

Ion irradiation-induced anisotropic plastic deformation

Teun van Dillen

Ion irradiation-induced anisotropic plastic deformation
Teun van Dillen

ISBN: 90-393-3670-9

Cover design by I. Cerjak

A digital version of this thesis can be downloaded from <http://www.amolf.nl>.
Printed copies can be obtained by request via e-mail to library@amolf.nl.

Ion irradiation-induced anisotropic plastic deformation

Anisotrope plastische deformatie
onder ionenbestraling

(met een samenvatting in het Nederlands)

Proefschrift

ter verkrijging van de graad van doctor aan de
Universiteit Utrecht op gezag van de Rector
Magnificus, Prof. Dr. W. H. Gispen, ingevolge het
besluit van het College voor Promoties in het
openbaar te verdedigen op maandag 26 april 2004 des
middags te 16.15 uur

door

Teun van Dillen

Geboren op 28 april 1976 te Culemborg

Promotor: Prof. Dr. A. Polman
Faculteit der Natuur- en Sterrenkunde, Universiteit Utrecht
FOM-Instituut voor Atoom- en Molecuulfysica, Amsterdam



The work described in this thesis was performed at the FOM-Institute for Atomic and Molecular Physics, Kruislaan 407, 1098 SJ Amsterdam, The Netherlands. It is part of the research program of the Foundation for Fundamental Research on Matter (FOM), and was made possible by financial support from the Dutch Organization for the Advancement of Research (NWO).

Contents

1	General introduction	9
1.1	Ion-solid interactions	10
1.2	Anisotropic plastic deformation under ion irradiation	11
1.3	This thesis	14
2	Anisotropic plastic deformation of colloidal silica particles under 4 MeV Xe ion irradiation	17
2.1	Introduction	18
2.2	Experimental	18
2.3	Results	19
2.4	Macroscopic phenomenological model for anisotropic deformation	22
2.5	Discussion	25
2.6	Conclusions	26
3.	Ion energy-dependent anisotropic deformation in several materials	29
3.1	Introduction	30
3.2	Experimental	30
3.3	Results and discussion	31
3.3.1	Silica colloids	31
3.3.2	Other materials	34
3.4	Conclusions	37
4.	Ion irradiation-induced anisotropic plastic deformation at 300 keV	41
4.1	Introduction	42
4.2	Experimental	42
4.3	Results and discussion	43
4.4	Conclusions	47

5. Anisotropic plastic deformation by viscous flow in ion tracks	49
5.1 Introduction	50
5.2 Formulation of the model	51
5.3 Initial state: instantaneous thermal loading	55
5.4 General time-dependent solution for viscous flow in single ion tracks	58
5.5 Viscous flow in single ion tracks: results	61
5.6 From mesoscopic model to macroscopic deformation	67
5.7 Discussion: comparison with experiment	70
5.8 Conclusions	71
Appendix 5.A	72
Appendix 5.B	73
6. Ion irradiation-induced anisotropic plastic deformation of silicon microstructures	77
6.1 Introduction	78
6.2 Experimental	78
6.3 Results and discussion	79
6.4 Conclusions	83
7. Stress map for ion irradiation: depth-resolved dynamic competition between radiation-induced viscoelastic phenomena in SiO₂	85
7.1 Introduction	86
7.2 Description of the model	87
7.3 Depth dependence of the in-plane stress	88
7.4 Stress map for ion irradiation	91
7.5 Conclusions	92

8. Activation energy spectra for annealing of ion irradiation-induced defects in silica glasses	95
8.1 Introduction	96
8.2 Experimental	96
8.3 Results and analysis	98
8.4 Discussion	101
8.5 Conclusions	104
9. Applications of shape-anisotropic colloidal particles and aggregates	107
9.1 Introduction	108
9.2 Anisotropic colloidal particles in solution	108
9.3 Modification of two-dimensional colloidal crystals, nanolithography	109
9.4 Photonic crystals of shape-anisotropic colloidal silica particles	111
9.5 Prolate silica colloids by multiple ion irradiation	113
9.6 Aligned gold nanorods in silica made by ion irradiation of core-shell colloidal particles	114
9.7 Conclusions	116
Summary	118
Samenvatting	121
Dankwoord - Acknowledgements	125
List of publications	127
Curriculum Vitae	128

1 *General introduction*

1.1 Ion-solid interactions

Ion implantation is a widely used technique in materials synthesis and modification. It is a key doping technique in semiconductor processing, and it is used to induce phase formation, amorphization, structural transformations or mixing in a wide range of materials. Its strength is the local control over species and concentration at a well-defined depth.

As an ion penetrates a solid, it loses energy due to two distinct interactions.^{1,2} First, it loses energy by *elastic*, nuclear collisions with the target atoms (nuclear stopping) described by the well-known Rutherford cross sections for the Coulomb interaction between the charged atomic nuclei. Second, it loses energy *inelastically* by exciting and ionizing electrons of target atoms (electronic stopping). Both stopping processes strongly depend on the kinetic energy of the ion. Figure 1.1 shows a graph of the nuclear and electronic energy loss and their sum as a function of ion energy for Xe irradiation of a SiO₂ target.

As can be clearly seen in Fig. 1.1, the stopping for Xe is dominated by the nuclear energy loss for ion energies smaller than ~ 2 MeV. In this energy range ions predominantly lose their energy due to Rutherford scattering. Due to collisions with the incident ions, target atoms are displaced from their original positions,³ leading to a subsequent nuclear collision cascade. The direct interaction between incoming ion and target atoms can lead to structural changes such as the generation of point defects, the amorphization of crystalline materials, or structural transformations in amorphous atomic networks. Nuclear stopping is also the origin of most sputtering processes and ion beam mixing of materials. All of these nuclear stopping effects are most efficient when the Rutherford scattering cross section is highest, i.e. for heavy incident ions at energies of typically 10-100 keV.

For higher ion energies (>2 MeV in Fig. 1.1) energy loss is dominated by electronic stopping. Due to the large mass difference between the ion and the electrons, the ion track remains roughly straight in this energy regime. Target atoms around the ion track are electronically excited. The energy in the electronic subsystem is subsequently transferred to the atomic subsystem by means of electron-phonon coupling, resulting in local lattice temperatures that can exceed several thousands of Kelvin.^{4,5} This then can lead to the formation of a cylindrically-shaped molten region around the ion track, of which the typical diameter is several nm. This process, commonly referred to as the '*inelastic*' thermal spike model, can therefore *indirectly* bring about structural changes in the target material. Indeed, electronic stopping can lead to structural modifications such as amorphization, defect generation and structural transformations provided the stopping is high. One prominent effect of electronic stopping processes is *anisotropic deformation*, a macroscopic materials shape

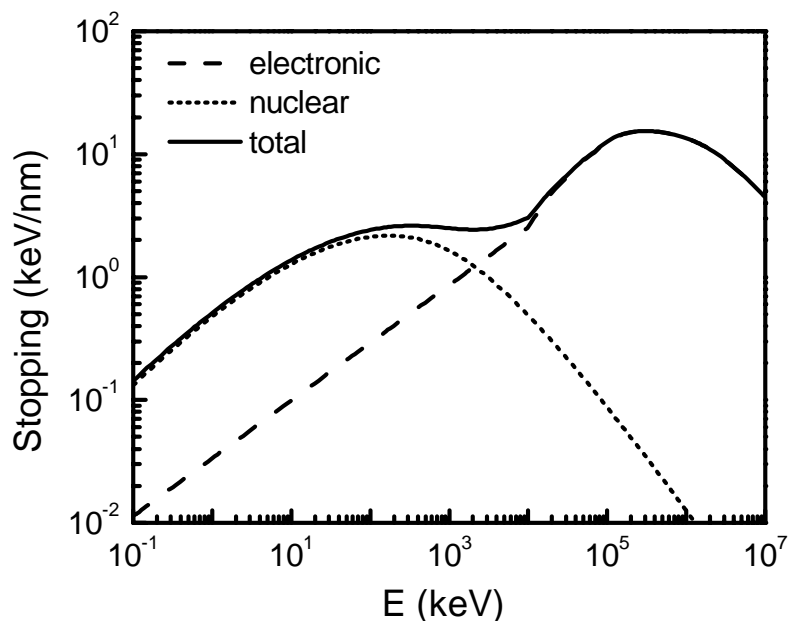


Figure 1.1 The nuclear (dotted line), electronic (dashed line) and total (solid line) stopping as a function of kinetic ion energy for Xe irradiation of a silica film (density: 2.2 g/cm³). The data are calculated using the SRIM 2000 Monte Carlo simulation code.¹

change that is the result of microscopic processes occurring in the thermal spike of individual ion impacts.

In the past 20 years much insight has been achieved in ion implantation doping distributions, in how ion irradiation amorphizes crystalline materials, how (point) defects are generated in crystalline hosts, and how structural changes in amorphous materials take place. Anisotropic deformation, however, has only been poorly studied and its origin is still a question of heated debates. Yet, this process provides for a unique way to control the shape of nano- and microshaped materials. This thesis focuses on ion irradiation-induced anisotropic plastic deformation, its origin and applications.

1.2 Anisotropic plastic deformation under ion irradiation

In the early eighties of the 20th century Cartz *et al.* discovered that small amorphous silicate particles undergo an irradiation creep process, extending the particles in the direction perpendicular to the ion beam.⁶ More detailed studies of this phenomenon followed in later studies by Klaumünzer and coworkers.⁷⁻¹¹ Thin films of metallic glasses or silica glasses of 5 to 15 μm thickness were irradiated with ions of several 100 MeV, i.e. in the electronic stopping regime, and it was found that the films expanded perpendicular to the ion beam direction

and contracted parallel to the ion beam direction, without significant volume change. Contrary to radiation-induced deformation that is observed in some cases in crystalline materials, where the anisotropy is the result of the preferred condensation of defects on certain crystallographic planes, the anisotropy of the growth phenomenon in amorphous materials was shown to originate from the directive ion beam.⁷

The deformation is quantified by the deformation strain rate A , which is defined as the differential length change per unit fluence:¹²

$$A = \frac{1}{L} \cdot \frac{dL}{d\phi}, \quad (1.1)$$

where ϕ is the ion fluence (the number of incident ions per unit area) and L a representative dimension perpendicular to the ion beam. It follows directly from Eq. (1.1) that for a constant strain rate, the dimension perpendicular to the ion beam should grow exponentially with ion fluence: $L=L_0\exp(A\phi)$. For high-energy ion irradiation (several 100 MeV) of thin foils of metallic and silica glasses at low substrate temperatures (<100 K), A was found to be in the range 10^{-17} - 10^{-14} cm²/ion.^{10,12} As an example, the latter value, in combination with a fluence of 10^{14} cm⁻² that is typical for many irradiation processes, translates into a deformation strain of $(L-L_0)/L_0=1.7$, indicating that anisotropic deformation can be quite a dramatic effect.

To study this anisotropic deformation process in better detail we initiated experiments on the ion irradiation of freestanding colloidal particles.¹³ Colloidal particles can be fabricated with a high degree of control of size and composition, and in combination with high-resolution electron microscopy, provide for a unique tool to investigate the anisotropic deformation process in detail. Figure 1.2 shows a scanning electron microscopy (SEM) image of a SiO₂ colloid with an original diameter of 1 μm that was irradiated with 4 MeV Xe ions to a fluence of 4×10^{14} cm⁻² at an angle of 45° at 90 K. The SEM image was taken (almost) perpendicular to the ion beam direction (side view, 10° tilt with respect to the substrate surface), using 10 keV electrons. The original ion beam is in the plane of the image, indicated by the white arrow. The original circumference of the colloidal particle before irradiation is indicated by the dashed circle. As can be clearly seen, the particle has expanded perpendicular to the ion beam and contracted parallel to the ion beam. The spherical particle has transformed into an oblate spheroid. The observed aspect ratio from this image (major over minor diameter) is ~2. This experiment demonstrates that the anisotropic plastic deformation can be accurately probed by imaging colloidal particles. Moreover, it also demonstrates that it can be observed at energies well below those studied in the early work by Klaumünzer and coworkers (several 100 MeV up to several GeV). Indeed, the 4 MeV ion energy used here is quite close to typical irradiation energies used in many practical experiments. In fact, as we will show in this thesis, anisotropic deformation is prominent at energies as low as 300

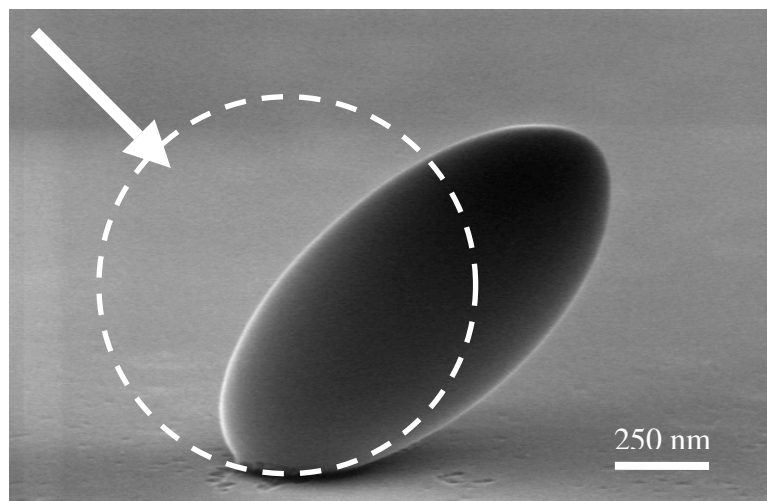


Figure 1.2 Side-view scanning electron microscopy image of a silica colloid after irradiation with 4 MeV Xe ions to a fluence of $4 \times 10^{14} \text{ cm}^{-2}$ at 90 K. The ion beam direction was tilted 45° away from the surface normal, indicated by the white arrow. The circumference of the originally spherical colloid is indicated by the dashed circle. The SEM image was taken (almost) perpendicular to the ion beam direction (10° tilt angle with respect to the substrate surface). The spherical colloid has transformed into an ellipsoidal oblate with its minor axis aligned with the ion beam.

keV, making study of this phenomenon relevant for a large range of ion-irradiation processes. Indeed, thousands of ion accelerators are operated today at voltages below 1 MV in integrated circuit manufacturing and in fundamental research on thin films. Anisotropic deformation is thus an important phenomenon that must be taken into account.

This thesis provides a detailed investigation of anisotropic plastic deformation of colloidal particles under ion irradiation. Taking advantage of their small size we were able to study the deformation process over a large ion energy range from 300 keV to 30 MeV. We determine the fluence and temperature dependence, and study it not only for SiO_2 , but also for other amorphous and crystalline materials. The data are then described and analyzed in terms of a viscoelastic model for anisotropic deformation resulting from shear stress relaxation in individual ion tracks. Based on the experimental results presented in this thesis and their good agreement with the viscoelastic model, we now have a quite complete understanding of the anisotropic deformation phenomenon.

1.3 This thesis

In Chapter 2 a detailed analysis is presented of the shape change of spherical colloidal silica particles under 4 MeV Xe ion irradiation. It is shown that the aspect ratio can be accurately tuned by varying the ion fluence, and size aspect ratios up to 5 are achieved. Particles irradiated at an angle of 45° with respect to the substrate surface normal perform a fluence-dependent angular “roll-off”, leading to an additional shape anisotropy. The deformation strain rate for 4 MeV Xe ion irradiation of colloidal silica particles is $A=6.0\times 10^{-16}$ cm²/ion.

In Chapter 3 we show that the irradiation does not significantly change the size polydispersity of a distribution of colloids. The transverse diameter perpendicular to the ion beam increases exponentially with ion fluence as predicted. By varying the ion energy in the range 4-16 MeV it is found that the deformation strain increases with electronic stopping. The deformation characteristics of colloidal particles of micro-crystalline ZnS, amorphous TiO₂, crystalline Al₂O₃ and micro-crystalline Ag are also studied and it is shown that anisotropic deformation only occurs in amorphous materials. The deformation of ZnS-SiO₂ and SiO₂-Au core-shell particles is also investigated.

In Chapter 4 we study anisotropic deformation in the energy range between 300 keV and 4.0 MeV. Anisotropic deformation at ion energies as low as 300 keV can still be observed. The transverse strain after irradiation increases with increasing electronic stopping without indication of a threshold, and gradually decreases with increasing irradiation substrate temperature.

In Chapter 5 a viscoelastic continuum model is derived for Newtonian viscous flow in ion-induced thermal spikes. A general expression for the macroscopic deformation strain rate A is derived and its dependence on the electronic stopping and irradiation temperature is discussed. By comparing this model with the experimental data in Chapters 2-4, we conclude that viscous flow in individual ion tracks is the origin of the macroscopic deformation process.

In Chapter 6 we present data on the deformation of crystalline and amorphous silicon micropillars during 30 MeV Cu irradiation. No deformation is found for crystalline Si, whereas amorphous silicon does deform anisotropically. The deformation rate of amorphous silicon is ~ 10 times smaller than that of silica glass, as will be discussed.

While Chapters 2-6 focus on the irradiation-induced deformation of freestanding, unconstrained colloidal particles and microstructures, in Chapters 7 and 8 we study the effect of a constraint on the deformation phenomenon. In this case irradiation-induced effects lead to the build-up of an in-plane stress, a quantity that can be accurately probed by measuring the sample curvature, using a sensitive, *in-situ*, scanning-laser wafer curvature technique.¹⁴ This makes it possible to study irradiation-induced processes that are accompanied by only very small dimensional changes (<1%, in case without constraint) that cannot be observed in the electron microscope.

In Chapter 7 we investigate the dynamic competition between anisotropic strain generation, densification by structural transformations, and Newtonian viscous flow under MeV ion irradiation. We demonstrate that the local stress in an irradiated SiO₂ film on a Si substrate exhibits variations with depth as large as several hundred MPa, ranging between tensile and compressive. The concept of a “stress map” is introduced, that predicts the depth-dependent, high-fluence saturation stress in silica films for a large range of irradiation conditions.

In Chapter 8 we present time-resolved stress measurements after MeV Xe ion irradiation of constrained films of thermal silica and alkali-borosilicate glass. From stress changes observed directly after the ion beam is switched off we conclude that, besides structural transformation, Newtonian viscous flow, and anisotropic strain generation, a fourth effect can occur during ion irradiation: the generation of volume-occupying defects. The accompanied stress changes are used to determine the defect activation energy spectrum in both thermally grown silica and alkali-borosilicate glass.

Finally, in Chapter 9 we report on several applications of shape-anisotropic colloidal particles made using ion irradiation. We discuss how anisotropic colloids can be brought in solution for studies on self-assembly. We show that ion irradiation can be used to deform two-dimensional colloidal crystals, providing a unique way to tailor masks for nanolithography. We then demonstrate the fabrication of three-dimensional photonic crystals of shape-anisotropic particles with modified optical properties. We report on the fabrication of prolate ellipsoidal particles by performing two subsequent, orthogonal ion irradiations and finally, we present the effect of ion irradiation of Au/SiO₂ core/shell particles, providing a novel way to fabricate Au nanorods with anisotropic optical properties.

References

- ¹ J. F. Ziegler, J. P. Biersack, and U. Littmark, *The Stopping and Range of Ions in Solids* (Pergamon, New York, 1985)
- ² R. Spohr, *Ion Tracks and Microtechnology, principles and applications* (Friedr. Vieweg & Sohn Verlagsgesellschaft mbH, Braunschweig, 1990)
- ³ The target atom is displaced in case the transferred energy is larger than the displacement energy of the atom: a typical value is 15 eV.
- ⁴ M. Toulemonde, Ch. Dufour, Z. Wang, and E. Paumier, *Nucl. Instrum. Methods Phys. Res. B* **112**, 26 (1996)
- ⁵ M. Toulemonde, J. M. Costantini, Ch. Dufour, A. Meftah, E. Paumier, and F. Studer, *Nucl. Instrum. Methods Phys. Res. B* **116**, 37 (1996)
- ⁶ L. Cartz, F. G. Karioris, and R. A. Fournelle, *Radiat. Eff.* **54**, 57 (1981)
- ⁷ S. Klaumünzer and G. Schumacher, *Phys. Rev. Lett.* **51**, 1987 (1983)

-
- ⁸ S. Klaumünzer, M.-d. Hou, and G. Schumacher, *Phys. Rev. Lett.* **57**, 850 (1986)
- ⁹ S. Klaumünzer, Changlin Li, and G. Schumacher, *Appl. Phys. Lett.* **51**, 97 (1987)
- ¹⁰ M.-d. Hou, S. Klaumünzer, and G. Schumacher, *Phys. Rev. B* **41**, 1144 (1990)
- ¹¹ A. Benyagoub, S. Löffler, M. Rammensee, S. Klaumünzer, and G. Saemann-Ischenko, *Nucl. Instrum. Methods Phys. Res. B* **65**, 228 (1992)
- ¹² S. Klaumünzer, *Radiat. Eff. Defects Solids* **110**, 79 (1989)
- ¹³ E. Snoeks, A. van Blaaderen, T. van Dillen, C. M. van Kats, M. L. Brongersma, and A. Polman, *Adv. Mater.* **12**, 1511 (2000)
- ¹⁴ C. A. Volkert, *J. Appl. Phys.* **70**, 3521 (1991)

2 *Anisotropic plastic deformation of colloidal silica particles under 4 MeV Xe ion irradiation*

Spherical colloidal silica particles with a diameter of 1029 nm ($\pm 3\%$) are irradiated with 4 MeV Xe ions to fluences ranging between 3×10^{13} and 1×10^{15} Xe/cm² at 90 K. During the irradiation the particles expand perpendicular to the ion beam and contract in the direction of the ion beam. The irradiation-induced anisotropic plastic deformation effect changes the shape of the particles from spherical into ellipsoidal, at constant volume. Particle size aspect ratios up to 5.2 ± 0.2 are achieved. The particles, irradiated at an angle of 45° with respect to the substrate normal, perform a fluence-dependent angular “roll-off”: after irradiation to a fluence of 1×10^{15} Xe/cm² the colloid’s minor axis has rotated by $(17 \pm 3)^\circ$ with respect to the ion beam direction. As a consequence of this angular roll-off, ellipsoids form with three principal axes of different length. We will show that the experimental data can be well described by a macroscopic phenomenological model for anisotropic deformation, yielding a deformation strain rate of 6.0×10^{-16} cm²/ion.

2.1 Introduction

Colloidal particles play an important role in studies of self-assembly and phase behaviour, and can find many applications in practical materials with interesting optical properties. The synthesis of colloidal model suspensions is well-explored and understood for a wide variety of inorganic materials.¹ However, most of the model systems with a narrow size distribution consist of spherical particles. It appears very difficult to synthesise *non-spherical* particles such as e.g., oblate and prolate ellipsoids with low polydispersity.² A system of optically transparent ellipsoidal colloids with adjustable aspect ratio would be ideal to investigate the effect of anisotropic particle shape on phase behaviour or optical properties.³⁻⁵ In this chapter we report a novel method to synthesise a new class of silica ellipsoidal colloids, that exploits a combination of colloidal chemistry^{6,7} and ion irradiation techniques.⁸ We find that monodisperse silica microspheres show a dramatic anisotropic plastic deformation^{9,10} under 4 MeV Xe ion irradiation that can be precisely tuned by varying the ion fluence. We will describe in detail the deformation characteristics under ion irradiation and show that our experimental results are in good agreement with a macroscopic phenomenological model for anisotropic plastic deformation.¹¹

2.2 Experimental

Silica microspheres with a diameter of 1030 nm were synthesized through hydrolysis and condensation reactions from tetraethoxysilane as described in Refs. 6 and 7. Drops of a dilute dispersion were placed on the clean surface of a Si (001) substrate, after which the ethanol solvent was left to evaporate.

The colloidal particles were irradiated with 4 MeV Xe⁴⁺ ions using a 1 MV Van de Graaff accelerator. The Xe⁴⁺ ions were generated in a Penning ion source. The ion beam was electrostatically scanned to homogeneously irradiate the entire sample to fluences in the range between 3×10^{13} and 1×10^{15} Xe/cm². The beam flux was in the range $(3-8) \times 10^{10}$ ions/cm²s. The Si substrate was tightly clamped against a copper sample stage and cooled to 90 K using liquid nitrogen. The base pressure during ion irradiation was 5×10^{-7} mbar.

The projected mean ion range was calculated using the SRIM 2000 computer code,¹² a Monte Carlo simulation program, using a silica structure with a density of 2.0 g/cm³, typical for colloidal silica.¹³ The projected mean ion range of 4 MeV Xe ions into silica is around 1.7 μm , well beyond the particle diameter.

Before and after irradiation the shape and size of the colloidal particles was measured by scanning electron microscopy (SEM), using an electron beam at 5 or 10 keV.

2.3 Results

Figure 2.1(a) shows a SEM image of unirradiated silica spheres on the Si surface, viewed under normal incidence to the substrate. The particle diameter is 1030 nm,¹⁴ with a relative size polydispersity of 3 %. Next, the particles were irradiated with 4 MeV Xe⁴⁺ ions with the sample surface held at an angle of +45° with respect to the direction of the ion beam, as indicated in the schematic inset in Fig. 2.1. Figures 2.1(b-d) show SEM images taken after irradiation to a fluence of 3×10^{14} ions/cm². The images were obtained using different sample-tilt angles in the microscope. The three (almost) orthogonal projections provide a full identification of the particle shape after irradiation: expansion is observed in the plane normal to the direction of the ion beam, and contraction in the direction of the beam. In Fig. 2.1(b) these ellipsoids are viewed along the direction of the ion beam, i.e., at a +45° tilt angle as indicated in the schematic inset. In this particular projection the ellipsoids appear circular. The dashed circle represents the circumference of unirradiated spheres. The transverse diameter (diameter perpendicular to the ion beam) of the particles has increased by 24 %. Figure 2.1(c) shows a SEM image taken perpendicular to the ion beam, at an angle of -45° (see schematic inset). The original ion beam direction is in the plane of the image as indicated by the white arrow in Fig 2.1(c). From this image it becomes clear that the colloidal particles have contracted parallel to the ion beam. Figure 2.1(d) shows a side view SEM image (15° tilt angle) taken perpendicular to the ion beam. From Figs. 2.1(c) and 2.1(d) it follows that the longitudinal diameter of the deformed particles (along the direction of the ion beam) has decreased with respect to the original diameter by about 35 %. From these measurements it follows that the volume of the colloids has remained constant during the irradiation.

Experiments as described above were performed for various Xe ion fluences ranging from 3×10^{13} to 1×10^{15} ions/cm². Figure 2.2 shows the ellipsoids' major diameter T (open circles) and minor diameter D (solid circles), obtained from side view SEM micrographs, as a function of ion fluence measured by averaging over a large number of colloids (see Chapter 3).¹⁵ Additional data at a fluence of 6×10^{14} Xe/cm² (triangles) correspond to the principle diameters of prolate ellipsoids that will be discussed in Chapter 9 (Section 9.5). As can be seen, the major diameter T increases monotonically with ion fluence, whereas the minor diameter D shows a monotonic decrease. We have performed deformation experiments using different ion fluxes in the range

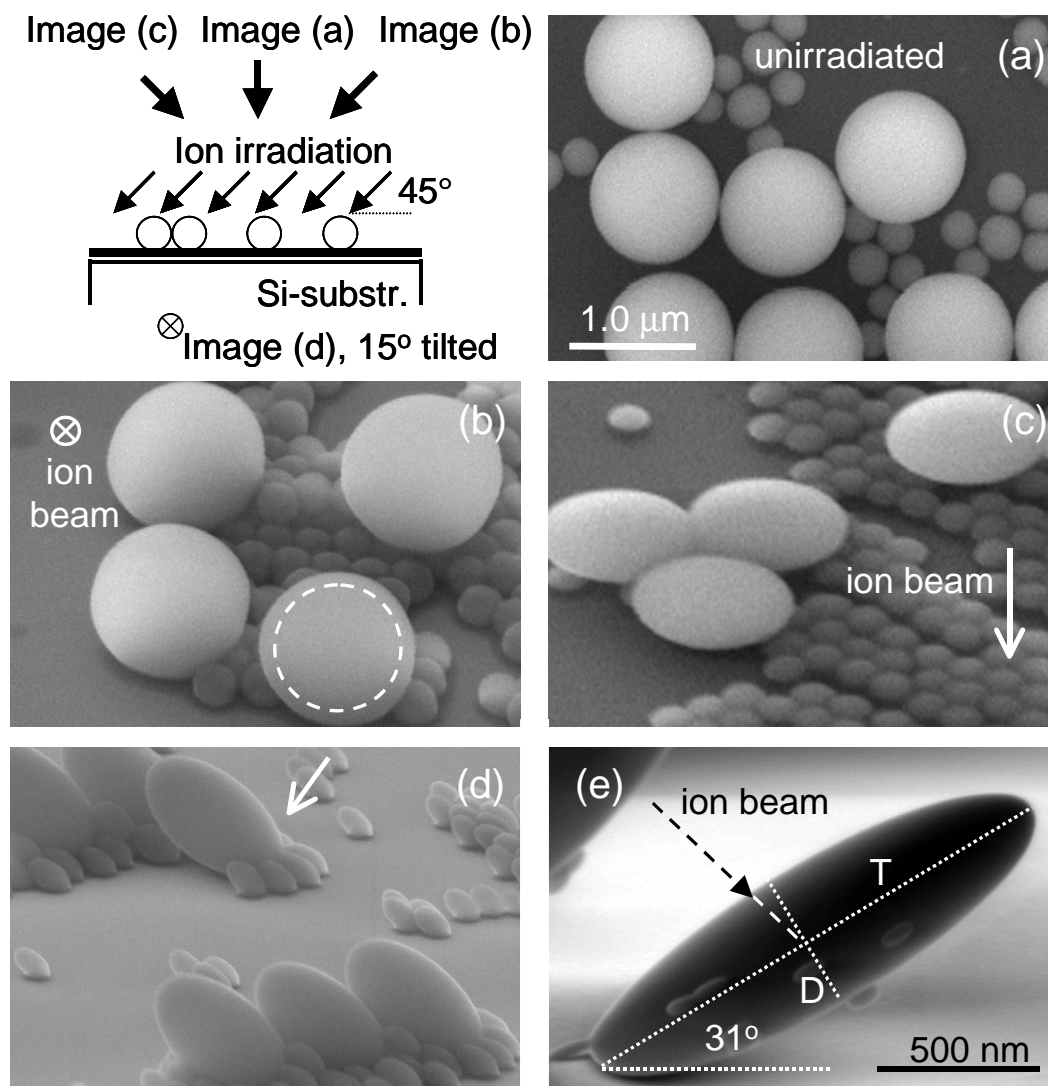


Figure 2.1 Scanning electron microscopy images of silica particles on a silicon substrate. **(a)** Top view (0° -tilt) of as-deposited silica spheres with two different diameters. **(b)-(d)** Silica ellipsoids that have formed after 4 MeV Xe irradiation to a fluence of $3 \times 10^{14} / \text{cm}^2$, at an angle of 45° relative to the surface normal, at 90 K. The ion beam direction and the different viewing angles are indicated in the schematic inset. The original ion beam direction is also indicated in the images. The dashed sphere in **(b)** indicates the spherical size of the colloids before irradiation. Images **(a)-(d)** are taken at the same magnification. **(e)** A silica colloid irradiated with $1 \times 10^{15} \text{ Xe/cm}^2$ at an angle of 45° . The ion beam direction, the angle between the colloid and substrate, and the colloid's 'major axis' T and 'minor' axis D are indicated in the image.

$(3.0\text{--}8.0)\times 10^{10}\text{ cm}^{-2}\text{s}^{-1}$, and found that the deformation for a given ion fluence is independent of the ion flux used.

Figure 2.1(e) shows a side-view SEM image (10° tilt angle with respect to the substrate's surface) of colloidal silica particles irradiated with 4 MeV Xe ions to a fluence of 1×10^{15} ions/cm². The diameters T and D are schematically indicated as well. As can be clearly seen at this large deformation ($T/D=4.8\pm 0.3$), the angle between the major particle axis (T) and the substrate is 31° , much smaller than the expected 45° , i.e. perpendicular to the original ion beam. The colloids have thus performed an angular “roll-off” with respect to the ion beam direction. For the particular colloid in Fig. 2.1(e) the roll-off angle is 14° , and on average an angle of $17\pm 3^\circ$ was found by analyzing a total of 10 colloids.

Figure 2.3 shows the projected minor diameter D_o of a single colloid measured at a view angle β with respect to substrate, as indicated in the schematic inset. We start by viewing perpendicular to the ion beam at $\beta=45^\circ$, where a value of $D_o=556\pm 5$ nm is observed. By decreasing the view angle, D_o first decreases and reaches a minimum value of $D_o=D=330$ nm at $\beta\sim 30^\circ$. By

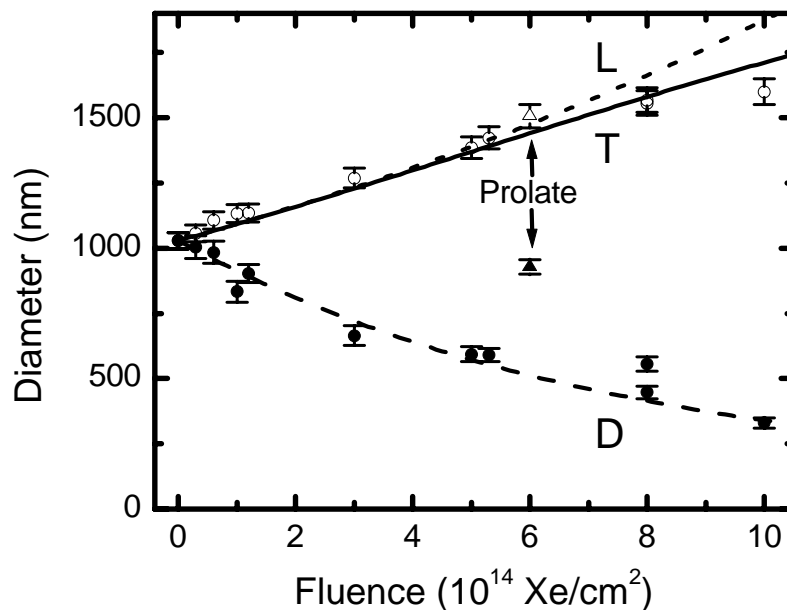


Figure 2.2 The major diameter T (open circles) and minor diameter D (solid circles) of silica ellipsoids as a function of 4 MeV Xe⁴⁺ irradiation fluence, determined from side view SEM images. The drawn curves for T (solid), L (dotted), and D (dashed) are calculated using Eq. (2.3) with a deformation strain rate of $A=6.0\times 10^{-16}$ cm²/ion. The triangles at a fluence of 6×10^{14} Xe/cm² represent T (open triangle) and D (solid triangle) of prolate ellipsoids, obtained after 2 orthogonal irradiations as discussed in Chapter 9.

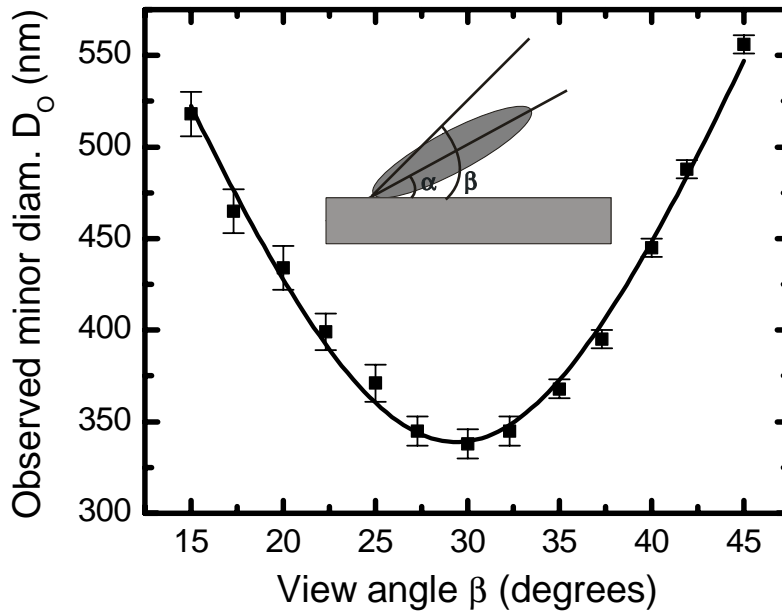


Figure 2.3 The observed (projected) minor diameter D_o as a function of the view angle β for a colloid irradiated with 4 MeV Xe to a fluence of 1×10^{15} Xe/cm² at an angle of 45° relative to the surface normal, at 90 K. The particles are viewed perpendicular to the transverse diameter L . The colloid angle α and view angle β are indicated in the schematic inset. The solid curve represents the best fit using Eq. (2.5) for ellipsoids: $\alpha = (29.4 \pm 0.2)^\circ$, $T = 1630 \pm 25$ nm and $D = 340 \pm 5$ nm.

decreasing β further, the diameter increases again to a value of $D_o = 518 \pm 12$ nm at $\beta = 15^\circ$. In this way the roll-off angle can be accurately determined. Moreover, from these data the ellipticity of the “rotated” colloid can be investigated (Sect. 2.5).

To obtain more insight in the fluence dependence of the roll-off effect, measurements of the particle angle α were performed as a function of ion fluence, and are presented in Fig. 2.4. An angle of 45° is observed for small fluences (1×10^{14} cm⁻²), while for higher fluences a gradual decrease is observed.

2.4 Macroscopic phenomenological model for anisotropic deformation

In Chapter 5 it will be shown that, on a microscopic scale, the anisotropic deformation phenomenon is the result of local viscous flow in single, high-temperature ion track cylinders brought about by the high electronic energy deposition of the ions. The observed macroscopic deformation is then the result of the integrated effect of a large number of microscopic single ion impacts. Note that at a fluence of 7×10^{14} ions/cm² each micron-sized particle has been impacted by some 10^7 Xe ions. Over such large numbers any statistical

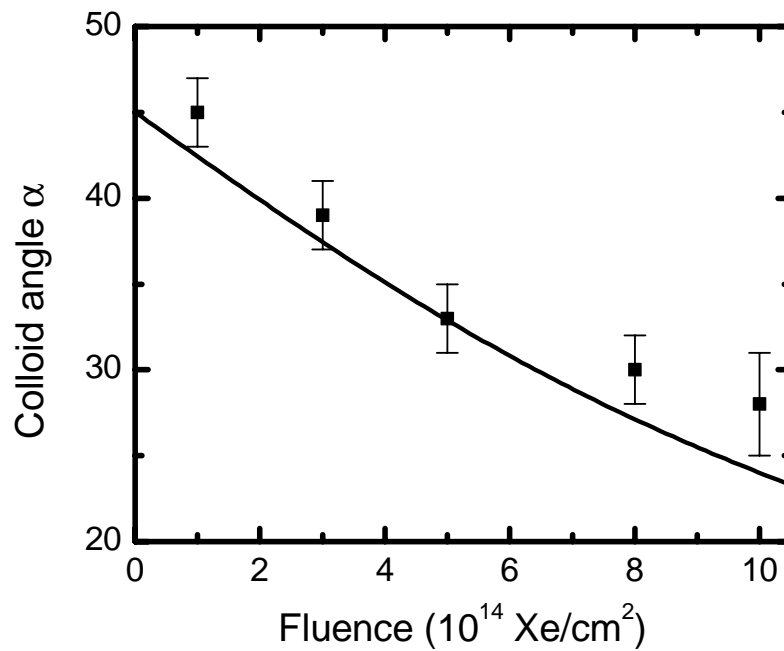


Figure 2.4 Angle α between substrate and major axis T of deformed silica colloids, as observed in side-view SEM images (10° and 15° tilt), as a function of ion fluence. Irradiations were performed using a 4 MeV Xe ion beam at 90 K. The drawn curve is calculated using Eq. (2.4) from the phenomenological model with $A=6.0 \times 10^{-16}$ cm 2 /ion.

variations are expected to average out, so that the deformed particles are expected to be very monodisperse in both size and shape. Measurements of the size polydispersity of silica particles before and after irradiation will be shown in Chapter 3 and confirm this.

Here we first focus on a description of the macroscopic deformation process quantified by a deformation strain rate A [Eq. (1.1)]. This process can be described phenomenologically by the rate-of-strain tensor $d\boldsymbol{\epsilon}/dt$, resulting from many ion impacts randomly over the sample surface. In the absence of a large-scale stress field, the rate-of-strain tensor for a sample irradiated at an ion flux F_{ion} and with its normal (z -axis) tilted by an angle θ with respect to the ion beam reads^{11,16}

$$\dot{\boldsymbol{\epsilon}} = AF_{ion} \begin{pmatrix} 1-3\sin^2\theta & 0 & 3\sin\theta\cos\theta \\ 0 & 1 & 0 \\ 3\sin\theta\cos\theta & 0 & 1-3\cos^2\theta \end{pmatrix}. \quad (2.1)$$

Here, the in-plane y -axis is the tilt axis. As an example, Eq. (2.1) shows that for $\theta=0^\circ$, with the ion beam in the direction of the z -axis, the in-plane sample dimensions perpendicular to the ion beam (x and y) grow at a rate AF_{ion} , whereas

the dimension in the direction of the ion beam (z) contracts at a rate $-2AF_{ion}$. The rate of volume change is equal to the trace of the rate-of-strain tensor and is zero. The deformation velocity vector \mathbf{v} of the material is directly linked to the rate-of-strain tensor by:

$$\dot{\boldsymbol{\varepsilon}} = \frac{1}{2}(\nabla\mathbf{v} + (\nabla\mathbf{v})^T), \quad (2.2)$$

where $\nabla\mathbf{v}$ is the velocity-gradient tensor and $(\nabla\mathbf{v})^T$ its transpose.

In a recent article by Klaumünzer, Eqs. (2.1) and (2.2) are used to describe the deformation of colloidal silica particles under MeV ion irradiation.¹⁷ In this model, the contact area of the colloid with the substrate is approximated by a fixed stress-free contact point. This approximation holds in case the stresses are confined to small region around the contact area. Using the condition that the substrate is a tangential plane of the colloid at the contact point, Eqs. (2.1) and (2.2) can then be integrated twice, resulting in the motion $\mathbf{r}=(x,y,z)$ of the colloid. Klaumünzer has shown that under ion irradiation at an angle of $\theta=45^\circ$ to a fluence ϕ , a spherical particle of radius R transforms into an ellipsoid having principal diameters D , T and L given by:

$$\begin{aligned} D &= \frac{2R \cdot \exp[-A\phi/2]}{\sqrt{1 + \frac{9}{2}(A\phi)^2 + 3A\phi\sqrt{1 + \frac{9}{4}(A\phi)^2}}} \\ T &= \frac{2R \cdot \exp[-A\phi/2]}{\sqrt{1 + \frac{9}{2}(A\phi)^2 - 3A\phi\sqrt{1 + \frac{9}{4}(A\phi)^2}}}, \\ L &= 2R \cdot \exp[A\phi] \end{aligned} \quad (2.3)$$

where the deformation strain rate A is assumed to be constant. Using Eq. (2.3) it is easy to show that the volume of the colloid remains constant, i.e. $\pi DLT/6=(4/3)\pi R^3$. The axes D and T are indicated in the SEM image of Fig. 2.1(e). The diameter L is always oriented perpendicular to the ion beam and is (almost) perpendicular to the image in Fig. 2.1(e). For a constant deformation strain rate A , the exponential behaviour of L can also be found directly from Eq. (1.1).

Finally, as shown by Klaumünzer, the angle α between the colloid and the substrate is given by:¹⁷

$$\alpha = \arctan\left[\left(\frac{3}{2}A\phi + \sqrt{1 + \frac{9}{4}(A\phi)^2}\right)^{-1}\right]. \quad (2.4)$$

Equations (2.3) and (2.4) can now be used to fit our data presented in Figs. 2.2 and 2.4.

2.5 Discussion

The drawn curves in Fig. 2.2 show the major diameters T (solid) and L (dotted) and the minor diameter D (dashed) as a function of fluence, calculated using Eq. (2.3) with $2R=1029$ nm. The model shows good agreement with the experimental data for diameters T and D using a deformation strain rate of $A=6.0\times 10^{-16}$. This agreement also shows that the volume of the colloids is conserved up to fluences as high as 1×10^{15} cm⁻².

For small fluences ($\phi < 6\times 10^{14}$ cm⁻²), the calculated growth of the major diameters L and T is similar and roughly linear with ion fluence. In this fluence range the ellipsoid is an oblate spheroid having two major diameters L and a minor diameter D . Indeed, in the small fluence range no difference is found experimentally between L and T . The calculation shows that for larger ion fluences ($\phi > 6\times 10^{14}$ cm⁻²) the exponential growth of L deviates from the growth of T . In this fluence range the oblates gradually transform into ellipsoids having three principal axes of different length. For the highest fluence irradiation performed in this work ($\phi = 1\times 10^{15}$ cm⁻²), L is found to be 1770 nm (not shown in Fig. 2.2), indeed larger than the measured value of T (1600 nm). The fact that T does not grow exponentially is the result of the colloid's angular roll-off, since this axis is no longer perpendicular to the ion beam. In fact, from the model it can be derived that for $A\phi \gtrsim 2$, T must *contract*. This would occur at $\phi \gtrsim 3.3\times 10^{15}$ cm⁻² for the strain rate in our work.¹⁷

The solid line in Fig. 2.4 shows the calculated fluence dependence of the colloid angle α according to Eq. (2.4). Starting at $\alpha=45^\circ$ the angle gradually decreases with ion fluence as is observed in our experiments (solid squares). Again, this phenomenological model shows good agreement with the experimental data for $A=6.0\times 10^{-16}$ cm²/ion. This implies that the “roll-off” effect is a direct consequence of the anisotropic deformation effect.

In the next chapters of this thesis, the measured “*transverse diameter*” is defined as the major diameter L , i.e. the direction that always remains perpendicular to the ion beam at each moment during irradiation, irrespective of the angular roll-off. It can easily be measured by taking SEM images perpendicular to the ion beam, as in Fig. 2.1(c), or along the substrate normal. Determination of the minor diameter D from SEM images taken perpendicular to the ion beam is more complicated. Due to the colloid's rotation the observed projected minor diameter D_o is larger than D . For an ellipsoidal particle with major diameters L and T , minor diameter D oriented at an angle α with the substrate, it can be shown that the observed (projected) minor diameter is given by:

$$D_o = D \sqrt{\cos^2(\alpha - \beta) + \left(\frac{T}{D}\right)^2 \sin^2(\alpha - \beta)}, \quad (2.5)$$

when the colloid is viewed at an angle β with respect to the sample surface (see inset Fig. 2.3) and perpendicular to axis L .

The solid line in Fig. 2.3 is a fit of Eq. (2.5) to the measured projections D_o (solid squares), with α , T and D fitting parameters.¹⁸ For the specific colloid under investigation this results in $\alpha=(29.4\pm 0.2)^\circ$, $T=1630\pm 25$ nm and $D=340\pm 5$ nm. Note that these values for α and T agree well with the values determined from side view projections (Figs. 2.2 and 2.4). The size aspect ratio of this colloid, defined as L/D , is therefore 5.2 ± 0.2 ($L=1770\pm 50$ nm).

Figure 2.3 thus shows that, for large particle size aspect ratios, D_o varies quite drastically for small variations in the view angle β . If the average minor diameter of colloids is determined from one projection only, e.g. perpendicular to the ion beam, a correction to the observed value using Eq. (2.5) is necessary. A side view image such as Fig. 2.1(e) is therefore needed to determine the average values of α and T . In the next chapters of this thesis we have performed the correction using Eq. (2.5). For aspect ratios smaller than 2 and corresponding roll-over angles smaller than 10° , the correction modifies the result only slightly, generally within the error of the experiment.

2.6 Conclusions

The combination of chemical synthesis and ion irradiation techniques makes it possible to fabricate a new class of colloidal ellipsoids with continuously variable shape.

Spherical colloidal silica particles with a diameter of 1029 nm were irradiated with 4 MeV Xe ions at an angle of 45° to fluences in the range between 3×10^{13} and 1×10^{15} Xe/cm². It is shown that the irradiation induces an anisotropic plastic deformation effect at constant volume: the particles expand in the plane perpendicular to the ion beam and contract in the direction of the ion beam, changing the colloid's shape from spherical to oblate ellipsoidal. A size aspect ratio as large as 5.2 is observed for the highest ion fluence used. The deformation increases with ion fluence and is independent of the ion flux used.

During irradiation the particles perform a gradual angular "roll-off" with respect to its original direction perpendicular to the ion beam. The roll-off angle gradually increases with ion fluence to a value of $(17\pm 3)^\circ$ at 1×10^{15} cm⁻². Due to this effect the oblates transform into ellipsoids with three different principle diameters. The fluence dependence of the deformation and the angular roll-off effect can be well described by a phenomenological model, from which follows that the deformation strain rate under 4 MeV Xe ion irradiation is 6.0×10^{-16} cm²/ion.

References

- ¹ E. Matijevic, *Langmuir* **10**, 8 (1994)
- ² C. C. Ho, A. Keller, J. A. Odell, and R. H. Ottewill, *Colloid. Polym. Sci.* **271**, 469 (1993)
- ³ L. Onsager, *Ann. (N.Y.) Acad. Sci.* **51**, 627 (1949)
- ⁴ D. Frenkel, and B. M. Mulder, *Mol. Phys.* **55**, 1171 (1985); J. A. Veerman and D. Frenkel, *Phys. Rev. A* **45**, 5632 (1992)
- ⁵ J. U. Noeckel and A. D. Stone, *Nature* **385**, 45 (1997)
- ⁶ W. Stöber, A. Fink, and E. Bohn, *J. Colloid Interface Sci.* **26**, 62 (1968)
- ⁷ A. van Blaaderen, J. van Geest, and A. Vrij, *J. Colloid Interface Sci.* **154**, 481 (1992)
- ⁸ E. Snoeks, A. Polman, and C. A. Volkert, *Appl. Phys. Lett.* **65**, 2487 (1994); E. Snoeks, T. Weber, A. Cacciato, and A. Polman, *J. Appl. Phys.* **78**, 4723 (1995)
- ⁹ S. Klaumünzer, *Radiat. Eff.* **110**, 79 (1989)
- ¹⁰ A. Benyagoub, S. Löffler, M. Rammensee, S. Klaumünzer, and G. Saemann-Ischenko, *Nucl. Instrum. Methods Phys. Res. B* **65**, 228 (1992)
- ¹¹ S. Klaumünzer and A. Benyagoub, *Phys. Rev. B* **43**, 7502 (1991)
- ¹² J. F. Ziegler, J. P. Biersack, and U. Littmark, *The Stopping and Range of Ions in Solids* (Pergamon Press, New York, 1985)
- ¹³ A. van Blaaderen and A. P. M. Kentgens, *J. Non-Cryst. Solids* **149**, 161 (1992)
- ¹⁴ Spherical silica colloids of 290 nm in diameter were also dispersed on the Si substrate as can be seen in Fig. 2.1(a). The deformation of these particles under ion irradiation will be described in detail in Chapter 4.
- ¹⁵ The values of D in Fig. 2.2 have been corrected for the side-view tilt angle.
- ¹⁶ A. Gutzmann, S. Klaumünzer, and P. Meier, *Phys. Rev. Lett.* **74**, 2256 (1995)
- ¹⁷ S. Klaumünzer, *Nucl. Instrum. Methods Phys. Res. B* **215**, 345 (2004)
- ¹⁸ One could directly reduce the number of fit parameters by taking fixed values for α and T , determined from independent measurements, e.g. from side-view images [Fig. 2.1(e)].

3 *Ion energy-dependent anisotropic deformation in several materials*

Spherical silica colloids with a diameter of 1.0 μm , made by wet chemical synthesis, were irradiated with 2-16 MeV Au ions at fluences in the range $(2-11)\times 10^{14} \text{ cm}^{-2}$. The irradiation induces an anisotropic plastic deformation turning the spherical colloids into ellipsoidal oblates. After 16 MeV Au irradiation to a fluence of $11\times 10^{14} \text{ cm}^{-2}$, a size aspect ratio of 5.0 was achieved. The size polydispersity ($\sim 3\%$) remains unaffected by the irradiation. The transverse diameter increases exponentially with ion fluence. From the energy dependence it is concluded that the deformation is dominated by the electronic energy loss. Nonellipsoidal colloids are observed in the case that the projected ion range is smaller than the colloid diameter. The deformation effect is also observed for amorphized micro-crystalline ZnS and amorphous TiO_2 colloids, as well as ZnS/ SiO_2 and SiO_2 /Au core/shell particles. No deformation is observed for crystalline Al_2O_3 and Ag particles. The data provide strong support for the thermal spike model of anisotropic deformation.

3.1 Introduction

MeV-ion irradiation of amorphous materials such as metallic or silica glasses is known to cause anisotropic plastic deformation.¹⁻⁵ The result is an increase of the sample dimension perpendicular to the ion beam and a decrease in the direction parallel to the ion beam. This deformation process can be described mesoscopically by a viscoelastic model, in which it is assumed that, due to the high electronic stopping power, a cylindrically-shaped region around the ion track is subject to transient heating (thermal spike).⁶⁻⁸ During the thermal spike, shear stresses in the heated region relax, resulting in an associated shear strain that would freeze in upon cooling of the thermal spike (see Chapter 5).

Experimentally, the anisotropic deformation has been studied by observing macroscopic dimensional changes of (metallic) glass foils^{1,2} or by studying the wafer curvature induced by irradiated thin films constrained on a substrate.^{4,5,9} In Chapter 2, we have shown that the deformation process also occurs in free-standing colloidal particles.¹⁰ Spherical colloidal SiO₂ particles can be changed into ellipsoidal-shaped particles due to a biaxial expansion perpendicular to the ion beam and a concomitant contraction along the ion beam. Colloidal particles with variable shape can find many applications in studies of self-assembly and phase behavior¹¹ and, except ion irradiation, no other methods exist that can produce nonspherical colloids that are monodisperse in size and shape. It is therefore important to study the dependence of the deformation effect on irradiation parameters such as ion energy and fluence.

In this chapter, we study the dependence of the deformation of spherical silica particles on Au ion fluence in the energy range 2-16 MeV. We find that the anisotropic deformation rate shows a gradual increase with electronic stopping power in the colloid. We also study the special case in which the ion beam only partly penetrates the colloids, and find that nonellipsoidal particles are formed. The data provide strong evidence for the thermal spike model for anisotropic deformation. In addition, we study the deformation of micro-crystalline ZnS and amorphous TiO₂ colloids, ZnS/SiO₂ and SiO₂/Au core/shell particles, as well as single-crystalline Al₂O₃ and micro-crystalline Ag particles.

3.2 Experimental

Colloidal silica spheres were made in a solution containing tetra-ethoxysilane, ammonia and ethanol.¹² A drop of the colloidal dispersion was dried on a Si(100) substrate which had previously been cleaned for 10 minutes in a 1.0 M KOH-ethanol solution. Next, the particles were irradiated with Au ions using the 3 MV tandetron accelerator at the ion beam facility in Rossendorf.¹³ The ion

beam was electrostatically scanned across a $5.1 \times 5.1 \text{ cm}^2$ area. The ion energy was varied between 2 and 16 MeV and fluences ranged from $(2 - 11) \times 10^{14} \text{ cm}^{-2}$. The ion beam energy flux was kept constant at a value of 0.16 W/cm^2 during all irradiations. The substrate holder was cooled with liquid nitrogen, and all irradiations were performed at an angle of 45° with respect to the Si surface. Vacuum grease at the backside of the sample was used to improve the heat contact between the sample and the cooled substrate holder. Note that the actual colloid temperature during irradiation might be higher than that of the holder. Ion ranges and electronic energy losses were calculated using TRIM98,¹⁴ a Monte Carlo simulation program, using a silica structure with a density of 2.0 g/cm^3 .¹⁵

ZnS and ZnS/SiO₂ core/shell particles as well as micro-crystalline Ag particles were synthesized using methods described in Refs. 16 and 17. TiO₂ colloids were made as described in Ref. 18, and single-crystalline α -Al₂O₃ particles were obtained from Sumitomo Chemical Co. Ltd. (Japan). The synthesis of Au/SiO₂ core/shell particles is described in Ref. 19. All these particles were irradiated with a 4 MeV Xe ion beam at 77 K. The ion beam was electrostatically scanned across a $2.7 \times 2.7 \text{ cm}^2$ area at a flux of $\sim 0.02 \text{ W/cm}^2$.

Scanning electron microscopy (SEM) was performed at an energy of 10 keV at different angles to image the particle shape before and after irradiation. Image processing and analysis software were used to characterize the particles before and after irradiation.

3.3 Results and discussion

3.3.1 Silica colloids

Figure 3.1(a) shows a SEM image of unirradiated silica particles on a silicon substrate viewed under normal incidence (see schematic in Fig. 3.1). The size distribution of 65 analyzed colloids is displayed in Fig. 3.2 (black histogram). The average colloid diameter is $1004 \pm 20 \text{ nm}$ ²⁰ with a standard deviation characterizing the size polydispersity $\sigma = 31 \pm 3 \text{ nm}$. This is typical for the colloid fabrication method used.¹²

Next, the colloids were irradiated with a 14 MeV Au⁴⁺ ion beam to a fluence of $4 \times 10^{14} \text{ cm}^{-2}$, at an angle of 45° (see schematic in Fig. 3.1). The projected ion range was calculated to be about $3.5 \mu\text{m}$,¹⁴ well beyond the particle diameter. Figure 3.1(b) shows a SEM micrograph after irradiation taken in the direction perpendicular to the ion beam. Clearly, the originally spherical particle has turned into an ellipsoid with a dimensional expansion perpendicular to the ion beam and a contraction parallel to the ion beam.²¹

Figure 3.2 also shows the size distribution of the transverse diameter L (perpendicular to the ion beam, as defined in Chapter 2) of 33 particles after

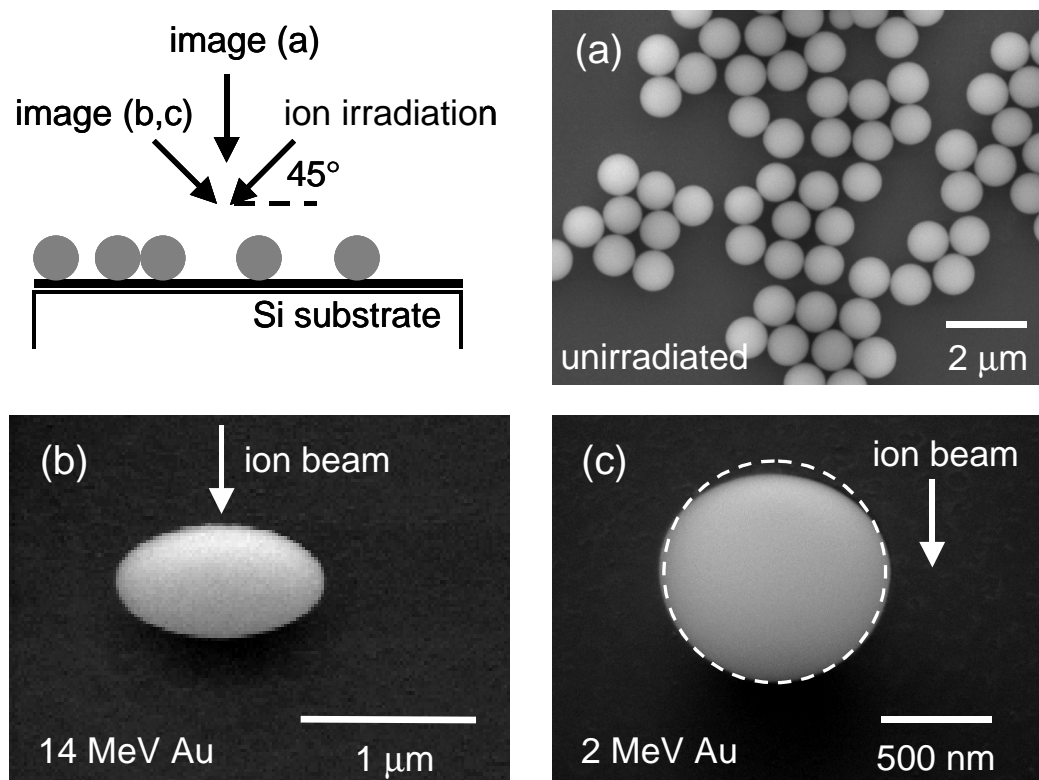


Figure 3.1 Scanning electron microscopy (SEM) images of unirradiated and Au ion irradiated silica colloids on a silicon substrate. The ion beam direction and the different SEM viewing angles are depicted in the schematic. The arrows in the SEM images indicate the direction of the ion beam. **(a)** Unirradiated silica colloids in top view. **(b)** Deformed silica colloid after irradiation with 14 MeV Au⁴⁺ ions to a fluence of $4 \times 10^{14} \text{ cm}^{-2}$ at 45° at 77 K. **(c)** Deformed silica colloid after an irradiation with 2 MeV Au²⁺ ions ($4 \times 10^{14} \text{ cm}^{-2}$). A circular shape is shown for reference.

irradiation (gray histogram). This diameter has increased to a mean value of $1181 \pm 20 \text{ nm}$, with $\sigma = 27 \pm 3 \text{ nm}$. This indicates that the ion irradiation process does not significantly increase the particle size polydispersity. Note that at a fluence of $4 \times 10^{14} \text{ cm}^{-2}$ each colloid has been impacted by some 10^6 - 10^7 ions. Indeed, at this large number of ions any statistical variations are expected to be averaged out. Assuming the colloidal volume remains constant after irradiation,¹⁰ the size aspect ratio L/D of the deformed colloids in Fig. 3.1(b) is calculated to be 1.63.

Figure 3.1(c) shows a SEM micrograph of a colloid after irradiation with 2 MeV Au²⁺ ions to a fluence of $4 \times 10^{14} \text{ cm}^{-2}$, viewed in the direction perpendicular to the ion beam. The projected range of 2 MeV Au ions in SiO₂ is about $0.55 \mu\text{m}$, roughly equal to half the colloid diameter. This implies that the lower half of the colloid is not fully irradiated, except at the lateral side edges.

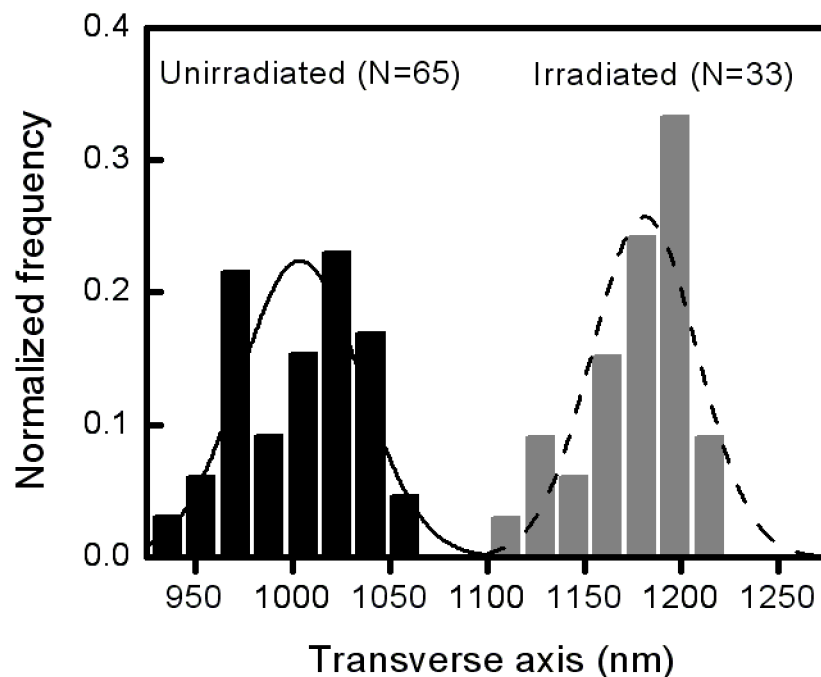


Figure 3.2 Histogram of the transverse diameter size distribution of unirradiated silica colloids (black bars) and silica colloids irradiated with 14 MeV Au⁴⁺ ions to a fluence of $4 \times 10^{14} \text{ cm}^{-2}$ (gray bars). Gaussian distributions with standard deviations of $\sigma = 31 \text{ nm}$ (unirradiated) and $\sigma = 27 \text{ nm}$ (irradiated) are indicated by the solid and dashed line, respectively.

Figure 3.1(c) clearly shows a nonellipsoidal shape of the colloid: the upper part of the colloid is deformed whereas the lower part remains undeformed (see white dashed line). This clearly indicates that the deformation only takes place in the irradiated region of the colloid. From this, we can conclude that the plastic deformation does not result from a uniaxial pressure generated by the ion beam, but results from single-ion impacts only. This is in agreement with the thermal spike model that will be discussed in Chapter 5.

Figure 3.3 shows the transverse particle dimension after irradiation with 8 MeV Au³⁺ ions at 45° for fluences ranging from $(2-11) \times 10^{14} \text{ cm}^{-2}$. The data were obtained from SEM micrographs taken at normal incidence. The transverse diameter increases with ion fluence from $1004 \pm 20 \text{ nm}$ for unirradiated particles to $L = 1494 \pm 20 \text{ nm}$ after irradiation with $11 \times 10^{14} \text{ cm}^{-2}$ Xe ions. If the strain rate per ion, defined by Eq. (1.1), would be constant with fluence, an exponential increase of the transverse diameter with ion fluence is expected. To describe the measured behavior, we fitted the data with an exponential function using a strain rate of $A = (3.6 \pm 0.1) \times 10^{-16} \text{ cm}^2/\text{ion}$.

Figure 3.3 also shows the fluence dependence for 16 MeV Au⁵⁺ irradiation. The colloid size aspect ratio after 16 MeV Au irradiation to a fluence of $11 \times 10^{14} \text{ cm}^{-2}$ is 5.0. Again, an exponential behavior is observed in the same

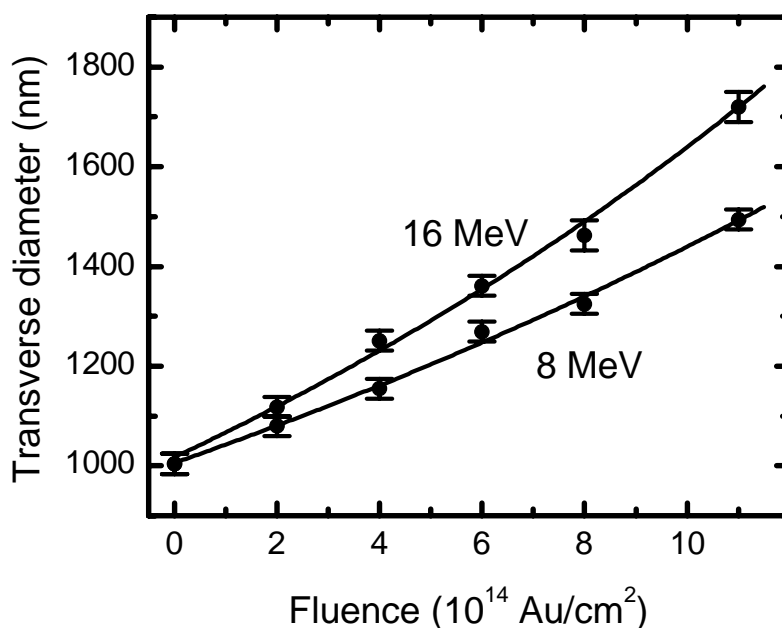


Figure 3.3 Transverse diameter of the silica spheroids as function of ion fluence. Results are shown for irradiations with 8 MeV Au $^{3+}$ and 16 MeV Au $^{5+}$. Exponential fits to the data are included.

fluence range, characterized by a strain rate of $A=(4.8\pm 0.2)\times 10^{-16}$ cm 2 /ion. Clearly, comparing the two data sets in Fig. 3.3, at a fixed fluence the deformation increases with ion energy.

To further investigate the energy dependence of the deformation, silica spheres were irradiated with Au ions at energies ranging from 4-16 MeV to a fixed fluence of 4×10^{14} cm $^{-2}$. Figure 3.4 shows the measured transverse strain (relative to the original diameter) after irradiation, plotted as a function of the average electronic stopping power in the colloid. The latter is calculated using a 3-dimensional averaging method taking into account the changing shape of the colloid during irradiation.

Figure 3.4 shows that the transverse strain gradually increases with average electronic stopping. With increasing ion energy from 4 to 16 MeV the average *nuclear* stopping decreases monotonically from 1.9 to 0.8 keV/nm, whereas the average *electronic* stopping increases from 1.7 to 3.8 keV/nm. Since the deformation strain increases in this ion energy range, it must therefore be mainly dependent on the electronic energy loss of the ions. This will be further discussed in Chapter 4.

3.3.2 Other materials

Figure 3.5 shows SEM images of colloidal particles of several other materials, all irradiated with 4 MeV Xe ions at 77 K. A side view image of micro-

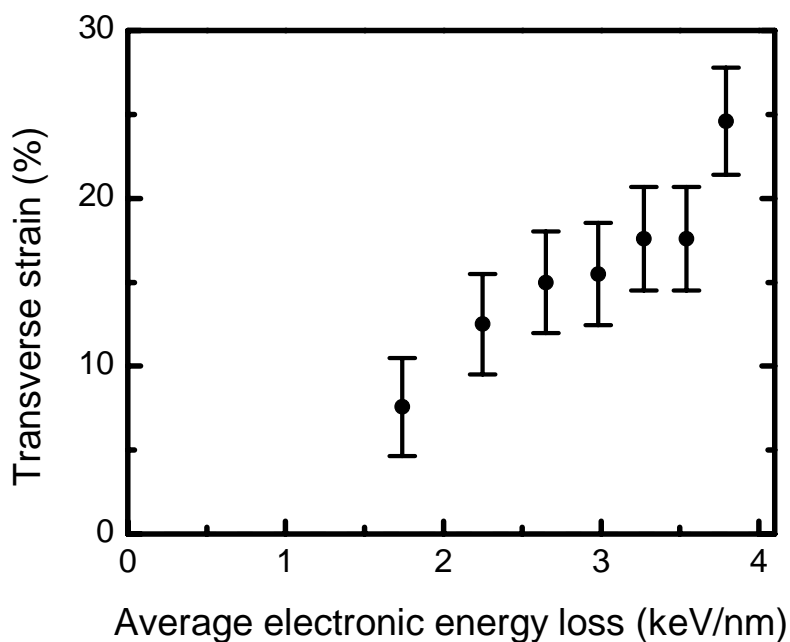


Figure 3.4 Transverse strain of silica spheroids as a function of average electronic energy loss at a fixed fluence of $4 \times 10^{14} \text{ cm}^{-2}$. Data were taken from experiments using Au ions at ion energies in the range (4-16) MeV.

crystalline ZnS particles irradiated at a fluence of $5 \times 10^{14} \text{ cm}^{-2}$ is shown in Fig. 3.5(a). The size aspect ratio of these particles is 2.2. This is similar to what is observed for silica particles irradiated under the same conditions (Chapter 2).¹⁰ Figure 3.5(b) shows deformed core/shell particles composed of a 692 nm-diameter ZnS core covered by a 5 nm thick SiO_2 shell after irradiation with $4 \times 10^{14} \text{ Xe cm}^{-2}$. The observed size aspect ratio is about twice as large as what would be observed for the individual materials at this same fluence. At present this difference remains to be explained.

Next, we studied the deformation of amorphous TiO_2 colloids. These particles cannot be made with the small size polydispersity as common for the SiO_2 and ZnS colloids, as can be seen in Fig. 3.5(c). However a deformation after irradiation ($3 \times 10^{14} \text{ Xe cm}^{-2}$) can clearly be seen in Fig. 3.5(d). This demonstrates the versatility of the ion irradiation technique to deform a variety of materials.

Figure 3.5(e) shows single-crystalline Al_2O_3 colloids after irradiation with $4 \times 10^{14} \text{ Xe/cm}^2$. Although less easy to identify in the SEM image because of the particle clustering, we find no evidence for anisotropic deformation of this material. Similarly, micro-crystalline Ag colloids [$4 \times 10^{14} \text{ Xe/cm}^2$, Fig 3.5(f)] show no deformation. In addition, no deformation was found after irradiation of Ag colloids with 30 MeV Se ions to a fluence of $2 \times 10^{14} \text{ Se/cm}^2$ (data not shown).

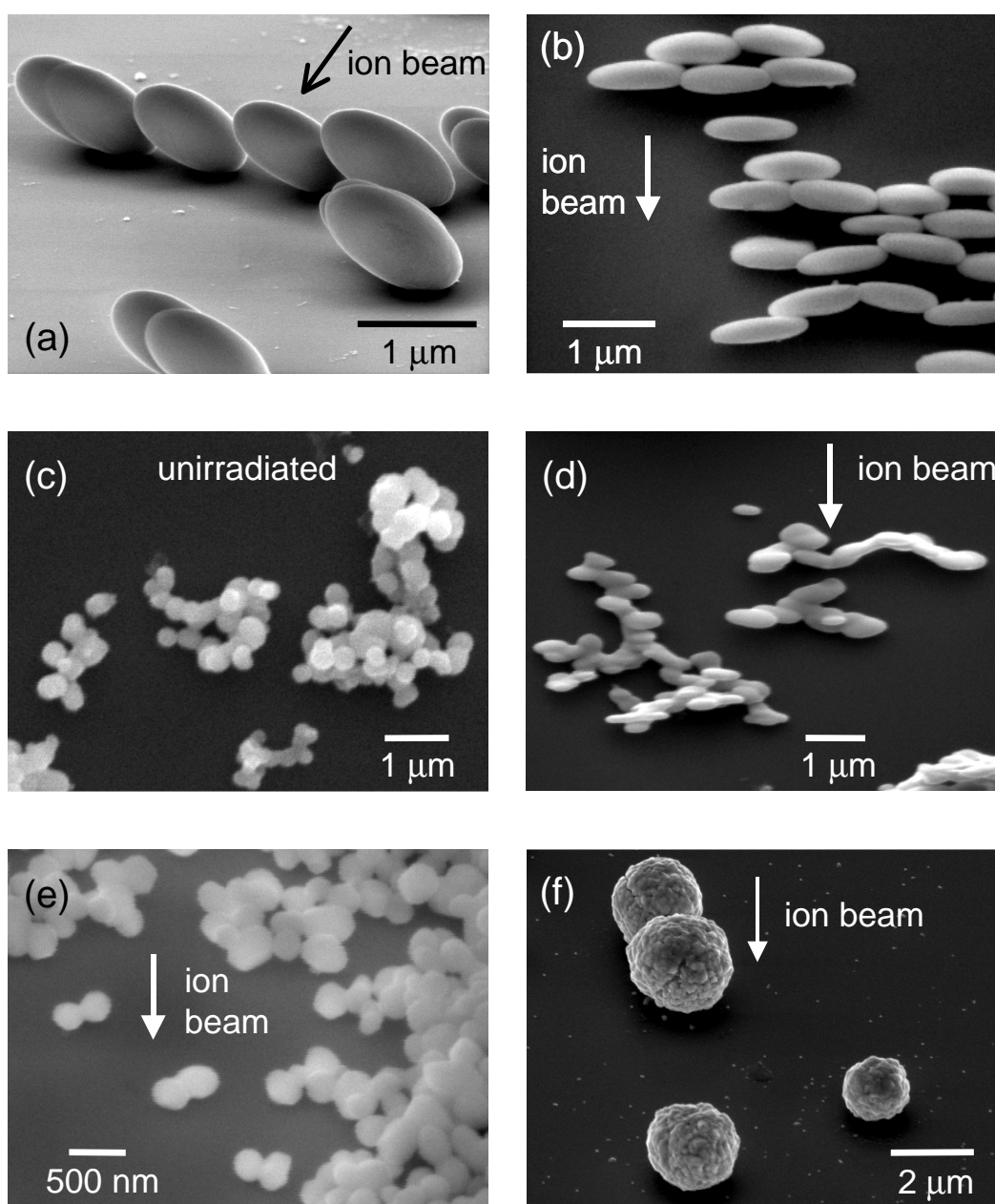


Figure 3.5 SEM images of ion irradiated colloids of various materials. The irradiations were all performed using a 4 MeV Xe ion beam at 77 K. The direction of the ion beam is indicated by the arrows. All images were taken as in projection (b) in the schematic of Fig. 3.1 (except (a), that was taken from the side at a 15° tilt). (a) irradiated micro-crystalline ZnS ($5 \times 10^{14} \text{ cm}^{-2}$), (b) irradiated ZnS/SiO₂ core/shell particles ($4 \times 10^{14} \text{ cm}^{-2}$), (c) unirradiated amorphous TiO₂, (d) irradiated amorphous TiO₂ ($3 \times 10^{14} \text{ cm}^{-2}$), (e) irradiated single-crystalline Al₂O₃ ($4 \times 10^{14} \text{ cm}^{-2}$), (f) irradiated micro-crystalline Ag ($4 \times 10^{14} \text{ cm}^{-2}$).

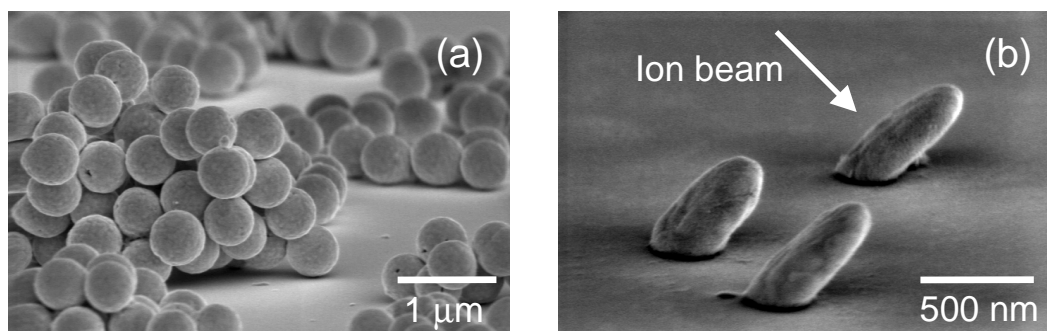


Figure 3.6 Side view SEM images (10° tilt) of metallo-dielectric SiO_2/Au core/shell colloids (silica core radius 205 nm, Au shell 63 nm) before irradiation (a), and after irradiation with 4 MeV Xe ion irradiation to a fluence of $1 \times 10^{15} \text{ cm}^{-2}$ at 90 K (b). The ion beam direction in (b) is indicated by the white arrow.

The fact that no deformation is observed in crystalline materials is consistent with earlier work on the deformation of thin foils.²² Within the thermal spike model of deformation, a crystalline material would not deform because of the large resistance to deformation due to the absence of ‘*shear sites*’, regions containing local free volume.²³ The molten region in the spike would then recrystallize so rapidly that it might not lead to deformation.

We note that the deformation of micro-crystalline ZnS colloids [Fig. 3.5(a)] may seem inconsistent with the argument that crystalline materials do not deform. However, these particles have amorphized under the ion beam, as was concluded from X-ray diffraction measurements after irradiation.

Figure 3.6(a) shows a side view SEM image (10° tilt) of unirradiated SiO_2/Au core/shell particles. The colloids consist of a silica core with a radius of 205 nm and a closed Au shell with a thickness of 63 nm. The size polydispersity of the colloid distribution is (3-5)%. Fig. 3.6(b) is a similar side view SEM image of these colloids after irradiation with 4 MeV Xe ions to a fluence of $1 \times 10^{15} \text{ Xe/cm}^2$. The core/shell particles have clearly deformed during ion irradiation. Since no deformation is observed for pure Au nanoparticles,²⁴ the induced deformation of the Au shells is thus brought about by the anisotropic deformation of the silica core. This *indirect* deformation process of Au shells makes it possible to fabricate anisotropic metallic shells that have interesting optical properties.

3.4 Conclusions

Spherical colloidal silica particles undergo anisotropic plastic deformation under 2-16 MeV Au irradiation. The size polydispersity is not affected by irradiation.

The transverse diameter increases exponentially with ion fluence at a rate that increases gradually with the average electronic energy loss in the colloid. Nonellipsoidal shapes are formed when the ion range is smaller than the colloid diameter. Anisotropic plastic deformation was also observed for micro-crystalline ZnS, ZnS/SiO₂ core/shell and amorphous TiO₂ particles. No deformation was found for single-crystalline Al₂O₃ and micro-crystalline Ag particles. Deformation was also found for metallo-dielectric SiO₂/Au core/shell particles, in which case the deformation of the Au shell is induced by the silica core. The data provide strong support for the thermal spike model for anisotropic deformation.

References

- ¹ M.-d. Hou, S. Klaumünzer, and G. Schumacher, *Phys. Rev. B* **41**, 1144 (1990)
- ² A. Benyagoub, S. Löffler, M. Rammensee, S. Klaumünzer, and G. Saemann-Ischenko, *Nucl. Instrum. Methods Phys. Res. B* **65**, 228 (1992)
- ³ S. Klaumünzer and A. Benyagoub, *Phys. Rev. B* **43**, 7502 (1991)
- ⁴ E. Snoeks, A. Polman, and C. A. Volkert, *Appl. Phys. Lett.* **65**, 2487 (1994)
- ⁵ M. L. Brongersma, E. Snoeks, T. van Dillen, and A. Polman, *J. Appl. Phys.* **88**, 59 (2000)
- ⁶ See Chapter 5 of this thesis.
- ⁷ H. Trinkaus and A. I. Ryazanov, *Phys. Rev. Lett.* **74**, 5072 (1995)
- ⁸ H. Trinkaus, *Nucl. Instrum. Methods Phys. Res. B* **146**, 204 (1998)
- ⁹ E. Snoeks, T. Weber, A. Cacciato, and A. Polman, *J. Appl. Phys.* **78**, 4723 (1995)
- ¹⁰ E. Snoeks, A. van Blaaderen, T. van Dillen, C. M. van Kats, M. L. Brongersma, and A. Polman, *Adv. Mater.* **12**, 1511 (2000)
- ¹¹ E. Snoeks, A. van Blaaderen, T. van Dillen, C. M. van Kats, K. Velikov, M. L. Brongersma, and A. Polman, *Nucl. Instrum. Methods Phys. Res. B* **178**, 62 (2001)
- ¹² A. van Blaaderen, J. van Geest, and A. Vrij, *J. Colloid Interface Sci.* **154**, 481 (1992)
- ¹³ M. Friedrich, W. Bürger, D. Henke, and S. Turuc, *Nucl. Instrum. Methods Phys. Res. A* **382**, 357 (1996)
- ¹⁴ J. F. Ziegler, J. P. Biersack, and U. Littmark, *The Stopping and Range of Ions in Solids* (Pergamon Press, New York, 1985)
- ¹⁵ A. van Blaaderen and A. P. M. Kentgens, *J. Non-Cryst. Solids* **149**, 161 (1992)
- ¹⁶ K. P. Velikov and A. van Blaaderen, *Langmuir* **17**, 4779 (2001)
- ¹⁷ S. M. Scholz, R. Vacassy, J. Dutta, H. Hofmann, and M. Akinc, *J. Appl. Phys.* **83**, 7860 (1998); S. M. Scholz, R. Vacassy, L. Lemaire, J. Dutta, and H. Hofmann, *Appl. Organometal. Chem.* **12**, 327 (1998)
- ¹⁸ J. H. Jean and T. A. Ring, *Langmuir* **2**, 251 (1986)
- ¹⁹ C. Graf and A. van Blaaderen, *Langmuir* **18**, 524 (2002)

- ²⁰ The error includes the error in the average determined from the size histogram and the pixel dimension in the digital SEM images.
- ²¹ For this fluence the ellipsoid is an (almost) oblate spheroid, as discussed in Chapter 2.
- ²² A. Benyagoub, S. Klaumünzer, L. Thomé, J. C. Dran, F. Garrido, and A. Dunlop, Nucl. Instrum. Methods Phys. Res. B **64**, 684 (1992)
- ²³ S. Klaumünzer, Changlin Li, S. Löffler, M. Rammensee, G. Schumacher, and H. Ch. Neitzert, Radiat. Eff. Defects Solids **108**, 131 (1989)
- ²⁴ We have irradiated Au nanoparticles of 15 nm in diameter with 30 MeV Se ions and observed no particle deformation using transmission electron microscopy.

4 *Ion irradiation-induced anisotropic plastic deformation at 300 keV*

Contrary to earlier predictions, ion irradiation at energies as low as 300 keV causes dramatic anisotropic plastic deformation of silica glass. Spherical colloidal silica particles with diameters of 125, 305 and 1030 nm were irradiated with Xe ions at energies in the range 0.3-4.0 MeV at temperatures between 85 K and 380 K. Irradiation-induced anisotropic plastic deformation changes the colloid shape from spherical into oblate ellipsoidal at a rate that strongly increases with ion energy. At a fixed fluence, the transverse diameter increases with electronic energy loss. Even at an energy as low as 300 keV large particle anisotropy was found (size aspect ratio of 1.43 at $1 \times 10^{15} \text{ cm}^{-2}$). The transverse plastic strain after irradiation gradually decreases with increasing irradiation temperature: it decreases by a factor 4.5 between 85 K and 380 K. The data are in agreement with a viscoelastic thermal spike model for anisotropic deformation.

4.1 Introduction

Amorphous materials subject to high-energy ion irradiation can undergo anisotropic plastic deformation at constant volume.¹⁻³ One of the most striking examples of this effect is the deformation of single colloidal particles under MeV ion irradiation.^{4,5} This effect is described in detail in Chapters 2 and 3. Spherical silica colloids expand perpendicular to the ion beam and contract parallel to the ion beam, changing their shape to oblate ellipsoidal. This ion beam deformation technique provides a unique method to tailor the shape of colloidal particles and aggregates. For example, as will be shown in Chapter 9, prolate ellipsoids can be made by using subsequent ion irradiations from different directions.⁴ Also, the optical properties of three-dimensional colloidal photonic crystals can be tailored by ion beam deformation.⁶ And recently we demonstrated how a colloidal mask for nanolithography can be modified by ion irradiation.⁷ With these different applications evolving, and in order to obtain fundamental understanding of the deformation process it becomes important to determine the critical parameters that determine the deformation rate.

In Chapter 3 we have shown that for 16 MeV Au irradiation the deformation rate (relative expansion per unit fluence) remains constant for increasing fluence, thus leading to an exponential growth of the transverse diameter with ion fluence.⁸ It was also shown that the deformation rate increases with ion energy for energies > 4 MeV. In fact, many studies on anisotropic deformation are performed at very high energies (several 100 MeV).³

A natural question that has remained open is what the lowest ion energy is at which anisotropic deformation occurs. Extrapolation of high-energy deformation data has suggested it will not occur below 1 MeV.^{3,8} In this chapter we study anisotropic deformation at Xe ion energies in the range 0.3-4 MeV. We find that significant deformation still occurs at energies as low as 300 keV, in contradiction with the earlier extrapolations. The transverse plastic strain increases with electronic energy loss of the Xe ions, with no or only a small threshold stopping. The deformation gradually decreases with increasing substrate temperature in the range 85–380 K. The results are in qualitative agreement with the mesoscopic viscoelastic model for anisotropic deformation as described in Chapter 5.

4.2 Experimental

Several dispersions of spherical colloidal silica particles were synthesized in solution using methods described in Ref. 9. A drop of the colloidal dispersion was dried on a Si(100) substrate leading to a coverage well below one

monolayer. The sample was mounted on a copper block of which the temperature was kept constant in the range 85 –380 K by cooling with liquid nitrogen or by resistive heating. Vacuum grease was used to improve the heat contact between sample and copper block. The colloidal particles were irradiated with Xe ions accelerated to energies in the range 0.3-4 MeV using a 1 MV Van de Graaff accelerator and a Xe charge state up to 4+. The samples were homogeneously irradiated to ion fluences as high as 1×10^{15} Xe/cm² by electrostatically scanning the ion beam through an aperture of 2.7×2.7 cm². The ion energy flux was kept constant at 0.04 W/cm² for all ion energies. All irradiations were performed at 45° with respect to the surface normal to enable investigation of the particles parallel and perpendicular to the ion beam. Scanning electron microscopy (SEM) using a 5 keV electron beam was used to determine the size and shape of the colloids before and after irradiation. The diameter of the unirradiated silica spheres was determined to be 125, 305 and 1030 nm, respectively, with a relative polydispersity $\leq 3\%$.

4.3 Results and discussion

Figure 4.1(a) shows a SEM image taken after 4 MeV Xe irradiation of 305-nm diameter silica colloids to a fluence of 1×10^{15} cm⁻² at a temperature of 85 K. The image is taken perpendicular to the ion beam. The dashed sphere indicates the original perimeter of the colloid before irradiation. It can clearly be seen that the colloid has expanded perpendicular to the ion beam and contracted parallel to the ion beam. The apparent colloid size aspect ratio (major over minor axis) is 2.52. SEM studies presented in Chapter 2 show that during ion irradiation at 45°, the colloids perform a gradual angular “roll-off” with respect to the perpendicular ion beam direction.⁵ For the sample in Fig. 4.1(a) the angle between the colloid’s minor axis and the ion beam is $15^\circ \pm 1^\circ$, upon completion of the irradiation. Taking this effect into account in the SEM projection, the actual size aspect ratio is calculated to be 3.21 ± 0.20 . No significant volume change is observed upon irradiation.

Figure 4.1(b) shows a SEM image taken after irradiation at a lower Xe ion energy of 1 MeV (1×10^{15} cm⁻²). The size aspect ratio determined from the SEM analysis (after correcting for the roll-off angle of 6°) is 1.84 ± 0.05 . This shows the anisotropic deformation process is strongly dependent on the ion energy used, in agreement with data in Chapter 3 and experiments performed at much higher energies.³

Figures 4.1(c,d) show silica colloids after irradiation at an even lower energy of 300 keV. It can clearly be seen that the shape of the colloids in Fig. 4.1(c) is nonellipsoidal. This is due to the fact that the projected Xe ion range (136 nm as calculated using a Monte Carlo simulation program¹⁰) is much smaller than the original colloid diameter of 305 nm. Only the ion-modified top

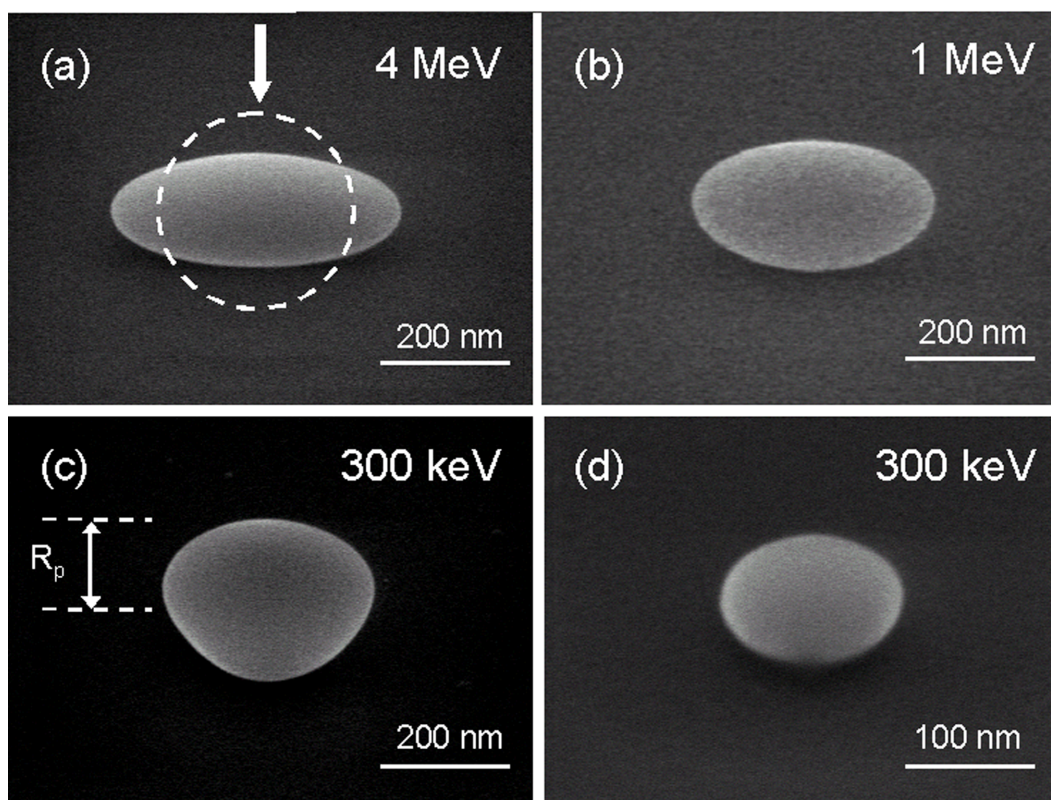


Figure 4.1: Scanning electron microscopy images of silica colloids after Xe ion irradiation to a fluence of $1 \times 10^{15} \text{ cm}^{-2}$ at an energy of 4 MeV **(a)**, 1 MeV **(b)** and 300 keV **(c,d)**. Irradiations were performed at a temperature of 85 K and at an angle of 45° . All images are taken perpendicular to the ion beam. The arrow in **(a)** indicates the ion beam direction. The dashed circle in **(a)** with a diameter of 305 nm represents the original spherical size before irradiation for **(a)**, **(b)** and **(c)**. The diameter of the colloids used in **(d)** is 125 nm. The mean projected ion range R_p for 300 keV Xe is indicated in **(c)**. Note the different scale bar in **(d)**.

part of the colloid has deformed. Additional experiments were then performed with colloids having a diameter of 125 nm, smaller than the ion range. These do have an ellipsoidal shape after irradiation as can be seen in Fig 4.1(d). The size aspect ratio of these colloids is 1.43 ± 0.04 , again without observable volume change.

The fact that considerable deformation is observed at Xe ion energies as low as 300 keV is striking. The typical deformation rate, defined as the differential length change perpendicular to the ion beam per unit fluence, is $A = 1 \times 10^{-16} \text{ cm}^2/\text{ion}$: at this rate a 300 keV Xe fluence of 10^{14} cm^{-2} will result in a transverse expansion of 1 %.

For 300 keV and 4 MeV Xe ions the average total energy lost in atomic and electronic stopping processes¹⁰ in silica is roughly identical ($\sim 2.3 \text{ keV/nm}$). In this energy range, the electronic stopping F_e increases monotonically with ion

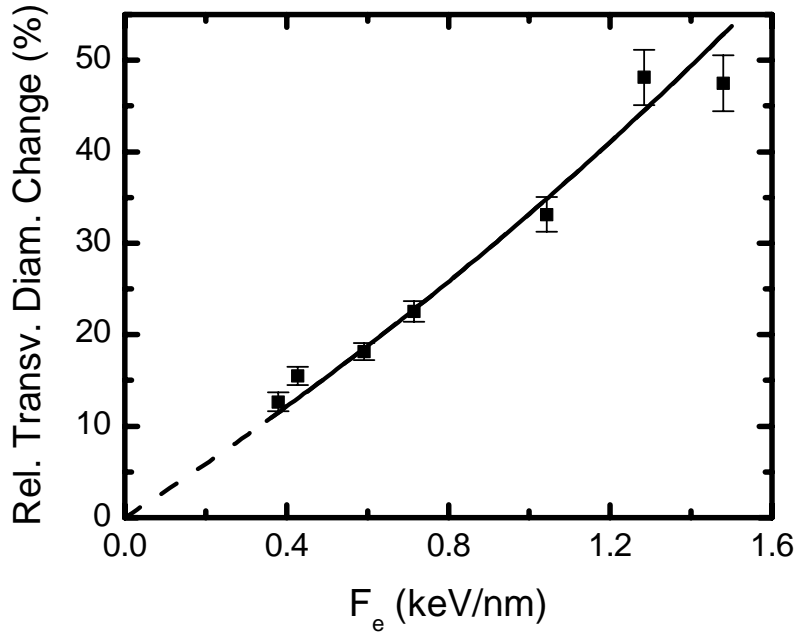


Figure 4.2: Relative transverse diameter change of the silica colloids as a function of average electronic energy loss F_e at a fixed fluence of $1 \times 10^{15} \text{ cm}^{-2}$ at 85 K. The data are determined from the colloid deformation after Xe irradiation with energies in the range between 300 keV and 4.0 MeV. The original diameter of the colloids was 305 nm for all irradiations, except for the 300 keV irradiation, where the original diameter was 125 nm [Fig. 4.1(d)]. The solid line is a fit to the data using $\varepsilon_T = \exp(A\phi) - 1$ and Eq. (4.1) taken from a viscoelastic model. The dashed line represents the extrapolation of this model to small F_e .

energy, the nuclear stopping decreases correspondingly. Since the deformation increases with ion energy it must therefore be mainly dependent on the electronic stopping. This is consistent with earlier work at very high energy.³ Figure 4.2 shows the relative increase of the transverse diameter as a function of the average electronic stopping of the Xe ions in the silica colloids, measured at a fixed fluence of $1 \times 10^{15} \text{ Xe/cm}^2$. All data were taken at a constant temperature of 85 K. For this experiment we used 0.3, 0.5, 0.75, 1.0, 2.0, 3.0 and 4.0 MeV Xe ions. The data in Fig. 4.2 were determined from deformation experiments on 305 nm-diameter colloids [e.g. Fig. 4.1(a) and (b)] except for the 300 keV Xe irradiation, where the deformation was determined on 125 nm-diameter colloids [Fig. 4.1(d)]. As can be seen in Fig. 4.2 the transverse plastic strain gradually increases with F_e (solid squares).

Trinka *et al.* have proposed a model to explain the ion irradiation-induced deformation phenomena in terms of a viscoelastic thermal spike model.^{11,12} In Chapter 5 we present a more general, viscoelastic model for time-dependent viscous flow in ion tracks to describe the macroscopic deformation

process. In this model the deformation is attributed to the high degree of anisotropy of the ion-induced thermal spike. Within this viscoelastic model two factors determine the energy dependence of the deformation. First of all, at low energy the ion trajectory angle is distributed due to Rutherford scattering that is quite prominent (high nuclear stopping), leading to less anisotropic deformation. At 300 keV the average angular variation over the colloid thickness is below 15° and thus the angular anisotropy is relatively small. Second, ions with a higher energy and thus a higher electronic stopping F_e induce a larger thermal spike cross section, and thus a larger deformation strain rate A .

Within the viscoelastic thermal spike model, the transverse plastic strain rate A (per unit fluence) is given by (see Eq. (5.6.11) in Chapter 5):

$$A = \frac{1.26}{e} \frac{1+\nu}{5-4\nu} \frac{\alpha}{\rho C} F_e, \quad (4.1)$$

with $e=2.72$, ν Poisson's ratio (typically 0.2 for silica), α the linear thermal expansion coefficient, ρ the density and C the specific heat of the target material. Eq. (4.1) holds for low enough substrate temperatures to ensure freezing-in of the local viscous strain and high enough values of F_e to ensure cylindrical symmetry of the thermal spike. For a constant strain rate A during irradiation, the transverse diameter should increase exponentially with ion fluence ϕ . In that case the transverse plastic strain is given by: $\varepsilon_T = \exp(A\phi) - 1$. The solid line in Fig. 4.2 is a fit of the transverse strain data using this relation and Eq. (4.1) and $\phi = 1 \times 10^{15} \text{ cm}^{-2}$. The model provides a very good description of the data for $\alpha/\rho C = 1.4 \times 10^{-12} \text{ m}^3/\text{J}$. For typical values of $\rho = 2.0 \text{ g/cm}^3$ and $C = 10^3 \text{ Jkg}^{-1}\text{K}^{-1}$, this results in a value of $\alpha = 2.8 \times 10^{-6} \text{ K}^{-1}$ for the colloidal silica, a reasonable value.

These data imply that anisotropic deformation is a general phenomenon that must be taken into account even in the tens-hundreds of keV energy range that is commonly used in many experiments and technological applications. Previous high-energy irradiation experiments indicated an apparent threshold value for the electronic stopping in the order of 1 keV/nm below which no deformation would be expected.^{3,8} Our data show that deformation occurs well below this value and in fact the model that fits the data well does not predict such a threshold (dashed line, Fig. 4.2). Ion beam-induced deformation is thus expected at energies well below 300 keV, although it should be noted that for low energy Eq. (4.1) must be corrected for angular straggle. More measurements are needed to study this in detail.

We have also studied the dependence of the deformation process on irradiation substrate temperature. Spherical silica colloids with a diameter of 1030 nm were irradiated with 4 MeV Xe ions to a fluence of $4 \times 10^{14} \text{ cm}^{-2}$ at temperatures in the range of 85 – 380 K. Figure 4.3 shows the relative transverse diameter change as a function of temperature.

As can be seen, the transverse plastic strain gradually decreases with increasing temperature. It is about 4.5 times less at 380 K than at 85 K. A similar

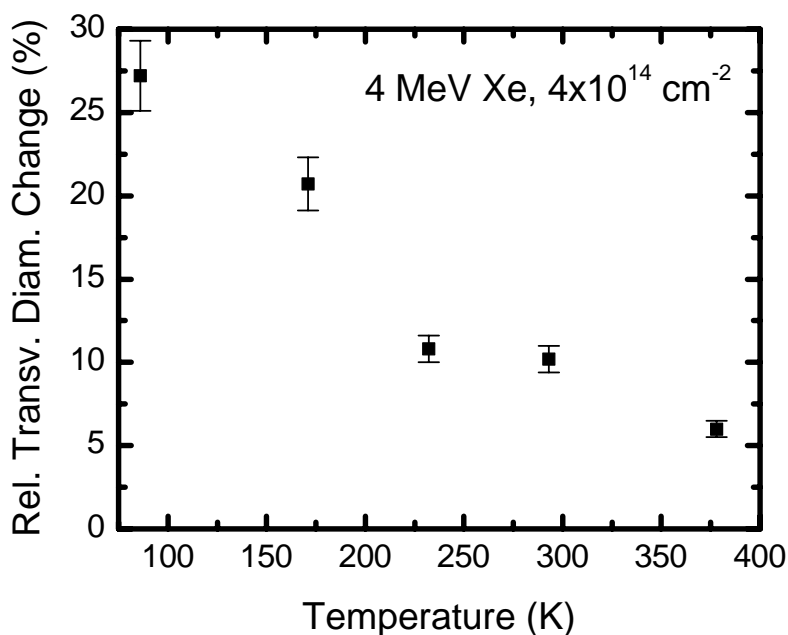


Figure 4.3: Relative transverse diameter change of 1030 nm-diameter silica colloids as a function of sample temperature measured after irradiation with 4 MeV Xe to a fluence of $4 \times 10^{14} \text{ cm}^{-2}$.

temperature dependence has been observed for the deformation of thin foils of vitreous silica and metallic glasses at very high energies.^{1,3} Within the viscoelastic model the decrease in deformation with increasing substrate temperature is attributed to the relaxation of the strained ion tracks that are under compression due to the interaction with the surrounding silica matrix, as discussed in Chapter 5 and Ref. 12. The local compressive stress would be partly relaxed at a rate determined by the reduced viscosity of the silica at elevated substrate temperature. This relaxation is more efficient at higher irradiation temperatures, therefore reducing the net amount of anisotropic deformation as observed in Fig. 4.3. It should be noted that under high-flux irradiation (beam fluxes much higher than used in this study), sample heating may also lead to reduced anisotropic deformation.¹³

4.4 Conclusions

Ion irradiation-induced anisotropic plastic deformation of colloidal silica particles occurs at energies as low as 300 keV. The deformation strain at 300 keV is 1 % for each Xe fluence of $10^{14} \text{ ions/cm}^2$. In the energy range 300 keV-4 MeV, the transverse strain increases with electronic stopping, without indication

of a threshold. The transverse expansion gradually decreases with increasing substrate temperature. The data can be explained by a viscoelastic model for local shear stress relaxation in the high-temperature ion-induced thermal spike (Chapter 5). With this observation the deformation of a wide variety of colloidal materials becomes possible using readily available accelerator energies.

References

- ¹ S. Klaumünzer and G. Schumacher, Phys. Rev. Lett. **51**, 1987 (1983)
- ² M.-d. Hou, S. Klaumünzer, and G. Schumacher, Phys. Rev. B **41**, 1144 (1990)
- ³ A. Benyagoub, S. Löffler, M. Rammensee, S. Klaumünzer, and G. Saemann-Ischenko, Nucl. Instrum. Methods Phys. Res. B **65**, 228 (1992)
- ⁴ E. Snoeks, A. van Blaaderen, T. van Dillen, C.M. van Kats, M. L. Brongersma, and A. Polman, Adv. Mater. **12**, 1511 (2000)
- ⁵ T. van Dillen, E. Snoeks, W. Fukarek, C. M. van Kats, K. P. Velikov, A. van Blaaderen, and A. Polman, Nucl. Instrum. Methods Phys. Res. B **175-177**, 350 (2001)
- ⁶ K. P. Velikov, T. van Dillen, A. Polman, and A. van Blaaderen, Appl. Phys. Lett. **81**, 838 (2002)
- ⁷ E. Snoeks, A. van Blaaderen, T. van Dillen, C. M. van Kats, K. Velikov, M. L. Brongersma, and A. Polman, Nucl. Instrum. Methods Phys. Res. B **178**, 62 (2001)
- ⁸ T. van Dillen, A. Polman, W. Fukarek, and A. van Blaaderen, Appl. Phys. Lett. **78**, 910 (2001)
- ⁹ A. van Blaaderen and A. Vrij, Langmuir **8**, 2921 (1993)
- ¹⁰ J.F. Ziegler, J.P. Biersack, and U. Littmark, *The Stopping and Range of Ions in Solids* (Pergamon, New York, 1985)
- ¹¹ H. Trinkaus and A.I. Ryazanov, Phys. Rev. Lett. **74**, 5072 (1995)
- ¹² H. Trinkaus, Nucl. Instrum. Methods Phys. Res. B **146**, 204 (1998)
- ¹³ Such a beam heating effect caused by high beam current and possibly poor heat contact between sample and substrate holder is most likely the origin of an earlier claim that deformation would not occur at 500 keV Xe irradiation (Ref. 4).

5 *Anisotropic plastic deformation by viscous flow in ion tracks*

A model describing the origin of ion beam induced anisotropic plastic deformation is derived and discussed. It is based on a viscoelastic thermal spike model for viscous flow in single ion tracks derived by Trinkaus et al. Deviatoric (shear) stresses, brought about by the rapid thermal expansion of the thermal spike, relax at ion track temperatures beyond a certain flow temperature. Shear stress relaxation is accompanied by the generation of viscous strains. The model introduces differential equations describing the time evolution of the radial and axial stresses, enabling an exact derivation of the viscous strains for any ion track temperature history $T(t)$. It is shown that the viscous strains effectively freeze in for large track cooling rates, whereas reverse viscous flow reduces the net viscous strains in the ion track for smaller cooling rates. The model is extended to include finite-size effects that occur for ion tracks close to the sample edge, enabling comparison with experimental results for systems with small size. The 'effective flow temperature approach', that was earlier introduced by Trinkaus et al. by making use of Eshelby's theory of elastic inclusions, follows directly from the viscoelastic model as a limiting case. We show that the viscous strains in single ion tracks are the origin of the macroscopic anisotropic deformation process. The macroscopic deformation rate can be directly found by superposing the effects of single ion impacts. By taking realistic materials parameters, model calculations are performed for experimentally studied cases. Qualitative agreement is observed.

5.1 Introduction

Stress-free amorphous materials subjected to irradiation with ions at energies of ~ 100 keV and higher exhibit anisotropic plastic flow.¹⁻⁷ The anisotropy is related to the direction of the ion beam: materials expand perpendicular to the ion beam and contract parallel to the ion beam while maintaining their volume. The anisotropic deformation is most pronounced at low temperatures (< 100 K) and decreases with increasing irradiation temperature.^{4,7} The deformation increases with ion fluence at a constant rate, without saturation. It is well established that the deformation is mainly driven by electronic excitations rather than the atomic displacements induced by the ion beam.

Anisotropic deformation has been experimentally investigated in great detail for thin foils of silica and metallic glasses.^{3,4} Recently, MeV ion irradiation of micron-sized colloidal silica particles was used to change the colloids' shape from spherical to oblate ellipsoidal.⁶⁻⁸ The ion irradiation induced-anisotropic deformation technique is now a well-established tool to tailor the shape of nanoscale and microscale structures. It has led to many applications, such as the tailoring of lithographic as well as colloidal nanomasks, tuning the optical bandgap of colloidal photonic crystals, tailoring the plasmon resonance in metallo-dielectric colloids, and controlling the anisotropy of colloidal particles for use in colloidal ordering studies, as will be shown in Chapter 9.^{9,10}

One of the most successful attempts to describe the deformation process with many of its characteristics is the viscoelastic model derived by Trinkaus *et al.*¹¹⁻¹⁴ This model, also known as the “*effective flow temperature approach*”, describes the viscous relaxation of shear stresses in the ion track, brought about by the rapid thermal expansion of the cylindrical thermal spike induced by the ion. Complete stress relaxation in the ion track is assumed to take place when the ion track temperature exceeds a certain flow temperature T^* . Trinkaus *et al.* use Eshelby's theory of ellipsoidal elastic inclusions in elastically isotropic media to calculate the viscous shear strains and assume these to freeze in upon rapid cooling so as to produce the overall anisotropic deformation.¹¹ The aim of the current chapter is to analyze in detail this stress relaxation process, focusing on the spatial evolution of stress and strain as a function of temperature and time. Along the way, due attention is paid to boundary conditions and approximations.

This chapter is organized as follows. After defining the proper type of viscoelastic model and describing the equations and boundary conditions governing the viscous flow in ion tracks (Sect. 5.2), we will first analyze the stresses and strains that develop upon initial thermal loading (Sect. 5.3). Subsequently, in Sect. 5.4, we will study viscous relaxation by deriving a set of

differential equations describing the evolution of the stresses and the viscous strains in ion tracks. This will lead to a general closed-form solution for the viscous strains. Based on these general solutions we will show in Sect. 5.5 some examples of time-dependent flow in ion tracks and compare our results with the “*effective flow temperature approach*” approximation. We will also show that ion tracks close to a sample edge exhibit reduced viscous flow compared to ion tracks situated far away from the edges. This result enables comparison with experiments performed on nanoscale systems with dimensions comparable to that of the ion track. In Sect. 5.6 we will show that the macroscopic deformation (as the result of multiple ion tracks) can be calculated directly from our mesoscopic model, without the necessity of calculating the volume average of the total strain. Finally, in Sect. 5.7, we will compare the calculated macroscopic deformation rate for silica glass with experimental values.

5.2 Formulation of the model

When an ion penetrates a solid it is slowed down by nuclear and electronic stopping processes.¹⁵ Anisotropic deformation is mainly dependent on the electronic energy loss F_e . This excitation/ionization process takes place within 10^{-16} s. After local thermalization of the electronic subsystem, energy is transferred from the electronic to the atomic subsystem (electron-phonon coupling)¹⁶ at time scales in the range 10^{-14} - 10^{-12} s. The rapid thermal expansion of the track results in large shear stresses in the heated region. For high F_e the heated region around the ion track may become fluid. Due to the reduced viscosity the thermally induced shear stresses relax, resulting in viscous expansion in the plane perpendicular to the ion track. After $\sim 10^{-10}$ to 10^{-9} s the thermal spike has cooled down to the irradiation (substrate) temperature. For high cooling rates inside the thermal spike, the viscous strain freezes in, leading to anisotropic deformation.¹¹ In order to describe the viscous flow in ion tracks we now, for the first time, explicitly formulate the assumptions, make the proper choice of viscoelastic model, write down all governing equations and solve them under appropriate approximations and boundary conditions as listed below:

1. The electronic stopping F_e is energy-dependent and thus changes as a function of depth. However, for high enough ion energies and small enough target thicknesses this depth-dependence can be neglected. Indeed, for MeV ion irradiation of colloidal silica particles and the high-energy ion irradiation of thin foils of metallic and silica glasses the variation of F_e with depth is only small. Consequently, also the resulting track temperature T is independent of depth.¹⁷

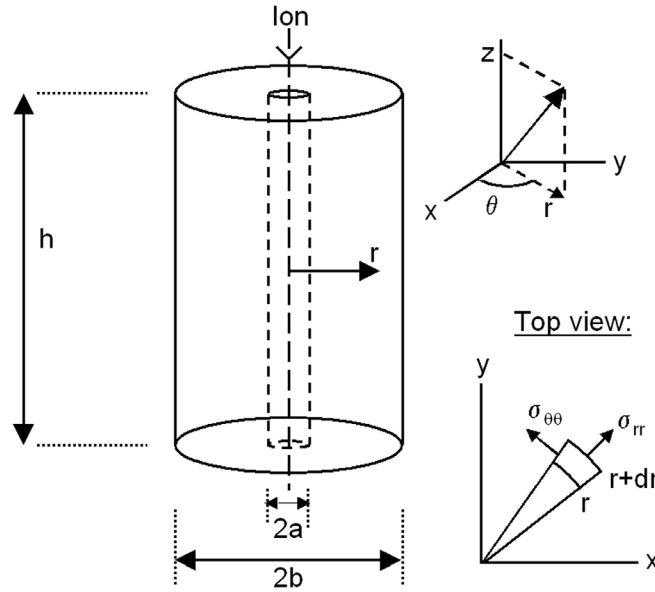


Figure 5.1 Geometry of a cylindrical ion track of radius a in a disk (sample) with radius b and height h . The cylindrical coordinates r , θ , z are indicated in the figure as well as the stress components σ_{rr} and $\sigma_{\theta\theta}$.

2. Toulemonde *et al.* have calculated the space-time evolution of the temperature distribution in the thermal spike by solving the heat flow equations in the electronic and atomic subsystems that are coupled by the electron-phonon interaction.^{16,18,19} It is found that the track temperature $T(r,t)$ (r is the radial coordinate measured from the center of the track) can rise up to several thousand K. In this article we will not take into account these “exact” temperature profiles, but assume that the time-dependent temperature in a cylinder around the ion track ($r \leq a$) is uniform (i.e., independent of r). The radius of the cylinder, a , is determined by the so-called flow temperature T^* , the temperature at which the material shows fluid-like behavior at time scales of the thermal spike.^{13, 14}

The geometry of the ion track in the sample is schematically depicted in Figure 5.1. The sample is modeled as a cylindrical disk of height h and radius b . An ion penetrates the sample at $r=0$ (along the z -axis). As a result of assumptions 1 and 2, a cylindrical region of fixed radius a is uniformly heated. By virtue of the cylindrical geometry of the sketched problem we will use cylindrical coordinates r , θ and z (see Fig. 5.1).

3. The radius a of the thermal spike is typically on the order of several nm.¹⁹ The height h of the sample, however, is on the order of several μm . The aspect ratio of the cylinder, h/a , thus is typically $>10^3$. This suggests that the ion track geometry can be described by an infinitely long cylinder of radius a inside a matrix of radius b . As a result, at each time during the deformation process, planes remain flat (axial displacement u_z independent of r), while the axial

strain, $\varepsilon_{zz} = \partial u_z / \partial z$, is independent of z . This condition is known as *generalized plane strain*. We will show that for $b \rightarrow \infty$ the axial strain vanishes, a condition known as *plane strain*.

4. The *equations of motion* describing the evolution of a velocity field v_i in a stress field with components σ_{ij} , are given by (neglecting body forces) $\rho \partial v_i / \partial t = \partial \sigma_{ij} / \partial x_j$, where we have used Einstein's summation convention and where ρ is the mass density. The inertia forces are only important for describing the emission of elastic waves during the initial stage of the thermal spike and are neglected here. This yields the equations of equilibrium

$$\frac{\partial \sigma_{ij}}{\partial x_j} = 0. \quad (5.2.1)$$

5. To describe anisotropic deformation as a result of the shear stress relaxation by viscous flow in ion tracks, it is important to make the proper choice for the stress-strain relations. The commonly used viscoelastic models are the Kelvin/Voigt model, used in Refs. 20, 21 and Maxwell's model used by Trinkaus *et al.*¹⁴ In the former model a spring (elastic, Hookean element) and a dashpot (viscous, Newtonian element) are coupled in parallel, while they are placed in series in the Maxwell model.

The Kelvin/Voigt model does not allow for complete stress relaxation because of the constraint imposed by the elastic, Hookean element. We here choose Maxwell's model in which shear stresses can be relaxed at reduced viscosities leading to concomitant viscous strains. The latter then are the origin of the anisotropic plastic deformation. In Maxwell's model the total strain ε_{ij} is a superposition of elastic (ε_{ij}^e), viscous (ε_{ij}^v) and thermal strains (ε_{ij}^{th}), that is

$$\varepsilon_{ij} = \varepsilon_{ij}^e + \varepsilon_{ij}^v + \varepsilon_{ij}^{th}, \quad (5.2.2)$$

while it is related to the displacement field u_i in the following way:

$$\varepsilon_{ij} = \frac{1}{2} \left(\frac{\partial u_i}{\partial x_j} + \frac{\partial u_j}{\partial x_i} \right). \quad (5.2.3)$$

For isotropic elastic media, the elastic strain tensor ε_{ij}^e is coupled to the stress tensor σ_{ij} by Hooke's law:

$$\varepsilon_{ij}^e = \frac{1}{2\mu} \left(\sigma_{ij} - \frac{\nu}{1+\nu} \sigma_{kk} \delta_{ij} \right), \quad (5.2.4)$$

where $\mu = E / [2(1+\nu)]$ is the shear modulus, and E and ν are Young's modulus and Poisson's ratio, respectively. In Eq. (5.2.4) $\sigma_{kk} = \sigma_{11} + \sigma_{22} + \sigma_{33}$ is the hydrostatic stress (negative pressure), and δ_{ij} is the Kronecker-delta ($\delta_{ij} = 1$ for $i=j$, $\delta_{ij} = 0$ for

$i \neq j$). The elastic behavior of the material is therefore described by two independent material parameters E and ν .²²

The inelastic behavior of the material is described by volume-conserving Newtonian viscous flow through

$$\frac{d\varepsilon_{ij}^v}{dt} \equiv \dot{\varepsilon}_{ij}^v = \frac{1}{2\eta} s_{ij} \quad , \quad (5.2.5)$$

where

$$s_{ij} \equiv \sigma_{ij} - \frac{1}{3} \sigma_{kk} \delta_{ij} \quad (5.2.6)$$

are the components of the stress deviator and η is the material's shear viscosity, which is strongly temperature dependent. Note that viscous flow can occur only in a non-hydrostatic (i.e. deviatoric) stress state, $s_{ij} \neq 0$. This is the basis for the phenomenon of shear stress relaxation, although it should be noted that not the shear stresses are relaxed, but the deviatoric stresses.²³

Finally, the last term in Eq. (5.2.2) concerns the thermal strains ε_{ij}^{th} , which are given by:

$$\varepsilon_{ij}^{th} = \alpha \Delta T \delta_{ij} \quad , \quad (5.2.7)$$

where α is the coefficient of linear thermal expansion and $\Delta T = T - T_s$ is the difference between the ion track cylinder's temperature T and the temperature of the substrate T_s .

The governing equations (5.2.1) to (5.2.7) describe shear stress relaxation through viscous flow inside the ion tracks. When an ion penetrates the sample it rapidly heats up a cylinder of radius a . Due to the mismatch in thermal straining (the elastic cylinder around the ion track remains at the substrate temperature T_s , so that $\varepsilon_{ij}^{th} = 0$ for $r > a$) and the geometry of the ion track, non-hydrostatic stresses build up. Above a so-defined flow temperature T^* , the viscosity $\eta(T)$ inside the ion track cylinder is low enough for the deviatoric stresses to relax, thus introducing viscous strains. Since heating of the ion track cylinder occurs at a time scale within $\sim 10^{-12}$ s, i.e. much smaller than the time scale of viscous flow, the heating can be taken as instantaneous. Therefore, we split the analysis in two parts: a *thermal loading* part (Sect. 5.3), describing the generation of internal stresses due an instantaneous temperature increase ΔT (at $t=0$) in the ion track, and a *viscous relaxation* part (Sect. 5.4), describing stress relaxation and the associated viscous flow determined by the temperature evolution $\Delta T(t)$.

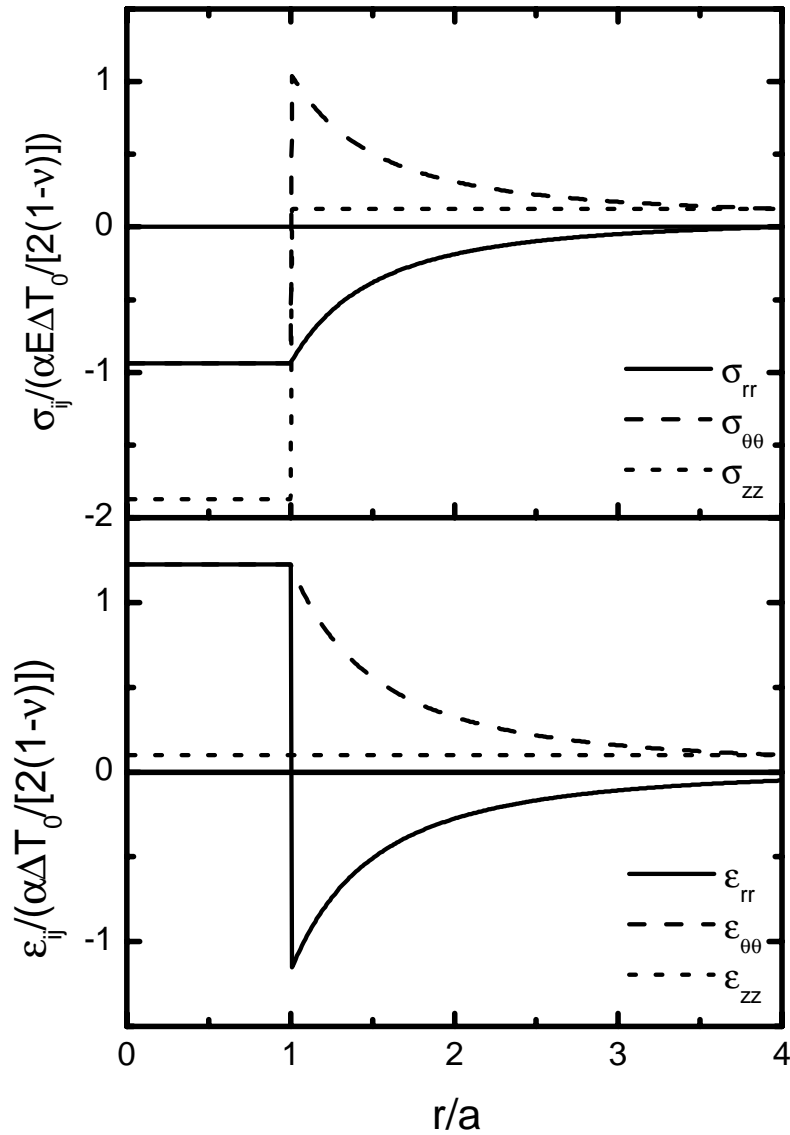


Figure 5.2 Distribution of the stresses σ_{rr} , $\sigma_{\theta\theta}$ and σ_{zz} (a), and the strains ϵ_{rr} , $\epsilon_{\theta\theta}$ and ϵ_{zz} (b) after instantaneous heating and expansion of the ion track cylinder, as a function of r/a [Eqs. (5.3.6) and (5.3.7)]. Results are plotted for $\nu=0.2$ and $b=4a$ ($\delta=0.25$).

5.3 Initial state: instantaneous thermal loading

The instantaneous thermal loading is a thermoelastic problem that can be solved by starting from the equations of equilibrium (5.2.1). In case of cylindrical symmetry (no dependence on circumferential angle θ), only a single equilibrium condition is left:²⁴

$$\frac{d\sigma_{rr}}{dr} + \frac{\sigma_{rr} - \sigma_{\theta\theta}}{r} = 0 \quad . \quad (5.3.1)$$

The direction of the stresses σ_{rr} (radial) and $\sigma_{\theta\theta}$ (hoop) are shown in Fig. 5.1. The shear stresses $\sigma_{r\theta}$, σ_{rz} and $\sigma_{\theta z}$ vanish due to the cylindrical symmetry. In the absence of viscous flow the stress-strain relations given by Eqs. (5.2.2), (5.2.4) and (5.2.7) reduce to

$$\begin{aligned} \varepsilon_{rr} &= \frac{1}{E} [\sigma_{rr} - \nu(\sigma_{\theta\theta} + \sigma_{zz})] + \alpha\Delta T \\ \varepsilon_{\theta\theta} &= \frac{1}{E} [\sigma_{\theta\theta} - \nu(\sigma_{rr} + \sigma_{zz})] + \alpha\Delta T \quad . \\ \varepsilon_{zz} &= \frac{1}{E} [\sigma_{zz} - \nu(\sigma_{rr} + \sigma_{\theta\theta})] + \alpha\Delta T \end{aligned} \quad (5.3.2)$$

For cylindrical symmetry the radial and hoop total strains ε_{rr} and $\varepsilon_{\theta\theta}$ are determined solely by the radial displacement u_r through

$$\varepsilon_{rr} = \frac{du_r}{dr} \quad , \quad \varepsilon_{\theta\theta} = \frac{u_r}{r} \quad . \quad (5.3.3)$$

In the absence of external forces, the total force in the axial direction, F_z , should vanish:

$$F_z = \int_0^b \sigma_{zz}(r) 2\pi r dr = 0 \quad . \quad (5.3.4)$$

With Eq. (5.3.4) and the traction-free boundary condition $\sigma_{rr}(r=b)=0$, the solutions of Eqs. (5.3.1), (5.3.2) and (5.3.3) for the normal stress components are found as:²⁴

$$\begin{aligned} \sigma_{rr}(r) &= \frac{\alpha E}{1-\nu} \left[\frac{1}{b^2} \int_0^b \Delta T(r') r' dr' - \frac{1}{r^2} \int_0^r \Delta T(r') r' dr' \right] \\ \sigma_{\theta\theta}(r) &= \frac{\alpha E}{1-\nu} \left[-\Delta T(r) + \frac{1}{b^2} \int_0^b \Delta T(r') r' dr' + \frac{1}{r^2} \int_0^r \Delta T(r') r' dr' \right] \quad . \\ \sigma_{zz}(r) &= \frac{\alpha E}{1-\nu} \left[\frac{2}{b^2} \int_0^b \Delta T(r') r' dr' - \Delta T(r) \right] \end{aligned} \quad (5.3.5)$$

We assume a uniform temperature distribution within the thermal spike region and thus the ion track cylinder of radius a is homogeneously heated to T_{max} ($\Delta T = T_{max} - T_s \equiv \Delta T_0$ for $r \leq a$) while the surrounding material remains at the temperature T_s ($\Delta T = 0$ for $a < r \leq b$). For this specific temperature profile, the

stresses inside the ion track cylinder ($r \leq a$) from Eqs. (5.3.5) and the corresponding strains from (5.3.2) are found to be

$$\begin{aligned} \sigma_{rr} = \sigma_{\theta\theta} = \frac{1}{2} \sigma_{zz} &= -\frac{\alpha E \Delta T_0}{2(1-\nu)} (1 - \delta^2) \\ \varepsilon_{rr} = \varepsilon_{\theta\theta} &= \frac{(1+\nu) + \delta^2(1-3\nu)}{2(1-\nu)} \alpha \Delta T_0 \quad , \quad \varepsilon_{zz} = \alpha \Delta T_0 \delta^2 \end{aligned} \quad (5.3.6)$$

where $\delta \equiv a/b$. The result for $a < r \leq b$ is given by²⁵

$$\begin{aligned} \sigma_{rr} &= -\frac{\alpha E \Delta T_0}{2(1-\nu)} \left[\left(\frac{a}{r} \right)^2 - \delta^2 \right] ; \quad \sigma_{\theta\theta} = \frac{\alpha E \Delta T_0}{2(1-\nu)} \left[\left(\frac{a}{r} \right)^2 + \delta^2 \right] \\ \sigma_{zz} &= \frac{\alpha E \Delta T_0}{(1-\nu)} \delta^2 \\ \varepsilon_{rr} &= -\frac{\alpha \Delta T_0}{2(1-\nu)} \left[(1+\nu) \left(\frac{a}{r} \right)^2 - (1-3\nu) \delta^2 \right] \\ \varepsilon_{\theta\theta} &= \frac{\alpha \Delta T_0}{2(1-\nu)} \left[(1+\nu) \left(\frac{a}{r} \right)^2 + (1-3\nu) \delta^2 \right] ; \quad \varepsilon_{zz} = \alpha \Delta T_0 \delta^2 \end{aligned} \quad (5.3.7)$$

Eqs. (5.3.6) and (5.3.7) fully characterize the stress-strain distribution in the thermal spike and its surrounding material upon instantaneous heating. Figures 5.2(a) and (b) show the stress and strain distributions respectively, calculated using Eqs. (5.3.6) and (5.3.7) for $\delta=0.25$ and $\nu=0.2$. The stresses are normalized with $\alpha E \Delta T_0 / [2(1-\nu)]$ and the strains with $\alpha \Delta T_0 / [2(1-\nu)]$. Figure 5.2(a) shows that the (compressive) stresses are uniform inside the cylinder of radius a . This result also follows from Eshelby's theory of ellipsoidal elastic inclusions as adopted by Trinkaus.¹¹ The axial stress (σ_{zz}) is compressive and is twice as large as the in-plane compressive stresses (σ_{rr} , $\sigma_{\theta\theta}$). Since the stress tensor is non-hydrostatic, there are deviatoric stresses s_{ij} , which follow from (5.2.6) and (5.3.6) to be

$$s_{rr} = s_{\theta\theta} = -\frac{1}{2} s_{zz} = \frac{\alpha E \Delta T_0}{6(1-\nu)} (1 - \delta^2) \quad (5.3.8)$$

These deviatoric stresses are the driving force for viscous straining according to Eq. (5.2.5), which will generate negative viscous strains in axial direction and positive viscous strains in radial and hoop directions. The details of this relaxation process will be the subject of the next two sections.

In the surrounding material ($a < r \leq b$) the stresses and strains decay as $1/r^2$. These solutions are identical to the well-known elastic solution for a thick-walled cylinder under internal pressure.²⁴ Note that for finite δ the radial stress

vanishes at $r=b$, whereas the hoop stress does not, while $\sigma_{rr} + \sigma_{\theta\theta}$ is uniform in $a < r \leq b$.

Figure 5.2(b) shows that within the heated region, $r \leq a$, the strains are uniform. The axial strain ε_{zz} is indeed constant as was imposed by the condition of “generalized plane strain” (Sect. 5.2). For $\delta \rightarrow 0$ it follows from Eqs. (5.3.6) and (5.3.7) that $\varepsilon_{zz}=0$, i.e. “plane strain”.

The stress and strain distributions shown in Fig. 5.2 are the initial conditions (at $t=0$) for the time-dependent viscous flow in the ion track cylinder, as described next.

5.4 General time-dependent solution for viscous flow in single ion tracks

After the initial instantaneous heating at $t=0$, the deviatoric stresses inside the ion track cylinder ($r \leq a$) may relax as long as the ion track temperature is above the flow temperature, i.e. $T > T^*$. The governing equations for this stage are different than those leading to the solution discussed in Sect. (5.3), since now the viscous contribution (5.2.5) to the strain (5.2.2) needs to be considered.

The equilibrium condition (5.3.1) is, in general, not sufficient to determine the stress fields, but we can make use of the structure of the initial solution found in Sect. 5.3. Inside the ion track ($r \leq a$), $\sigma_{rr}(r;t=0)$ and $\sigma_{\theta\theta}(r;t=0)$ are uniform and equal. Since this holds for the initial state, the equilibrium condition (5.3.1) remains satisfied identically when

$$\sigma_{rr}(r;t) = \sigma_{\theta\theta}(r;t) = c(t) \quad . \quad (5.4.1)$$

Here $c(t)$ is a function that only depends on time t . In Appendix 5.A it is shown that in this case the axial stress σ_{zz} is also uniform in this region.

For $a < r \leq b$ the solution in Eq. (5.3.7) satisfies $\sigma_{rr}(r;t=0) + \sigma_{\theta\theta}(r;t=0) = \text{constant}$. Using this result for each time t and by applying the appropriate boundary conditions,

$$\lim_{r \downarrow a} \sigma_{rr}(r;t) = \sigma_{rr}(a;t) \quad , \quad \sigma_{rr}(r=b;t) = 0 \quad , \quad (5.4.2)$$

the solution of the equation of equilibrium in $a < r \leq b$ is

$$\begin{aligned} \sigma_{rr}(r;t) &= \sigma_{rr}(a;t) \frac{(a/r)^2 - \delta^2}{1 - \delta^2} \\ \sigma_{\theta\theta}(r;t) &= -\sigma_{rr}(a;t) \frac{(a/r)^2 + \delta^2}{1 - \delta^2} \quad . \end{aligned} \quad (5.4.3)$$

As a result of Eq. (5.4.3), σ_{zz} is also uniform for $a < r \leq b$ (see appendix 5.A). Since the axial force resultant F_z should vanish in the absence of external forces and by making use of uniformity of the axial stresses in both regions, we find that

$$\sigma_{zz}(a < r \leq b; t) = -\sigma_{zz}(a; t) \frac{\delta^2}{1 - \delta^2} . \quad (5.4.4)$$

At this stage we have shown that inside the ion-track cylinder ($r \leq a$), all stresses $\sigma_{rr} = \sigma_{\theta\theta}$, and σ_{zz} are uniform (and therefore also all strains) and that in the surrounding elastic material ($a < r \leq b$) σ_{zz} is uniform, while σ_{rr} and $\sigma_{\theta\theta}$ have a radial $1/r^2$ dependence according to Eq. (5.4.3). Note that through Eqs. (5.4.3) and (5.4.4) all stresses in the material follow from the uniform stresses $\sigma_{rr}(a; t)$ and $\sigma_{zz}(a; t)$ inside the ion-track cylinder. To calculate the time evolution of these stresses we use the constitutive equations (5.2.2) to (5.2.7) and the following two continuity conditions at $r=a$:

1. Since the radial displacement $u_r(r; t)$ must be continuous at $r=a$ it follows from Eq. (5.3.3) that the hoop strain $\varepsilon_{\theta\theta}(r; t)$ should also be continuous at $r=a$:

$$\lim_{r \uparrow a} \varepsilon_{\theta\theta}(r; t) = \lim_{r \downarrow a} \varepsilon_{\theta\theta}(r; t) . \quad (5.4.5)$$

2. Due to the condition of generalized plane strain (i.e., $\varepsilon_{zz}(r; t) = \varepsilon_{zz}(t)$, independent of r):

$$\lim_{r \uparrow a} \varepsilon_{zz}(r; t) = \lim_{r \downarrow a} \varepsilon_{zz}(r; t) . \quad (5.4.6)$$

For $r \leq a$ it follows from Eq. (5.4.1) that $s_{rr} = s_{\theta\theta} = -(\frac{1}{2})s_{zz} = (\sigma_{rr} - \sigma_{zz})/3$, so that from Eq. (5.2.5) the viscous strain rates are uniform, given by

$$\dot{\varepsilon}_{rr}^v(t) = \dot{\varepsilon}_{\theta\theta}^v(t) = -\frac{1}{2} \dot{\varepsilon}_{zz}^v(t) = \frac{1}{6\eta} [\sigma_{rr}(t) - \sigma_{zz}(t)] . \quad (5.4.7)$$

Since $\varepsilon_{ij}^v(t=0) \equiv 0$ it follows from Eq. (5.4.7) that $\varepsilon_{rr}^v(t) = \varepsilon_{\theta\theta}^v(t) = -(\frac{1}{2})\varepsilon_{zz}^v(t)$ and therefore the total uniform strains $[\varepsilon_{ij}(r; t) = \varepsilon_{ij}(t)]$ in Eqs. (5.2.2)-(5.2.7) become

$$\begin{aligned} \varepsilon_{rr}(t) = \varepsilon_{\theta\theta}(t) &= \frac{1}{E} [(1 - \nu)\sigma_{rr}(t) - \nu\sigma_{zz}(t)] + \varepsilon_{rr}^v(t) + \alpha\Delta T(t) \\ \varepsilon_{zz}(t) &= \frac{1}{E} [\sigma_{zz}(t) - 2\nu\sigma_{rr}(t)] - 2\varepsilon_{rr}^v(t) + \alpha\Delta T(t) \end{aligned} . \quad (5.4.8)$$

For $a < r \leq b$, the strain in the elastic surrounding medium is given by Eq. (5.2.4). Taking the limit for $r \rightarrow a$ and by using Eqs. (5.4.2) and (5.4.3) we find that

$$\begin{aligned}
\lim_{r \downarrow a} \varepsilon_{rr}(r;t) &= \frac{1}{E} \left[\left(1 + \nu \frac{1 + \delta^2}{1 - \delta^2} \right) \sigma_{rr}(t) + \nu \frac{\delta^2}{1 - \delta^2} \sigma_{zz}(t) \right] \\
\lim_{r \downarrow a} \varepsilon_{\theta\theta}(r;t) &= \frac{1}{E} \left[- \left(\nu + \frac{1 + \delta^2}{1 - \delta^2} \right) \sigma_{rr}(t) + \nu \frac{\delta^2}{1 - \delta^2} \sigma_{zz}(t) \right] , \\
\lim_{r \downarrow a} \varepsilon_{zz}(r;t) &= \frac{1}{E} \left[- \frac{\delta^2}{1 - \delta^2} \sigma_{zz}(t) + 2\nu \frac{\delta^2}{1 - \delta^2} \sigma_{rr}(t) \right]
\end{aligned} \tag{5.4.9}$$

where the stresses $\sigma_{rr}(t)$ and $\sigma_{zz}(t)$ are the uniform stresses $\sigma_{rr}(a;t)$ and $\sigma_{zz}(a;t)$ in the ion-track cylinder. Inserting Eqs. (5.4.8) and (5.4.9) into the continuity conditions (5.4.5) and (5.4.6) results in two equations for $\sigma_{rr}(t)$, $\sigma_{zz}(t)$ and $\varepsilon_{rr}^v(t)$. If we then take the time derivative and use Eq. (5.4.7) to eliminate the viscous strain rates, two differential equations can be obtained for the radial and axial stresses inside the ion track:

$$\begin{aligned}
2 \dot{\sigma}_{rr}(t) - \nu \dot{\sigma}_{zz}(t) + \frac{\xi E}{6\eta(t)} [\sigma_{rr}(t) - \sigma_{zz}(t)] + \alpha \xi E \Delta \dot{T}(t) &= 0 \\
\dot{\sigma}_{zz}(t) - 2\nu \dot{\sigma}_{rr}(t) - \frac{\xi E}{3\eta(t)} [\sigma_{rr}(t) - \sigma_{zz}(t)] + \alpha \xi E \Delta \dot{T}(t) &= 0
\end{aligned} \tag{5.4.10}$$

with initial condition, from Eq. (5.3.6),

$$\sigma_{rr}(t=0) = \frac{1}{2} \sigma_{zz}(t=0) = - \frac{\alpha \xi E \Delta T_0}{2(1-\nu)} ,$$

with $\xi=1-\delta^2$ and $\eta(t) \equiv \eta(T(t))$. Addition of the two equations in a proper way gives a relation between the stress rates. By integrating over time we obtain the following relation between $\sigma_{rr}(t)$ and $\sigma_{zz}(t)$:

$$\sigma_{zz}(t) = - \frac{4-2\nu}{1-2\nu} \sigma_{rr}(t) - \frac{3\alpha \xi E}{1-2\nu} \Delta T(t) . \tag{5.4.11}$$

With the aid of Eq. (5.4.11), the set of first order differential equations (5.4.10) can be reduced to a single second-order differential equation for the radial viscous strain $\varepsilon_{rr}^v(t)$, through Eq. (5.4.7):

$$\begin{aligned}
\ddot{\varepsilon}_{rr}^v(t) + \frac{\dot{\tau}(t)+1}{\tau(t)} \dot{\varepsilon}_{rr}^v(t) - \frac{1+\nu}{5-4\nu} \frac{\alpha \Delta \dot{T}(t)}{\tau(t)} &= 0 \\
\varepsilon_{rr}^v(0) = 0 \quad , \quad \dot{\varepsilon}_{rr}^v(0) &= \frac{\alpha \xi E \Delta T_0}{12\eta_0(1-\nu)}
\end{aligned} \tag{5.4.12}$$

where

$$\tau(t) = \frac{12(1-\nu^2)}{5-4\nu} \frac{\eta(t)}{\xi E} \quad (5.4.13)$$

is the characteristic viscous flow time scale at time t , and $\eta_0 = \eta(t=0) = \eta(T(t=0)) = \eta(T_{max})$, is the spike's thermal viscosity at $t=0$. If $T(t)$ and $\eta(T(t))$ are known, the solution of Eq. (5.4.12) gives a full description of the viscous strains in ion tracks in a virgin sample without external stresses. By integrating Eq. (5.4.12) twice with respect to time we find the following closed-form integral solution for $\varepsilon_{rr}^v(t)$:

$$\varepsilon_{rr}^v(t) = \frac{1+\nu}{5-4\nu} \alpha \int_0^t \Delta T(t'') \exp \left[- \int_{t''}^t \frac{dt'}{\tau(t')} \right] \frac{dt''}{\tau(t'')} \quad (5.4.14)$$

This expression allows us to directly calculate the evolution of the viscous strains in both the high-temperature and the (rapid) cooling phase of the ion track cylinder. In the next section we will show how viscous strains are generated at spike temperatures $T > T^*$ and how these strains are frozen in upon subsequent cooling down.

5.5 Viscous flow in single ion tracks: results

Calculations of flow in an ion cylinder can be performed by numerically solving the differential equations (5.4.10) for σ_{rr} and σ_{zz} and (5.4.12) for ε_{rr}^v [or alternatively, evaluating Eq. (5.4.14)]. Normalization of these equations allows us to perform general calculations without using specific material dependent parameters. To this end we have normalized the temperature T with respect to the maximum temperature T_{max} inside the ion track. We used a temperature dependent shear viscosity $\eta(T)$ of the following general form:

$$\eta(T) = \psi 10^{\frac{\lambda}{T}} \quad (5.5.1)$$

where ψ and λ are material dependent parameters. In normalizing the temperature with T_{max} in Eqs. (5.4.10), (5.4.12) and (5.4.14), with η from Eq. (5.5.1), we have used the following normalized parameters for our numerical calculations: $T_s/T_{max}=0.025$ and $\lambda/T_{max}=6.8$.²⁶ Finally, the stresses σ_{ij} were normalized with $\alpha E \Delta T_0$, and the time t was normalized with τ_0 , given by

$$\tau_0 = \frac{12(1-\nu^2)}{5-4\nu} \frac{\eta_0}{E} \quad (5.5.2)$$

where Poisson's ratio ν was chosen to be 0.2, a typical value for silica glass.

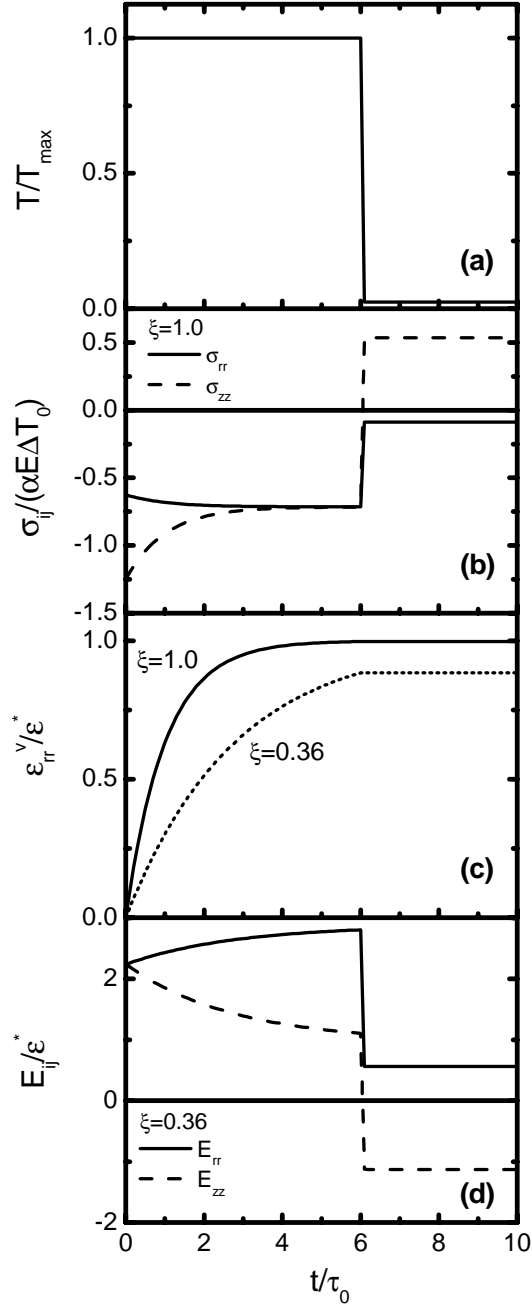


Figure 5.3 (a) Time evolution of the ion track temperature T , (b) the corresponding stresses σ_{ij} [$\sigma_{rr}=\sigma_{\theta\theta}$ (solid line), σ_{zz} (dashed line)] for $r \leq a$, (c) the associated radial viscous strain ϵ_{rr}^v [for $\xi=1.0$ (solid line), $\xi=0.36$ (dotted line)] for $r \leq a$, and (d) the resulting macroscopic deformations E_{rr} (solid line) and E_{zz} (dashed line) for $\xi=0.36$. The time is normalized with τ_0 [Eq. (5.5.2)]. Results are plotted using: $\nu=0.2$, $T_s/T_{max}=0.025$ and $\lambda/T_{max}=6.8$. Stresses are normalized with $\alpha E \Delta T_0$ and the strains in (c) and (d) with ϵ^* [Eq. (5.5.6)]. At the spike lifetime $\tau_s=6\tau_0$ the temperature almost instantaneously drops from T_{max} to the substrate temperature T_s .

First we will evaluate a limiting case in which the temperature $T(t)$ inside the ion track remains at a high temperature T_{max} during a time interval τ_s (spike lifetime) and then (almost) instantaneously drops to the substrate temperature T_s . This temperature evolution is shown in Fig. 5.3(a), where the (normalized) ion track temperature T/T_{max} is plotted as a function of t/τ_0 . In this calculation the spike lifetime τ_s has been chosen to be $6\tau_0$ to allow for nearly full relaxation of the stresses to their steady-state value. Since the temperature remains constant for $t \leq \tau_s$ the differential equations (5.4.10) and (5.4.12) can easily be solved analytically since $d\tau(t)/dt=0$ and $d\Delta T(t)/dt=0$. In this case the evolution of the radial stress is given by

$$\sigma_{rr}(t) = \frac{1-2\nu}{2(1-\nu)(5-4\nu)} \alpha \xi E \Delta T_0 \exp\left[-\xi \frac{t}{\tau_0}\right] - \frac{3}{5-4\nu} \alpha \xi E \Delta T_0, \quad (5.5.3)$$

which reveals that the characteristic relaxation time scale is $\tau_0/\xi = \tau_0/[1-(a/b)^2]$. The axial stress $\sigma_{zz}(t)$ can then be found from Eq. (5.4.11).

Figure 5.3(b) shows the result of the numerical calculation of the normalized radial stress $\sigma_{rr}(t)$ (solid curve) and axial stress $\sigma_{zz}(t)$ (dashed curve), as a function of t/τ_0 , for the case $\xi=1.0$, i.e. $b \gg a$. The initial values of σ_{rr} and σ_{zz} are compressive, as given by Eq. (5.3.6) (normalized values of -0.625 and -1.25, respectively). During viscous flow, for $0 \leq (t/\tau_0) \leq (\tau_s/\tau_0)=6$, the compressive radial stress increases, whereas the compressive axial stress decreases, thereby reducing the deviatoric stresses. As can be seen in Fig. 5.3(b), this process continues until all stresses are equal ($\sigma_{rr}=\sigma_{\theta\theta}=\sigma_{zz}$) and a negative hydrostatic stress state is achieved. From equations (5.5.3) and (5.4.11) it immediately follows that for $\tau_0 \ll t < \tau_s$ this stress is given by

$$\sigma_{rr} = \sigma_{\theta\theta} = \sigma_{zz} = -p = -\frac{3}{5-4\nu} \alpha \xi E \Delta T_0, \quad (5.5.4)$$

where p is the hydrostatic pressure inside the ion track after stress relaxation. From Eq. (5.5.4) it follows that the hydrostatic stress state has a pressure of $p/(\alpha E \Delta T_0) = 3\xi/(5-4\nu) = 0.714$, as can also be seen in Fig. 5.3(b).

For $0 \leq t \leq \tau_s$ the viscous strains resulting from the stress relaxation can be found by solving Eq. (5.4.12) or by directly calculating Eq. (5.4.14), and are given by:

$$\varepsilon_{rr}^v(t) = \varepsilon_{\theta\theta}^v(t) = -\frac{1}{2} \varepsilon_{zz}^v(t) = \frac{1+\nu}{5-4\nu} \alpha \Delta T_0 \left(1 - \exp\left[-\xi \frac{t}{\tau_0}\right]\right). \quad (5.5.5)$$

Viscous strains thus build up at a characteristic time scale of τ_0/ξ and saturate at a limiting value of

$$\varepsilon_{rr}^v = \varepsilon_{\theta\theta}^v = -\frac{1}{2}\varepsilon_{zz}^v \equiv \varepsilon^* = \frac{1+\nu}{5-4\nu}\alpha\Delta T_0 . \quad (5.5.6)$$

This is shown in Fig. 5.3(c) where the in-plane viscous strain ε_{rr}^v , normalized by ε^* , is plotted as a function of t/τ_0 for $\xi=1$. Starting at $\varepsilon_{rr}^v=0$ at $t=0$, the in-plane viscous strain increases and exponentially approaches its saturation value of ε^* , which is reached at the end of the spike lifetime τ_s . Note that the result in Eq. (5.5.6), which follows from the time-dependent relaxation model as a limiting case, was also found by Trinkaus *et. al.* in his ‘effective flow temperature approach’.¹¹

Next, at $t/\tau_0=6$, the spike instantaneously cools down to the substrate temperature T_s [Fig. 5.3(a)]. The viscosity η thus changes from a small value (liquid) to a relatively large value (solid), abruptly turning off viscous flow. As a result, the viscous strains given by Eq. (5.5.6) freeze in. This can be seen in Fig. 5.3(c) where ε_{rr}^v does not change upon the instant temperature quenching. As in the case of instantaneous heating (Sect. 5.3) the instantaneous cooling down is a simple elastic problem. The stress field can be derived by using the same continuity conditions at $r=a$ (Sect. 5.4) and by taking the in-plane frozen-in viscous strain equal to ε^* . This yields the following final stress state:

$$\begin{aligned} \sigma_{rr} = \sigma_{\theta\theta} &= -\frac{1-2\nu}{2(1-\nu)(5-4\nu)}\alpha\xi E\Delta T_0 \\ \sigma_{zz} &= \frac{2-\nu}{(1-\nu)(5-4\nu)}\alpha\xi E\Delta T_0 \end{aligned} . \quad (5.5.7)$$

Figure 5.3(b) reveals that both stresses abruptly adapt to the instant temperature jump and reach values of $\sigma_{rr}/(\alpha E\Delta T_0) = -0.089$ and $\sigma_{zz}/(\alpha E\Delta T_0) = +0.54$. The compressive radial stress and tensile axial stress are a direct consequence of the frozen-in viscous strains. Since the ion track has viscously expanded perpendicular to the ion beam, the in-plane stress remains compressive (<0) whereas the axial stress becomes tensile (>0) due to the viscous axial contraction. Said differently, if the ion track would be cut out from its elastic surrounding medium, the only strains within the ion track cylinder would be the viscous strains given by Eq. (5.5.6). The cylinder would expand freely in the direction perpendicular to the ion track with strain ε^* and contract in the axial direction with strain $-2\varepsilon^*$ (to conserve volume). Forcing the cylinder back into the surrounding medium would imply that it had to be *compressed* in the in-plane direction (radial and hoop) and to be *pulled* on in the axial direction (tensile stress). Therefore, “an ion track penetrating a thin film acts like a tensioned string tight between the two surfaces of the film”.¹¹

Fig. 5.3(c) also shows the viscous strain as a function of t/τ_0 for $\xi=0.36$ (dotted curve), *i.e.* a case where the sample’s edge at $r=b$ is located close to the ion track cylinder wall ($b=1.25a$). It can be seen that the characteristic time for

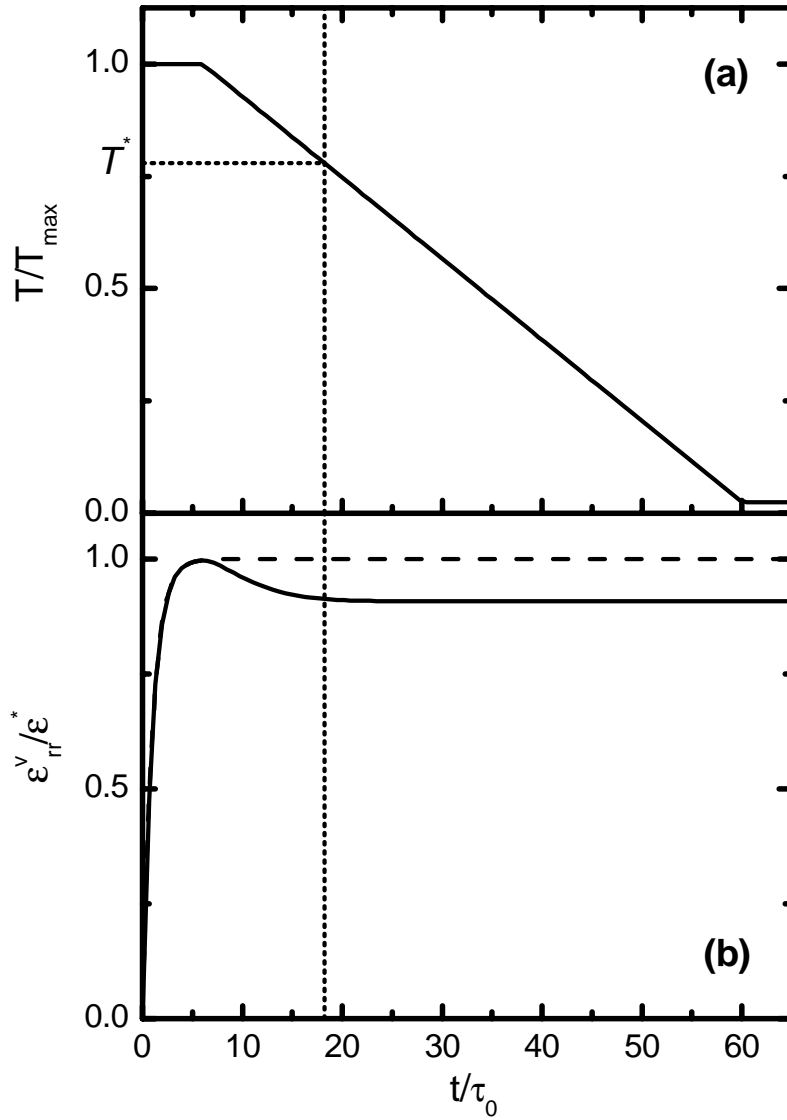


Figure 5.4 (a) Time evolution of the ion track temperature T , and (b) the corresponding radial viscous strain ϵ_{rr}^v (solid line) for $r \leq a$. The time is normalized with τ_0 , the characteristic time for shear stress relaxation in ion track cylinders at temperature T_{max} situated far away from the sample's edge [Eq. (5.5.2)]. Results are plotted using: $\nu=0.2$, $T_s/T_{max}=0.025$, $\lambda/T_{max}=6.8$ and $\xi=1$. The viscous strain is normalized with ϵ^* [Eq. (5.5.6)]. The dashed curve in (b) represents the radial viscous strain upon instantaneous freezing in [solid line in Fig. 5.3(c)]. Between $6\tau_0$ and $60\tau_0$ the temperature decreases from T_{max} to T_s at a constant rate dT/dt . The dotted lines indicate the time and the effective flow temperature T^* at which the viscous strains freeze in.

shear stress relaxation, τ_0/ξ , is now longer. As a consequence, the fully relaxed hydrostatic stress state in the ion track cannot be achieved within the spike lifetime and the viscous strain is frozen-in before it has reached its maximum value of ε^* . Ion tracks very close to the edge of a sample therefore should exhibit reduced viscous flow.²⁷

The situation described above is a limiting case in which cooling occurs instantaneously. The effect of the cooling rate dT/dt on viscous flow in ion tracks can be studied by numerical integration of Eq. (5.4.12). As a first step towards incorporating the effect of a temperature-time profile in the calculations we study the case for an ion track cylinder that cools down at a constant rate. Figure 5.4(a) shows an example of the ion track temperature T as a function of t/τ_0 , where the temperature again remains constant at T_{max} for $t \leq 6\tau_0$, after which the ion track cylinder cools down at a constant rate and reaches T_s at $t=60\tau_0$. All parameters used for this calculation are equal to those used in Fig. 5.3, *i.e.* $T_s/T_{max}=0.025$, $\lambda/T_{max}=6.8$, $\nu=0.2$ and $\xi=1.0$. The solid line in Fig. 5.4(b) shows the calculated normalized in-plane viscous strain $\varepsilon_{rr}^v/\varepsilon^*$ as function of t/τ_0 . For comparison, the dashed line in Fig. 5.4(b) shows $\varepsilon_{rr}^v/\varepsilon^*$ for infinitely large cooling rates and is identical to the solid line in Fig. 5.3(c). For $6\tau_0 \leq t \leq 60\tau_0$ the temperature in the spike decreases, which again introduces deviatoric stresses in the ion track. Since $\sigma_{rr}-\sigma_{zz}$ becomes negative, the in-plane viscous strain rate, $d\varepsilon_{rr}^v/dt$, is now negative according to Eq. (5.4.7). Therefore, the material will exhibit viscous flow in the opposite direction (with respect to the flow for $t \leq 6\tau_0$) in order to relax these deviatoric stresses, shown by the initial decrease in the solid curve of Fig. 5.4(b). As the temperature continues to decrease, the viscosity increases until it becomes too large for reverse viscous flow to continue on the time scale of the thermal spike. Hence, the in-plane viscous strain freezes in at a value smaller than ε^* , depending on the cooling rate dT/dt and the temperature dependence of the viscosity, $\eta(T)$. In this particular example, the effective frozen-in viscous strain is $0.91\varepsilon^*$ (solid line), 9 % lower than the value for infinitely large cooling rates (dashed line). From Fig. 5.4 we can estimate the effective flow temperature T^* , below which no stress relaxation occurs at the time scale of the thermal spike; it amounts to $\sim 0.8T_{max}$ in this example (dashed lines).

To estimate the value of T^* for a commonly irradiated material like silica glass, a material that exhibits large anisotropic plastic deformation under ion irradiation,^{4,7} the characteristic time scale τ for viscous flow in ion tracks, Eq. (5.4.13), can be set equal to the characteristic thermal spike lifetime τ_s .¹⁴ For SiO₂ containing 0.12 wt.% water, the viscosity (in Pa·s) below about 1800 K is specified as²⁸

$${}^{10}\log \eta = -7.7 + \frac{2.67 \times 10^4}{T}, \quad (5.5.8)$$

with the temperature T in K. If we extrapolate Eq. (5.5.8) for temperatures higher than 1800 K and use typical elastic parameters for silica, $\nu=0.2$ and $\mu=34$ GPa ($E=81.6$ GPa),²⁹ an estimated value of $T^* \sim 3250$ K is obtained when using a typical thermal spike lifetime of 10^{-10} s. This implies that for irradiation conditions in which the thermal spike temperature does not reach ~ 3250 K, no anisotropic deformation is expected.

In the preceding sections, we have derived an exact model to solve the anisotropic strain in a *single* ion track cylinder, assuming a homogeneous temperature distribution in the spike for a spike duration τ_s , and a subsequent temperature quenching profile. Experimental data on anisotropic deformation are only available on systems that have had *multiple* ion impacts. For example, the well-characterized deformation of spherical colloidal particles with diameters of ~ 1 μm , is the overall effect of some 10^6 - 10^7 ions impacting on a single colloid.⁶ In the next section we will describe how such a macroscopic effect can be derived from the mesoscopic model introduced above.

5.6 From mesoscopic model to macroscopic deformation

To show that the local viscous flow in single ion tracks is the origin of the macroscopic deformation process, we have to determine the change in the macroscopic sample dimensions due to successive ion impacts.

Our sample is a disk of radius b and height h , as sketched in Fig. 5.1. During a *single* ion-induced thermal spike having an internal radial viscous strain of $\varepsilon_{rr}^v(t)$, the radius of the sample changes with $\Delta b(t)$ and its height with $\Delta h(t)$. From Eq. (5.3.3) it follows that $\Delta b(t)=u_r(b;t)=b\varepsilon_{\theta\theta}(b;t)$, so that the macroscopic radial strain $E_{rr}(t)$ can be written as

$$E_{rr}(t) \equiv \frac{\Delta b(t)}{b} = \varepsilon_{\theta\theta}(b;t) \quad . \quad (5.6.1)$$

The macroscopic axial strain $E_{zz}(t)$ in the direction of the ion beam during a single ion-impact can be found in a similar manner and reads

$$E_{zz}(t) \equiv \frac{\Delta h(t)}{h} = \varepsilon_{zz}(t) \quad . \quad (5.6.2)$$

We can therefore directly calculate the macroscopic strains E_{rr} and E_{zz} resulting from a single ion impact using the mesoscopic model described in the previous sections. For the calculated example shown in Fig. 5.3(c) with $b=1.25a$ ($\delta=0.8$ or $\xi=0.36$, dotted line) the result is shown in Fig. 5.3(d), where E_{rr} (solid line) and E_{zz} (dashed line) are plotted as a function of t/τ_0 . This plot is obtained by numerically solving $\sigma_{rr}(t)$ and $\sigma_{zz}(t)$ from Eq. (5.4.10), substituting the solutions

into Eqs. (5.4.3) and (5.4.4), and finally by using $\varepsilon_{\theta\theta}$ and ε_{zz} from Eq. (5.2.4) at $r=b$.

Figure 5.3(d) shows that just after the abrupt temperature increase at $t=0$ the macroscopic strains (for a single ion impact) are equal and given by

$$E_{rr}(t=0) = E_{zz}(t=0) \equiv \alpha \Delta T_0 \delta^2 \quad , \quad (5.6.3)$$

which follows directly from Eq. (5.3.7). Next, for $0 \leq t \leq \tau_s$, E_{rr} increases during deviatoric stress relaxation resulting from the in-plane viscous expansion ($\varepsilon_{rr}^v(t) > 0$), whereas E_{zz} decreases due to the axial viscous contraction ($\varepsilon_{zz}^v(t) = -2\varepsilon_{rr}^v(t) < 0$). Finally, at $t = \tau_s$, the viscous strains freeze in during instantaneous temperature quenching, resulting in a net macroscopic expansion perpendicular to the ion beam, $E_{rr} > 0$, and a net contraction parallel to the ion beam, $E_{zz} = -2E_{rr} < 0$.

In case the ion track cylinder has a frozen-in radial viscous strain of ε^* ,³⁰ the frozen-in macroscopic strains in Eqs. (5.6.1) and (5.6.2) after a single ion impact can be directly calculated using Eqs. (5.5.7), (5.4.3), (5.4.4) and (5.2.4), resulting in

$$E_{rr} = -\frac{1}{2} E_{zz} \equiv \varepsilon^* \delta^2 \quad . \quad (5.6.4)$$

Eq. (5.6.4) clearly shows that the macroscopic deformation is volume conserving.

After N *independent* ion impacts³¹ distributed *randomly*³² over the sample surface, the total macroscopic deformation is simply a superposition of the individual ‘total’ strains. Recognizing that $N = \pi b^2 \phi$, where ϕ is the ion fluence, we can rewrite the macroscopic deformation as

$$E_{rr} = \pi a^2 \varepsilon^* \phi = -\frac{1}{2} E_{zz} \quad . \quad (5.6.5)$$

Eq. (5.6.5) immediately demonstrates that in the present model the viscous flow in single ion tracks is the origin of the macroscopic deformation process. We point out that our derivation of the macroscopic deformations directly from the single-ion results is notably different from the averaging procedure adopted by Trinkaus *et al.*, albeit yielding the same result.¹⁴

The rate of macroscopic deformation, A , defined as the differential length change perpendicular to the ion beam per unit ion fluence, is given by

$$A \equiv \frac{\partial E_{rr}}{\partial \phi} = \varepsilon^* \pi a^2 \quad , \quad (5.6.6)$$

according to Eq. (5.6.5). The value of A can be computed once the radius of the ion track is known. For an estimate, let us assume that the initial temperature

distribution has the form of a delta function along a linear ion track. Then the track temperature at a distance r from the ion track at time t can be found by solving the classical heat conduction law and is given by³³

$$T(r;t) = \frac{\Omega}{t} \exp\left[-\Lambda \frac{r^2}{t}\right] + T_s \quad , \quad (5.6.7)$$

with $\Omega = F_e / (4\pi\kappa)$ and $\Lambda = \rho C / (4\kappa)$. Here ρ is the mass density of the material, κ is the thermal conductivity, C is the specific heat capacity, and T_s is the substrate temperature. It is shown in Appendix 5.B that for this Gaussian temperature distribution the following relation can be found between the spike's cross section πa^2 and the flow temperature T^* :

$$\pi a^2 = \frac{\pi\Omega}{e\Lambda\Delta T^*} = \frac{F_e}{e\rho C\Delta T^*} \quad , \quad (5.6.8)$$

where $e = \exp(1)$ and $\Delta T^* = T^* - T_s$. When the (time-dependent) temperature distribution inside the track is uniform, the uniform in-plane viscous strain ε_{rr}^v at the end of a thermal spike is equal to ε^* [see Eq. (5.5.6)] for large track cooling rates. In the case of large cooling rates but a non-uniform temperature distribution, we may replace Eq. (5.5.6) by an appropriate average

$$\varepsilon_{rr}^v = \frac{1+\nu}{5-4\nu} \alpha \langle \Delta T \rangle \quad , \quad (5.6.9)$$

where $\langle \Delta T \rangle$ is the space and time-averaged temperature increase in the thermal spike. In Appendix 5.B it is shown that, for a Gaussian temperature distribution, $\langle \Delta T \rangle$ is given by³⁴

$$\langle \Delta T \rangle = 1.26 (T^* - T_s) \quad . \quad (5.6.10)$$

Replacing ε^* in Eq. (5.6.6) by ε_{rr}^v from Eq. (5.6.9) and by substituting Eqs. (5.6.8) and (5.6.10), the steady state deformation rate A now reads

$$A \equiv \frac{1.26}{e} \frac{1+\nu}{5-4\nu} \frac{\alpha F_e}{\rho C} \quad . \quad (5.6.11)$$

5.7 Discussion: comparison with experiment

a) A at very high energy and low substrate temperature

Klaumünzer *et al.* studied the expansion of silica foils under 360 MeV Xe ion irradiation at 100 K and determined $A=(8.0\pm 0.5)\times 10^{-16}$ cm²/ion.³⁵ Eq. (5.6.11) with the corresponding stopping of $F_e=15.1$ keV/nm and typical material parameters of $\nu=0.2$, $\alpha=0.6\times 10^{-6}$ K⁻¹, $\rho=2.2\times 10^3$ kg·m⁻³ and $C=10^3$ Jkg⁻¹K⁻¹ yields $A=8.7\times 10^{-16}$ cm²/ion, which is in close agreement with the experimental result.

b) Energy dependence of A

As was shown in Chapter 4 significant anisotropic deformation is observed at energies as low as 300 keV,⁷ and a linear increase of A with F_e is experimentally observed. This is in direct agreement with Eq. (5.6.11). The increase of A with F_e is brought about by the increasing cylindrical track radius a [see Eqs. (5.6.6) and (5.6.8)].

c) Threshold F_e for anisotropic deformation

It has been experimentally observed for some silica as well as metallic glasses that no deformation occurs below a threshold electronic stopping, typically around 2 keV/nm.^{4,35} This is in contrast to what we found in Chapter 4 for colloidal silica, where no threshold is observed.⁷ One explanation for this difference may be the relatively low value of the flow temperature T^* for colloidal silica compared to that of other amorphous materials. Indeed, the bulk melting temperature of colloidal silica is several 100 K below that of fused silica.

d) Substrate temperature dependence of A

As was shown in Chapter 4, A decreases with irradiation substrate temperature by a factor 4.5 between 85 K and 380 K for colloidal silica particles,⁷ similar to what was found by Klaumünzer *et al.* for silica and metallic glasses.^{1,4} A decrease with temperature is in agreement with the viscoelastic model: the deviatoric stress resulting from the thermal spike [see Eqs. (5.2.6) and (5.5.7)] can be partly relaxed at elevated substrate temperatures. Additional calculations must be done to quantitatively study this effect.

Summarizing the comparison between experiment and theory above, we conclude that the viscoelastic model provides an excellent qualitative and often quantitative representation of experimental results.

5.8 Conclusions

We have performed a detailed investigation of a viscoelastic thermal spike model describing viscous flow in ion tracks as the origin of anisotropic deformation. First, the track geometry and the imposed condition of ‘generalized plane strain’ were discussed. After assigning Maxwell’s model as the physical relevant model, the governing equations describing the flow were discussed in detail. By dividing the analysis in a thermal loading and viscous relaxation part, we solved the equations yielding the time evolution of the stresses and (viscous) strains for a specific track temperature history $T(t)$. A closed-form expression for the radial viscous strains in ion tracks has been found.

We have shown that for large track cooling rates the viscous strains freeze in effectively, while for smaller cooling rates reverse flow reduces the net viscous strains in the ion track. The model also demonstrates that ion tracks close to the edge exhibit reduced viscous flow with respect to tracks located far away from the edge.

As a limiting case, for sufficiently large thermal spike lifetimes and instantaneous temperature quenching, the ‘effective flow temperature approach’ as introduced by Trinkaus *et al.* follows directly from the viscoelastic model. For SiO_2 the effective flow temperature T^* , at which the viscous strains effectively freeze in, is about 3250 K.

Next, we have shown that the frozen-in viscous strains of individual ion impacts are the origin of the macroscopic anisotropic deformation process. In particular, the macroscopic deformation rate can be calculated directly from the mesoscopic model by considering multiple, independent ion tracks randomly penetrating the sample.

Based on a Gaussian temperature profile the macroscopic deformation rate has been calculated. For vitreous silica irradiated with 360 MeV Xe ions at low irradiation temperatures the experimentally observed deformation rate by Klaumünzer *et al.* agrees well with the calculated value from the viscoelastic model. Finally, the experimental dependence of the deformation rate on electronic stopping F_e and irradiation substrate temperature T_s is discussed and shows qualitative agreement with the viscoelastic model.

Appendix 5.A

To show that the axial stress σ_{zz} is uniform for $r \leq a$, we write Hooke's law, Eq. (5.2.4) for isotropic elastic media, in the form

$$\sigma_{ij} = 2\mu\varepsilon_{ij}^e + \lambda\varepsilon_{kk}^e \delta_{ij} \quad , \quad (5.A.1)$$

where $\lambda = k - (2/3)\mu$ is Lamé's constant and $k = E/[3(1-2\nu)]$ the bulk modulus of elasticity. Using Eqs. (5.A.1), (5.2.2) and (5.2.7) we then obtain

$$\begin{aligned} \sigma_{rr} &= 2\mu(\varepsilon_{rr} - \varepsilon_{rr}^v) + \lambda\varepsilon_{kk} - 3k\alpha\Delta T \\ \sigma_{\theta\theta} &= 2\mu(\varepsilon_{\theta\theta} - \varepsilon_{\theta\theta}^v) + \lambda\varepsilon_{kk} - 3k\alpha\Delta T \quad , \\ \sigma_{zz} &= 2\mu(\varepsilon_{zz} - \varepsilon_{zz}^v) + \lambda\varepsilon_{kk} - 3k\alpha\Delta T \end{aligned} \quad (5.A.2)$$

making use of the fact that viscous strains are volume preserving, i.e. $\varepsilon_{kk}^v = 0$. Since $\sigma_{rr} = \sigma_{\theta\theta}$ [Eq. (5.4.1)] and $\varepsilon_{rr}^v = \varepsilon_{\theta\theta}^v$ [Eq. (5.4.7)], it follows from Eq. (5.A.2) that $\varepsilon_{rr} = \varepsilon_{\theta\theta}$. From Eq. (5.3.3) it immediately follows that both ε_{rr} and $\varepsilon_{\theta\theta}$ are uniform as well. By taking the time derivative of axial stress in Eq. (5.A.2) and substituting Eq. (5.4.7) we can now write for $r \leq a$

$$\dot{\sigma}_{zz} + \frac{2\mu}{3\eta}\sigma_{zz} = 2\mu\dot{\varepsilon}_{zz} + \frac{2\mu}{3\eta}\sigma_{rr} + \lambda\left(2\dot{\varepsilon}_{rr} + \dot{\varepsilon}_{zz}\right) - 3k\alpha\Delta\dot{T} \quad . \quad (5.A.3)$$

All terms on the right-hand side of Eq. (5.A.3) are clearly uniform. Since $\sigma_{zz}(t=0)$ is uniform [Eq. (5.3.6)] it follows from Eq. (5.A.3) that σ_{zz} is uniform at each time t .

For the elastic surrounding medium, $a < r \leq b$, it follows from Eq. (5.A.2) with $\Delta T = 0$,

$$\begin{aligned} \sigma_{rr} &= 2\mu\varepsilon_{rr} + \lambda\varepsilon_{kk} \\ \sigma_{\theta\theta} &= 2\mu\varepsilon_{\theta\theta} + \lambda\varepsilon_{kk} \\ \sigma_{zz} &= 2\mu\varepsilon_{zz} + \lambda\varepsilon_{kk} \end{aligned} \quad (5.A.4)$$

that

$$\sigma_{rr} + \sigma_{\theta\theta} = 2(\mu + \lambda)(\varepsilon_{rr} + \varepsilon_{\theta\theta}) + 2\lambda\varepsilon_{zz} \quad . \quad (5.A.5)$$

According to Eq. (5.4.3) $\sigma_{rr} + \sigma_{\theta\theta}$ is uniform and from Eq. (5.A.5) it then follows that $\varepsilon_{rr} + \varepsilon_{\theta\theta}$ is uniform and therefore ε_{kk} as well. Thus, σ_{zz} is also uniform over $a < r \leq b$.

Appendix 5.B

For the Gaussian temperature profile given by Eq. (5.6.8) the maximum temperature at radial distance r is

$$T_{\max}(r) = \frac{\Omega}{e\Lambda r^2} + T_s, \quad (5.B.1)$$

occurring at $t = \Lambda r^2$. The radius $r=a$ is defined as the radius of the cylinder where the maximum temperature T_{\max} just reaches the flow temperature T^* at time $t=t^*$. Hence,

$$\pi a^2 = \frac{\pi\Omega}{e\Lambda\Delta T^*}, \quad (5.B.2)$$

with $\Delta T^* = T^* - T_s$.

Since viscous strains are generated at temperatures above the flow temperature T^* , the appropriate average track temperature increase $\langle\Delta T\rangle$ can be found by averaging the temperature difference $\Delta T(r;t)$ over space and time where $T \geq T^*$, starting at $t=t^*$: we therefore consider the region $r \leq R(t) \leq a$ with its boundary, specified by $T(R(t);t) = T^*$, moving towards the center. At time $t \geq t^* = \Lambda a^2 = \Omega/(e\Delta T^*)$ the radius $R(t)$ of the region for which $T \geq T^*$ is given by

$$R(t) = \sqrt{\frac{t}{\Lambda} \ln \left[\frac{\Omega}{\Delta T^* t} \right]} = a \sqrt{\frac{t}{t^*} \left(1 + \ln \left[\frac{t^*}{t} \right] \right)}. \quad (5.B.3)$$

Since $0 \leq R(t) \leq a$, the time interval for which the track temperatures exceed T^* therefore equals $t^* \leq t \leq et^*$. First we determine the spatial average at a fixed time t over the region $r \leq R(t)$:

$$\langle\Delta T\rangle(t) \equiv \frac{1}{\pi R^2(t)} \int_0^{R(t)} \Delta T(r;t) 2\pi r dr = \frac{e - t/t^*}{(t/t^*)(1 - \ln[t/t^*])} \Delta T^*. \quad (5.B.4)$$

Next, the average track temperature increase $\langle\Delta T\rangle$ can be found by averaging this mean value $\langle\Delta T\rangle(t)$ over the relevant time interval $t^* \leq t \leq et^*$, resulting in

$$\langle\Delta T\rangle \equiv \frac{1}{t^*(e-1)} \int_{t^*}^{et^*} \langle\Delta T\rangle(t) dt = \frac{\Delta T^*}{e-1} \int_1^e \frac{e-x}{x(1-\ln[x])} dx = 1.26\Delta T^*. \quad (5.B.5)$$

References

- ¹ S. Klaumünzer and G. Schumacher, Phys. Rev. Lett. **51**, 1987 (1983)
- ² S. Klaumünzer, Radiat. Eff. Defects Solids **110**, 79 (1989)
- ³ M.-d. Hou, S. Klaumünzer, and G. Schumacher, Phys. Rev. B **41**, 1144 (1990)
- ⁴ A. Benyagoub, S. Löffler, M. Rammensee, S. Klaumünzer, and G. Saemann-Ischenko, Nucl. Instrum. Methods Phys. Res. B **65**, 228 (1992)
- ⁵ A. Audouard, J. Dural, M. Toulemonde, A. Lovas, G. Szenes, and L. Thomé, Phys. Rev. B **54**, 15690 (1996)
- ⁶ E. Snoeks, A. van Blaaderen, T. van Dillen, C. M. van Kats, M.L. Brongersma, and A. Polman, Adv. Mater. **12**, 1511 (2000)
- ⁷ T. van Dillen, A. Polman, C. M. van Kats, and A. van Blaaderen, Appl. Phys. Lett. **83**, 4315 (2003)
- ⁸ T. van Dillen, A. Polman, W. Fukarek, and A. van Blaaderen, Appl. Phys. Lett **78**, 910 (2001)
- ⁹ E. Snoeks, A. van Blaaderen, T. van Dillen, C. M. van Kats, K. Velikov, M. L. Brongersma, and A. Polman, Nucl. Instrum. Methods Phys. Res. B **178**, 62 (2001)
- ¹⁰ K. P. Velikov, T. van Dillen, A. Polman, and A. van Blaaderen, Appl. Phys. Lett. **81** 838 (2002)
- ¹¹ H. Trinkaus and A. I. Ryazanov, Phys. Rev. Lett. **74**, 5072 (1995)
- ¹² H. Trinkaus, Nucl. Instrum. Methods Phys. Res. B **107**, 155 (1996)
- ¹³ A. Benyagoub, S. Klaumünzer, and M. Toulemonde, Nucl. Instrum. Methods Phys. Res. B **146**, 449 (1998)
- ¹⁴ H. Trinkaus, Nucl. Instrum. Methods Phys. Res. B **146**, 204 (1998)
- ¹⁵ J. F. Ziegler, J. P. Biersack, and U. Littmark, *The Stopping and Range of Ions in Solids* (Pergamon, New York, 1985)
- ¹⁶ Z. G. Wang, C. Dufour, E. Paumier, and M. Toulemonde, J. Phys. Condens. Matter **6**, 6733 (1994)
- ¹⁷ In this work we also assume that the electronic stopping F_e is fully converted to heat in the cylindrical thermal spike.
- ¹⁸ M. Toulemonde, Ch. Dufour, Z. Wang, and E. Paumier, Nucl. Instrum. Methods Phys. Res. B **112**, 26 (1996)
- ¹⁹ M. Toulemonde, J. M. Costantini, Ch. Dufour, A. Meftah, E. Paumier, and F. Studer, Nucl. Instrum. Methods Phys. Res. B **116**, 37 (1996)
- ²⁰ A. I. Ryazanov, A. E. Volkov, and S. Klaumünzer, Phys. Rev. B **51**, 12107 (1995)
- ²¹ V. A. Borodin, A. E. Volkov, and D. N. Korolev, Nucl. Instrum. Methods Phys. Res. B **209**, 122 (2003)
- ²² Generally, the elastic moduli depend on temperature. For example, Polian *et al.* have studied the elastic properties of liquid SiO₂ up to 2300 K by Brillouin spectroscopy measurements [A. Polian, Dung Vo-Thanh, and P. Richet, Europhys. Lett. **57**, 375 (2002)]. It was found that the shear modulus μ of liquid SiO₂ is 34 GPa at 2300 K, which is only 10 % larger than the value of 31 GPa found for solid

- SiO₂ at 293 K. Consequently, we assume the elastic moduli to be temperature-independent, so that the same moduli can be used in- and outside the ion track.
- ²³ In the cylindrical coordinate system used here (see Fig. 5.1), all shear stresses are zero due to symmetry (Sec. 5.3), while the deviatoric stresses are not. However, shear stresses do exist, albeit on coordinate axes that are rotated with respect to the cylindrical coordinate axes used here.
- ²⁴ A. C. Ugural and S. K. Fenster, *Advanced Strength and Applied Elasticity*, 3rd edition (Prentice-Hall PTR, New Jersey, 1995)
- ²⁵ To calculate the thermal strains for $a < r \leq b$ Eq. (5.3.2) can be used with $\Delta T = 0$.
- ²⁶ The quantity ψ cancels out in normalizing Eqs. (5.4.10), (5.4.12) and (5.4.14).
- ²⁷ Ion tracks close to the sample's edge of course do not exhibit the axial symmetry as in our calculations: the edge is not symmetrically located around the ion track. However, the frozen-in (in-plane) viscous strain, given by $\varepsilon^* (1 - \exp[-\xi \tau_s / \tau_0])$, still gives a lower limit estimate for the reduced viscous strains in ion tracks close to the edge.
- ²⁸ N. P. Bansal and R. H. Doremus, *Handbook of Glass Properties* (Academic Press, New York, 1986)
- ²⁹ A. Polian, Dung Vo-Thanh, and P. Richet, *Europhys. Lett.* **57**, 375 (2002)
- ³⁰ This is not the case for the example plotted in Fig. 5.3(d) as can be seen from the associated in-plane viscous strain plotted in Fig. 5.3(c) (dotted line).
- ³¹ Independent ion tracks are ion tracks that do not overlap and do not 'feel' each other's stress field.
- ³² This suggests that on average each ion can be viewed to have its impact at the center of the sample having a distance b to the edge (provided that b is not too close to a).
- ³³ G. H. Vineyard, *Radiat. Eff.* **29**, 245 (1976)
- ³⁴ The value of the average depends on how the average is taken. Our result is slightly different from the one found by Trinkaus *et al.*¹¹
- ³⁵ S. Klaumünzer, *Nucl. Tracks Radiat. Meas.* **19**, 91 (1991)

6 **Ion irradiation-induced anisotropic plastic deformation of silicon microstructures**

Amorphous silicon micropillars show anisotropic plastic shape changes upon irradiation with 30 MeV Cu ions. The transverse plastic strain rate is $(2.5 \pm 0.2) \times 10^{-17}$ cm²/ion at 77 K, which is about one order of magnitude less than that of silica glass. In contrast, crystalline silicon pillars, irradiated under the same conditions, do not exhibit anisotropic deformation. A viscoelastic and free volume model is used to qualitatively describe the data. By irradiating partially amorphous structures a variety of silicon microshapes can be fabricated.

6.1 Introduction

Amorphous materials such as metallic and silica glasses, subjected to high-energy ion irradiation, show irreversible anisotropic plastic flow at temperatures far below the glass transition temperature;¹⁻³ these materials expand in the direction perpendicular to the ion beam and shrink in the direction parallel to the ion beam, while their volume remains constant. The deformation strain increases with ion fluence at a constant rate that increases with ion energy and decreases with increasing substrate temperature.³ This beam-induced anisotropic deformation leads to a dramatic shape change of free-standing colloidal particles,⁴ as described in Chapters 2 and 3. In Chapter 4 we demonstrated that the deformation process occurs at ion energies as low as 300 keV.⁵

Ion irradiation-induced deformation of silicon has not been studied in detail, with one exception of hydrogenated amorphous Si (a-Si:H) foils that did show deformation under 360 MeV ion irradiation.⁶ As ion implantation of Si is a technologically important process, it is important to study deformation of this material. The deformation effect may then be exploited to tailor the shape of Si microstructures. In addition, by comparing ion irradiation effects in the crystalline and amorphous phases of Si, insights in the mechanism behind the deformation process may be acquired.

In this chapter we investigate the irradiation of 1.5 μm tall Si micropillars with 30 MeV Cu ions. We find that pre-amorphized pillars show anisotropic plastic deformation under irradiation, while crystalline pillars do not. We determine the deformation rate constant, compare our data with a viscoelastic and free volume model for deformation, and demonstrate the formation of unique microstructures in amorphous/crystalline composite structures.

6.2 Experimental

Crystalline Si(100) pillars of 1.5 μm height were made by anisotropic reactive ion etching of a silicon-on-insulator substrate (1.5 μm Si/3.0 μm SiO₂/Si) in a SF₆/O₂ plasma using a method described in Ref. 7. By careful tuning of the etching parameters near-vertical sidewalls were achieved.

Some pillars were turned amorphous using 3 MeV Xe irradiation at fluences up to $1.0 \times 10^{15} \text{ cm}^{-2}$, while cooling the substrate holder with liquid nitrogen. These irradiations were performed with the ion beam tilted 7° away from the normal to avoid ion channeling. The thickness of the amorphous layer was determined by channeling Rutherford backscattering spectrometry on a planar Si(100) sample irradiated under the same conditions, and was at least 1.5 μm . Electron backscatter diffraction patterns of the pillars during SEM

confirmed that the pillars were amorphous. Partial amorphization of the Si pillars was achieved after irradiation with 1 MeV Xe ions to a fluence of $2.1 \times 10^{15} \text{ cm}^{-2}$ at 77 K.

Substrates containing both c-Si and a-Si pillars were clamped to a liquid-nitrogen cooled copper block and then irradiated with 30 MeV Cu ions to fluences in the range $(1.8\text{-}8.2) \times 10^{15} \text{ cm}^{-2}$ using tandem accelerators in Rossendorf and Utrecht. The irradiations were performed at normal incidence or with the ion beam tilted 4° away from the normal to avoid channeling in the c-Si pillars.

Before and after the ion irradiations the size and shape of the Si micropillars were investigated by scanning electron microscopy (SEM) using a 5, 10 or 20 keV electron beam.

6.3 Results and discussion

Figure 6.1(a) shows a side-view SEM image (2° tilt) of Si pillars with a width of $1.8 \mu\text{m}$. The pyramidal footprint in the contact region with the silica substrate layer is characteristic for the etching process and is caused by the reduced etch rate of Si in the (111) directions.⁷

Figure 6.1(b) shows a side-view SEM image (10° tilt) of amorphized silicon pillars. The dashed box in Fig 6.1(b) outlines the outer boundaries of a pillar and is identical to that for the crystalline pillars in Fig. 6.1(a). Thus, no measurable deformation is observed after amorphization using 3 MeV Xe. Since ion beam-amorphized Si (a-Si) has a density that is 1.8 % lower than that of crystalline Si (c-Si),⁸ the pillars must have homogeneously expanded by about 0.6 %. This expansion is too small to be observed in SEM.

Figure 6.1(c) shows a SEM image of c-Si pillars after irradiation with 30 MeV Cu ions to a fluence of $1.8 \times 10^{15} \text{ cm}^{-2}$ at an ion beam energy flux of 0.7 W/cm^2 . No anisotropic deformation of the c-Si pillars is observed. Amorphous Si pillars [from Fig. 6.1(b)] irradiated under the same conditions are shown in the SEM image of Fig. 6.1(d). It can clearly be seen that the a-Si pillars have expanded perpendicular to the ion beam and contracted parallel to the ion beam direction, retaining the rectangular cross sectional shape. The relative lateral expansion is $12.2 \pm 2.0 \%$. From measurements of the transverse and longitudinal dimensions it follows that (within $\pm 3\%$) the a-Si pillar's volume has remained constant after deformation.

By comparing the data in Figs. 6.1(c) and (d) we thus conclude that there is a clear difference in ion beam-induced effects in c-Si and a-Si. Ion irradiation-induced anisotropic deformation is a universal phenomenon in amorphous materials.⁹ As shown in the previous chapter, the driving force for this effect is the electronic stopping F_e , the energy loss of the ions into electronic excitations and ionization of target atoms.¹⁰ The deformation effects in silica and metallic

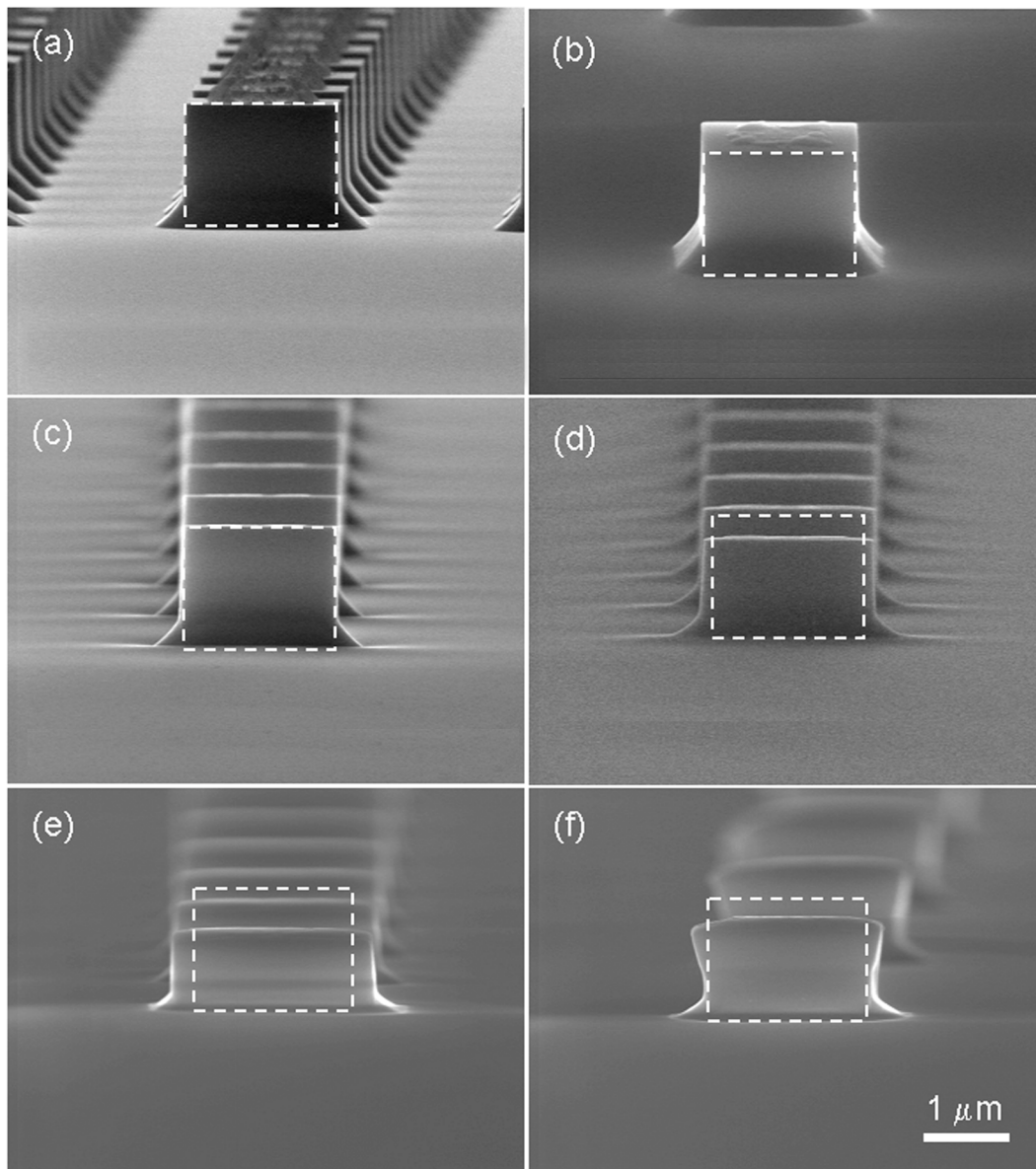


Figure 6.1 Scanning electron microscopy images of (a) unirradiated c-Si(100) pillars, (b) Si pillars amorphized with 3 MeV Xe, $1.0 \times 10^{15} \text{ cm}^{-2}$, (c) c-Si pillars irradiated with 30 MeV Cu, $1.8 \times 10^{15} \text{ cm}^{-2}$, (d) a-Si pillars irradiated with 30 MeV Cu, $1.8 \times 10^{15} \text{ cm}^{-2}$, (e) a-Si pillars irradiated with 30 MeV Cu, $8.2 \times 10^{15} \text{ cm}^{-2}$, and (f) partially amorphized Si pillars, subsequently irradiated with 30 MeV Cu, $6.1 \times 10^{15} \text{ cm}^{-2}$. SEM images were taken with a side-view tilt angle of $2^\circ \pm 1^\circ$ (a,c-f) and $10^\circ \pm 1^\circ$ (b). Magnification is the same for all micrographs.

glasses can be well described by a viscoelastic model derived by Trinkaus *et al.*,¹¹ and the time-dependent extension that we presented in Chapter 5. In this model viscous flow in ion track cylinders is the origin of the macroscopic

anisotropic deformation. It is assumed that thermal expansion of a cylindrically shaped region around the ion track leads to the generation of shear stresses that subsequently relax due to local atomic rearrangements in (overlapping) shear sites, regions with a local free volume.⁹ The net effect of this shear stress relaxation is a local in-plane expansion perpendicular to the ion track, which freezes in upon cooling down of the thermal spike. Within this model, anisotropic deformation is not expected to occur in crystalline materials, due to the lack of shear sites.^{2,9} In those materials, epitaxial recrystallization at the track's solid-liquid interface would restore the initial state, without anisotropic deformation. Our data on c-Si and a-Si provide clear experimental support for this model.

Figure 6.2 shows the fluence dependence of the transverse strain of a-Si pillars after irradiation with 30 MeV Cu ions at fluences in the range $(2.0\text{--}8.2)\times 10^{15}\text{ cm}^{-2}$ at a beam energy flux of 1.5 W/cm^2 (solid squares). As can be seen the transverse plastic strain increases gradually with ion fluence. A SEM image of the sample irradiated to a fluence of $8.2\times 10^{15}\text{ cm}^{-2}$ is shown in Fig. 6.1(e); it shows a transverse plastic strain as high as $21.8 \pm 2.1\%$. Note that the rectangular shape of the pillar with its pyramidal footprint remains conserved

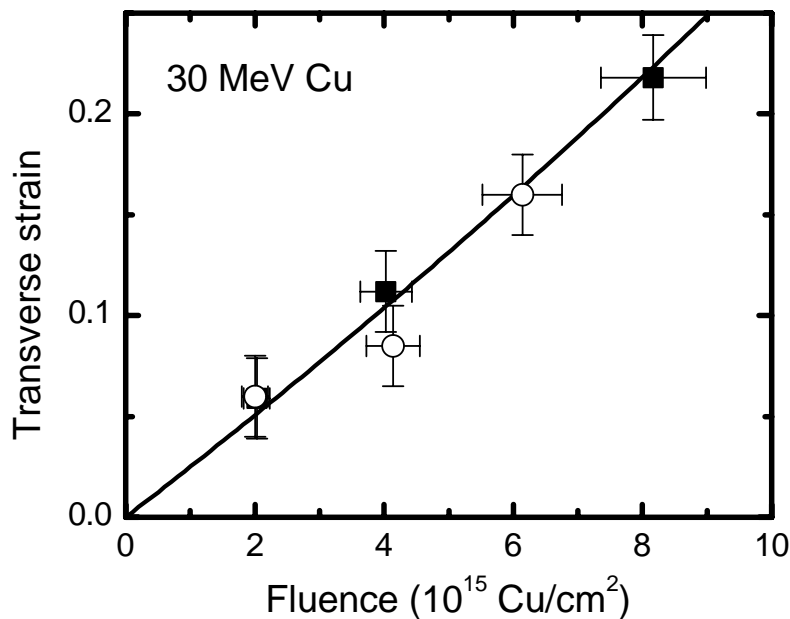


Figure 6.2 Transverse strain of ion beam-amorphized Si pillars during 30 MeV Cu irradiation at a beam energy flux of 1.5 W/cm^2 as a function of Cu ion fluence (ϕ). The sample holder was cooled with liquid nitrogen. The solid squares refer to the deformation of Si pillars amorphized with 3 MeV Xe [e.g. Fig. 6.1(e)], the open circles to deformation of Si pillars amorphized with 1 MeV Xe [e.g. Fig. 6.1(f)]. The solid curve is a fit to the data (solid squares) using the relation $\varepsilon_T = \exp(A\phi) - 1$ and results in $A = (2.5 \pm 0.2) \times 10^{-17}\text{ cm}^2/\text{ion}$.

upon continued irradiation, except for the expansion factor. This is attributed to the radiation-induced lowering of the viscosity of the underlying SiO₂ substrate (a known effect¹²) that enables Newtonian plastic flow around the interface of the expanding a-Si and the SiO₂ substrate. Assuming a constant deformation rate A , the transverse plastic strain should increase exponentially with ion fluence ϕ : $\varepsilon_T = \exp(A\phi) - 1$.³ The solid line in Fig. 6.2 is a fit of the transverse strain data (solid squares) to this relation. From the fit we find that $A = (2.5 \pm 0.2) \times 10^{-17}$ cm²/ion.

To further illustrate how we can obtain local control over the shape of silicon microstructures by ion irradiation we have irradiated Si pillars that were partially amorphized. This amorphization was done by irradiating 1.5 μm -tall c-Si pillars with 1 MeV Xe ions to a fluence of 2.1×10^{15} cm⁻² at 77 K, which resulted in a 710-nm thick amorphous top layer. SEM micrographs did not show deformation of the Si pillars due to the 1 MeV Xe irradiation. Next, these pillars were irradiated with 30 MeV Cu ions to fluences of 2.0×10^{15} , 4.1×10^{15} and 6.1×10^{15} cm⁻² at a beam energy flux of 1.6 W/cm², while cooling the substrate holder with liquid nitrogen. Figure 6.1(f) shows a SEM image of a partially amorphized pillar irradiated to a fluence of 6.1×10^{15} cm⁻². As can be clearly seen, the amorphous top part of the pillar has expanded whereas the bottom crystalline part has remained undeformed. Note that the expansion at the lower part of the amorphous region is constrained by the non-deforming c-Si underneath. The transverse strain measured at the top of the pillar is included in Fig. 6.2 for the three fluences used (open circles). These data fit well with the trend observed for the completely amorphous pillars.

At this stage we have clearly demonstrated that 30 MeV Cu irradiation of a-Si leads to anisotropic deformation with a well-defined rate constant. We can now compare the deformation of ion beam-amorphized Si with the well-known deformation of silica glass (SiO₂). Benyagoub *et al.* have studied the deformation of vitreous silica under high-energy ion irradiation.³ From interpolation of their data a strain rate constant of $A = 2.5 \times 10^{-16}$ cm²/ion is derived for silica at an electronic stopping equivalent to that in our experiment ($F_e = 6.0$ keV/nm). This is 10 times larger than the strain rate found for a-Si in this work (Fig. 6.2). In addition, the deformation of colloidal silica particles upon MeV ion irradiation was found to be at least 10 times larger than that of a-Si found here (Chapters 2-4).⁴ We can also compare the deformation of ion beam-amorphized Si with that of hydrogenated a-Si under 360 MeV Xe ion irradiation as studied by Klaumünzer *et al.*⁶ From that work a deformation strain rate of at least 5×10^{-16} cm²/ion can be estimated at $F_e = 6.0$ keV/nm, again much higher than the value found here for pure a-Si. Finally, Chicoine *et al.* have studied surface deformations during off-normal 24 MeV Se irradiation of several amorphous materials and found that lateral mass transport in pure a-Si was about 30 times smaller than in fused silica.¹³

In the viscoelastic model (Chapter 5) the deformation rate depends on the parameters that determine the effective diameter and the thermal expansion of the heated region around the ion track (i.e. F_e , specific heat, mass density, thermal expansion coefficient).¹¹ Using parameters for a-Si and silica, it is found that the calculated deformation rate of these two materials would be quite similar, contrary to what is observed. One possible explanation of the difference is that a-Si may not contain a high enough amount of free volume to mediate full shear stress relaxation. Indeed, the excess free volume in a-Si (relative to c-Si) is only 1.8 %, whereas this difference for amorphous SiO₂ and quartz amounts to ~17 %. A counter argument, however, to the amount of free volume being a limiting factor determining the deformation is the fact that metallic glasses, that are known to have small free volume,² do show large anisotropic deformation strain rates, similar to SiO₂.

One phenomenon that distinguishes silicon from most other materials is that its molten phase has a larger density (by 8 % at the melting point) than the solid. This would imply that the amorphous region around the ion track would initially expand as the temperature increases, but then contract as the ion track region becomes molten. This effect could cause a reduced deformation rate for a-Si compared to other amorphous materials such as SiO₂.

Finally, we note that not only thermally-induced viscous flow but also ion irradiation-induced defects may cause shear stress relaxation in the ion tracks (and thus deformation). Thus, the density of such defects, or the radiation-induced viscosity, is also a parameter that might determine the deformation rate. Values for the radiation-induced viscosity during ion irradiation have been measured for both a-Si¹⁴ and SiO₂,¹² and, under comparable conditions (2 MeV Xe), the viscosity of a-Si was found to be 5 to 10 times higher than that of SiO₂, implying that a-Si flows less than SiO₂.

A quantitative model of the deformation of a-Si must therefore necessarily include (at least) the effects of free volume, density change upon ion track melting and radiation-induced flow, and remains thus quite a challenge to establish.

6.4 Conclusions

Ion beam-amorphized Si pillars show anisotropic plastic deformation under 30 MeV Cu ion irradiation at a transverse strain rate of $(2.5 \pm 0.2) \times 10^{-17}$ cm²/ion. In contrast, crystalline Si pillars irradiated under the same conditions do not show anisotropic deformation due to the lack of shear sites with local free volume. The relatively low value of the strain rate for pure a-Si compared to SiO₂ could be related to the smaller amount of free volume in a-Si, contraction of silicon upon melting, or its relatively high radiation-induced viscosity. By irradiation of partially amorphous structures, a variety of microshapes can be fabricated.

References

- ¹ S. Klaumünzer and G. Schumacher, Phys. Rev. Lett. **51**, 1987 (1983)
- ² M.-D. Hou, S. Klaumünzer, and G. Schumacher, Phys. Rev. B **41**, 1144 (1990)
- ³ A. Benyagoub, S. Löffler, M. Rammensee, S. Klaumünzer, and G. Saemann-Ischenko, Nucl. Instrum. Methods Phys. Res. B **65**, 228 (1992)
- ⁴ E. Snoeks, A. van Blaaderen, T. van Dillen, C. M. van Kats, M. L. Brongersma, and A. Polman, Adv. Mater. **12**, 1511 (2000)
- ⁵ T. van Dillen, A. Polman, C. M. van Kats, and A. van Blaaderen, Appl. Phys. Lett. **83**, 4315 (2003)
- ⁶ S. Klaumünzer, M. Rammensee, S. Löffler, H. C. Neitzert, and G. Saemann-Ischenko, J. Mater. Res. **6**, 2109 (1991)
- ⁷ T. Zijlstra, E. W. J. M. van der Drift, M. J. A. de Dood, E. Snoeks, and A. Polman, J. Vac. Sci. Technol. B **17**, 2734 (1999)
- ⁸ J. S. Custer, M. O. Thompson, D. C. Jacobson, J. M. Poate, S. Roorda, W. C. Sinke, and F. Spaepen, Appl. Phys. Lett. **64**, 437 (1994)
- ⁹ S. Klaumünzer, Changlin Li, S. Löffler, M. Rammensee, G. Schumacher, and H. Ch. Neitzert, Radiat. Eff. Defects Solids **108**, 131 (1989)
- ¹⁰ J. F. Ziegler, J. P. Biersack, and U. Littmark, *The Stopping and Range of Ions in Solids* (Pergamon Press, New York, 1985)
- ¹¹ H. Trinkaus and A. I. Ryazanov, Phys. Rev. Lett. **74**, 5072 (1995)
- ¹² E. Snoeks, T. Weber, A. Cacciato, and A. Polman, J. Appl. Phys. **78**, 4723 (1995)
- ¹³ M. Chicoine, S. Roorda, L. Cliche, and R. A. Masut, Phys. Rev. B **56**, 1551 (1997)
- ¹⁴ C. A. Volkert, J. Appl. Phys. **70**, 3521 (1991)

7

Stress map for ion irradiation: depth-resolved dynamic competition between radiation- induced viscoelastic phenomena in SiO₂

The dynamic competition between structural transformation, Newtonian viscous flow, and anisotropic strain generation during ion irradiation of SiO₂ leads to a strongly depth-dependent evolution of the mechanical stress, ranging between compressive and tensile. From independent in-situ stress measurements during irradiation, generic expressions are derived of the nuclear stopping dependence of both the structural transformation rate and the radiation-induced viscosity. Using these data we introduce and demonstrate the concept of a stress map that predicts the depth-resolved saturation stress in SiO₂ for any irradiation condition with ion energies up to several MeV.

7.1 Introduction

Ion irradiation is a widely used technique to modify the structure and composition of thin film materials. It is the key doping technology in integrated circuit manufacturing and is used to locally modify and tailor optical, magnetic, or mechanical properties of a wide range of materials. Over the past years ion irradiation has enabled a large number of important fundamental and technological innovations.

Ion irradiation can induce large changes in the mechanical stress state of a material. Surprisingly, this effect has only been marginally studied.¹⁻³ Yet, mechanical stress is known to affect important parameters such as thin film growth kinetics and stability, impurity diffusion, optical birefringence, and many other properties. For example, ion irradiation of amorphous SiO₂ causes a reduction in the mean Si-O-Si bridging bond angle, leading to a new structural state with a higher equilibrium density.⁴ This leads to the build-up of a tensile stress if the irradiated film is constrained on a substrate. Second, Newtonian viscous flow takes place, mediated by radiation-induced defects that relax the stress at a rate proportional to the stress.³⁻⁶ Third, as we described in Chapters 2-5, shear stresses, brought about by the expansion of the highly anisotropic ion-induced thermal spike, relax, generating anisotropic strain that freezes in as the thermal spike cools down.⁷ This results in the build-up of a compressive stress if the film is constrained on a substrate.

In the past we have developed a qualitative model to describe the stress evolution in SiO₂ during ion irradiation, taking into account the interplay between the three ion irradiation-induced processes. For ion energies in the range between 100 keV up to several MeV this model describes the measured mean stress evolution reasonably well.³ Even though this model appears successful, it is only a rough approximation and its applicability is limited, since it does not take into account the depth-dependence of each of the radiation-induced effects in the film. However, each of the three effects strongly depends on either the nuclear or electronic stopping, which are both highly depth-dependent.

In this chapter we will for the first time evaluate the depth-dependence of the local stress in SiO₂ due to the depth-dependence of the electronic and nuclear stopping. We will demonstrate that the local stress shows giant variations with depth of several hundred MPa, even ranging between compressive and tensile. The model also solves a long-standing contradiction between the theory and some of our experiments, where an apparent tensile saturation stress is observed experimentally for Xe irradiations at energies below 3.5 MeV,³ while anisotropic strain generation would be expected to drive the stress to a compressive value. Using this new model it now becomes possible to construct “stress maps” that can be used to predict the local saturation stress in SiO₂ for any ion/energy

combination. In our analysis we limit ourselves to ion energies up to a few MeV, where electronic stopping effects on densification and Newtonian flow are negligible.

7.2 Description of the model

As a starting point we use the solution of a differential equation that describes the interplay between the three ion irradiation-induced processes^{3,8} and gives the in-plane stress as a function of ion fluence:

$$\sigma(\phi) = Y_{ox} \left[(-\varepsilon_1 + \varepsilon_{SAT} - C) \cdot \exp\left(-\frac{Y_{ox}}{6\eta_{RAD}}\phi\right) + C \cdot \exp\left(-\frac{\phi}{\phi_s}\right) - \varepsilon_{SAT} \right], \quad (7.1)$$

where $C=6\eta_{RAD}(\varepsilon_2-\varepsilon_1)/(6\eta_{RAD}-Y_{ox}\phi_s)$ and $\varepsilon_{SAT}=-6A\eta_{RAD}/Y_{ox}$. Here we have assumed a damage overlap model for structural transformation,⁹ where the in-plane strain evolves exponentially from ε_1 to ε_2 with a characteristic fluence ϕ_s , Newtonian viscous flow with a radiation-induced viscosity η_{RAD} and anisotropic strain generation at a constant rate A . In Eq. (7.1), Y_{ox} is the biaxial stress state modulus of the SiO₂ film and compressive stress is defined to be positive.

Next we take into account the stopping dependence of the parameters ϕ_s , η_{RAD} and A in SiO₂. Experiments by Devine *et al.* have shown that structural transformations occur at a characteristic fluence: $\phi_s = \kappa F_n^{-\lambda}$, with F_n the nuclear stopping.⁴ Previous measurements by Snoeks *et al.* have shown that the radiation-induced viscosity decreases with F_n as: $\eta_{RAD} = \alpha F_n^{-\delta}$.³ Both λ and δ are of order 1. The dependence of ϕ_s and η_{RAD} on the nuclear stopping holds for ion energies up to several MeV. For much higher energies also the electronic stopping will affect densification and stress relaxation by Newtonian flow.^{4,10,11} Benyagoub and others have shown that the anisotropic strain generation rate A for pure silica increases linearly with electronic stopping (F_e) above a threshold:¹² $A=c\times(F_e-F_{th})$, with $c=3.38\times 10^{-17}$ cm²×nm/keV. Using these parameters, $F_{th}=0.6$ keV/nm, and Eq. (7.1) we can now calculate the fluence dependence of the local stress at each depth z , with the depth-dependent stopping $F_e(z)$ and $F_n(z)$ as input.

To obtain the depth-dependence of the electronic and nuclear stopping, we have used the SRIM 2000 computer code.¹³ This program is a Monte Carlo simulation that calculates, after specifying the irradiation conditions and the target material, the ion trajectories and the ion-solid interactions at any irradiation depth.

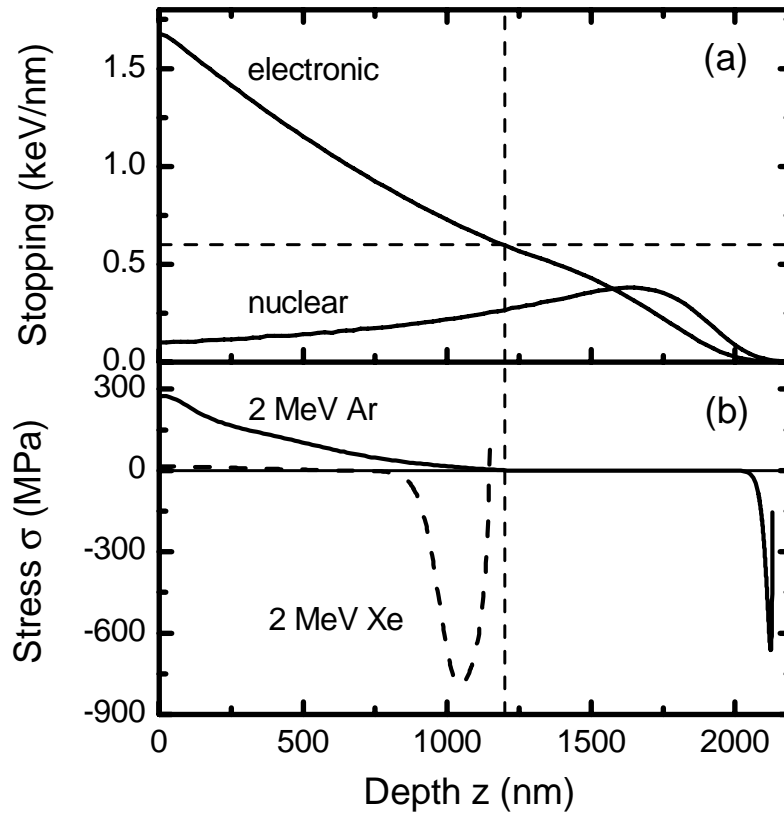


Figure 7.1 (a) Electronic and nuclear stopping (F_e and F_n) as a function of the depth z for 2 MeV Ar irradiation of SiO_2 . The threshold stopping for anisotropic strain generation ($F_{th} = 0.6$ keV/nm) and the corresponding depth (1200 nm) are indicated by the dashed lines. (b) Local stress as a function of depth for 2 MeV Ar (7×10^{14} Ar/cm², solid line) and 2 MeV Xe (1×10^{14} Xe/cm², dashed line) irradiation of SiO_2 .

7.3 Depth dependence of the in-plane stress

Figure 7.1(a) shows $F_e(z)$ and $F_n(z)$ for 2 MeV Ar irradiation of a SiO_2 film on Si. Figure 7.2(a) shows the corresponding local in-plane stress as a function of Ar ion fluence for three different depths, calculated using Eq. (7.1) and characteristic parameters as will be discussed later on. The solid line in Fig. 7.2(a) represents the local stress at the surface of the film ($z=0$). The initial stress, before irradiation, is taken to be compressive at the experimental value of 260 MPa. It is due to the difference in thermal contraction between the SiO_2 film and the Si substrate upon cooling down the substrate to room temperature after thermal oxidation at 1050 °C.³ Upon irradiation the near-surface stress first changes from compressive to tensile. This is due to the structural changes that compact the silica network. After a maximum tensile stress is reached, the stress

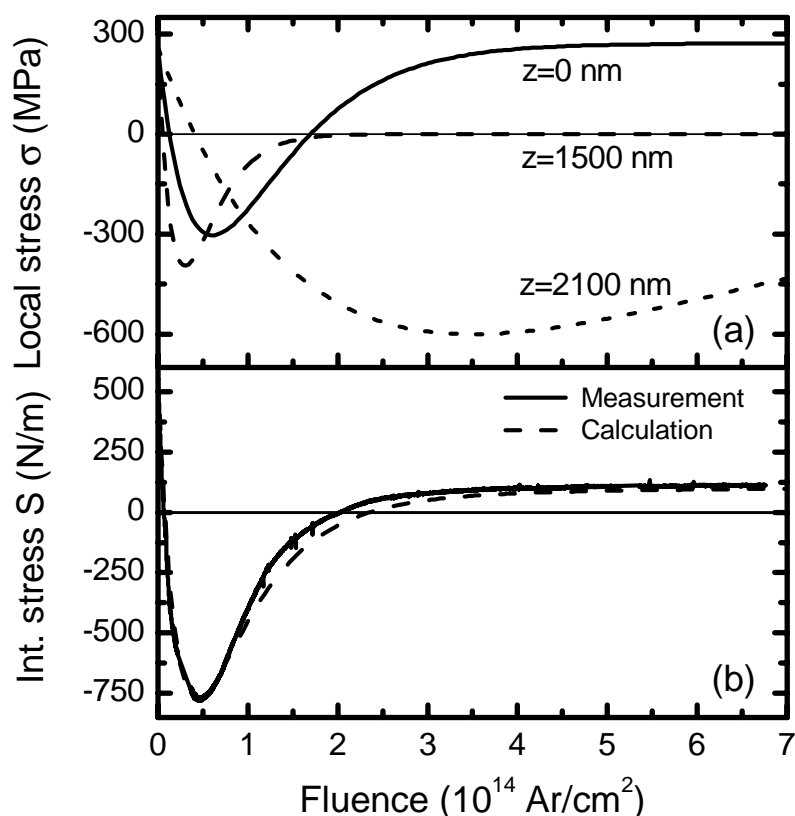


Figure 7.2 (a) Local stress as a function of fluence, calculated using Eq. (7.1), for 2 MeV Ar irradiation of SiO_2 at three different depths indicated in the figure. (b) *In-situ* measurement of the integrated stress S as a function of ion fluence during 2 MeV Ar irradiation of SiO_2 at 115 K (solid line). The dashed line represents a calculation by the local stress model using integration of Eq. (7.1).

relaxes due to Newtonian viscous flow. Ultimately, a compressive saturation stress as high as 270 MPa is reached. This saturation stress is a result of a dynamic competition between compressive anisotropic stress generation (with strain rate A) and stress relaxation due to Newtonian viscous flow (with viscosity η_{RAD}) and amounts to $6A\eta_{RAD}$ [the high-fluence limit of Eq. (7.1)]. The large saturation stress near the surface results from the high anisotropic strain rate due to the high electronic stopping as the ion energy is still high, and the high viscosity due to the relatively small nuclear stopping [see Fig. 7.1(a)].

An entirely different behavior is observed deeper in the film, at $z=1500 \text{ nm}$ [dashed curve in Fig. 7.2(a)]. At this depth the electronic stopping is below the threshold for anisotropic strain generation and the high-fluence limit of Eq. (7.1) is zero. Stress relaxation at this depth occurs slightly faster than at the surface due to the higher nuclear stopping. Fig. 7.2(a) also shows the stress evolution at the end-of-range of the ions ($z=2100 \text{ nm}$, dotted line) where the

nuclear stopping is small and structural changes and radiation-induced flow therefore occur at a slower rate, as is observed in the calculation.

From Fig. 7.2(a) we can immediately conclude that at a fixed fluence the local stress is strongly dependent on the depth in the irradiated film. For example, at a fluence of 3×10^{14} Ar/cm², the surface stress is highly compressive (200 MPa) while at the end-of-range the stress is highly tensile (-600 MPa). Such giant stress inhomogeneities in thin films under ion irradiation have never been considered before. To further illustrate the depth-dependence of the stress, Fig. 7.1(b) plots the local stress as a function of depth for 2 MeV Ar irradiation at a fluence of 7×10^{14} ions/cm² (solid line). A high compressive stress is seen just below the surface, the stress then decreases with depth and finally vanishes at 1200 nm. The latter is the depth at which the electronic stopping is equal to the threshold stopping for anisotropic strain generation [see dashed lines in Fig. 7.1(a)]. At the end-of-range of the ions, around 2100 nm, a narrow tensile stress region is observed, as explained above.

Figure 7.2(b) shows a measurement (solid line) of the integrated in-plane stress S as a function of the ion fluence during 2 MeV Ar irradiation of a 2.5 μm thick thermally grown SiO₂ film on a 150 μm thick Si(100) substrate at a temperature of 115 K. These data were taken using an *in-situ* wafer curvature technique² that probes the integrated stress rather than the local stress in the film. Since our model provides the local stress at each depth, we can calculate the depth-integrated stress at any fluence. This calculation is also shown in Fig. 7.2(b) (dashed line). As can be seen, the calculation corresponds closely with the measurement.

In fitting our model we have optimized the functions $\phi_s = \kappa F_n^{-\lambda}$ and $\eta_{RAD} = \alpha F_n^{-\delta}$ to obtain good agreement for three independent measurements of the integrated stress as a function of fluence (1 MeV Ne, 2 MeV Ar and 2 MeV Xe) using an iteration procedure. Note that the three irradiations, with very different ion masses, lead to entirely different depth profiles of F_e and F_n . These three different measurements were all fitted using the same set of input functions for ϕ_s and η_{RAD} : $\phi_s(\text{ions/cm}^2) = 1.46 \times 10^{13} F_n^{-0.55}$ and $\eta_{RAD}(\text{Pa ion/cm}^2) = 1.79 \times 10^{23} F_n^{-0.83}$, with F_n in units of keV/nm. The fact that these exponents are smaller than unity may point to defect reactions by thermally activated processes.¹⁴

As an illustration of how these generic expressions consistently describe entirely different experiments, we show in Fig. 7.3 a measurement of the integrated stress as a function of fluence during 2 MeV Xe irradiation of a SiO₂ film on Si performed at 115 K (solid line). The stress curve exhibits a totally different behavior than for 2 MeV Ar irradiation; the most striking difference is the apparent high-fluence saturation stress that is now tensile. Nevertheless, the calculation (dashed line in Fig. 7.3) performed using the same set of input functions as used for the calculation of the 2 MeV Ar irradiation shows very good agreement with the measurement.

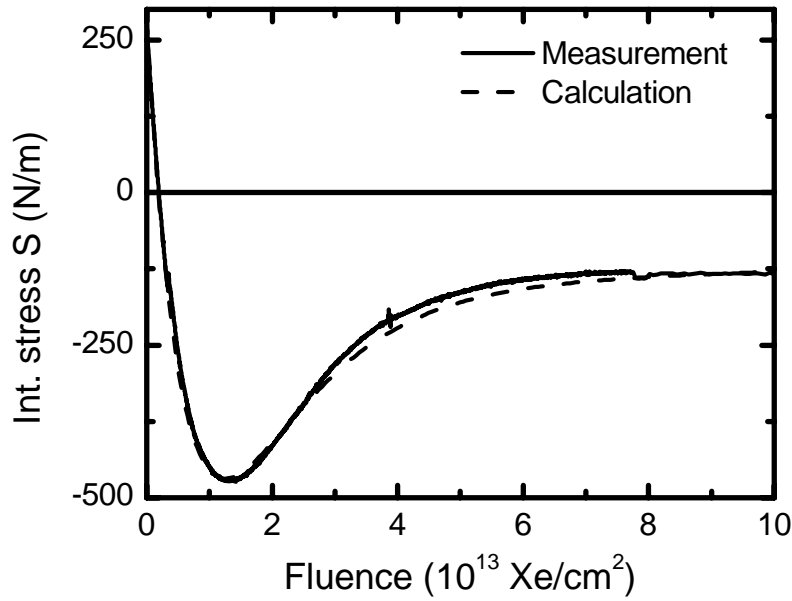


Figure 7.3: *In-situ* measurement of the integrated stress in a SiO₂ film as a function of ion fluence during 2 MeV Xe irradiation at 115 K (solid line). A calculation by the local stress model using integration of Eq. (7.1) is also included (dashed line).

This analysis now provides a consistent explanation for the tensile saturation stress that had remained controversial and unexplained to date. This tensile stress now naturally follows from our model as can be seen in Fig. 7.1(b), which shows the local stress as a function of depth for 2 MeV Xe irradiation at a fluence of 1×10^{14} Xe/cm² (dashed line). Clearly, the large ion straggle for Xe leads to a broad tensile contribution at the end-of-range, thus leading to a tensile integrated stress.

7.4 Stress map for ion irradiation

Finally, by analogy of the deformation mechanism map that predicts stress-strain-temperature behavior for materials, we introduce the new concept of a “stress map” for ion irradiation. Since the anisotropic strain generation rate A depends on the electronic stopping F_e and the radiation-induced viscosity η_{RAD} on the nuclear stopping F_n (for ion energies up to several MeV), the saturation stress $\sigma_{SAT} = 6A\eta_{RAD}$ can be calculated for any irradiation condition. These data can be plotted on a stress map in which iso-saturation stress contours are plotted versus F_e and F_n , as is shown in Fig. 7.4. For F_e below 0.6 keV/nm the saturation stress vanishes. It can immediately be seen that a high electronic energy loss and a small nuclear energy loss results in a high local saturation stress. In contrast, a

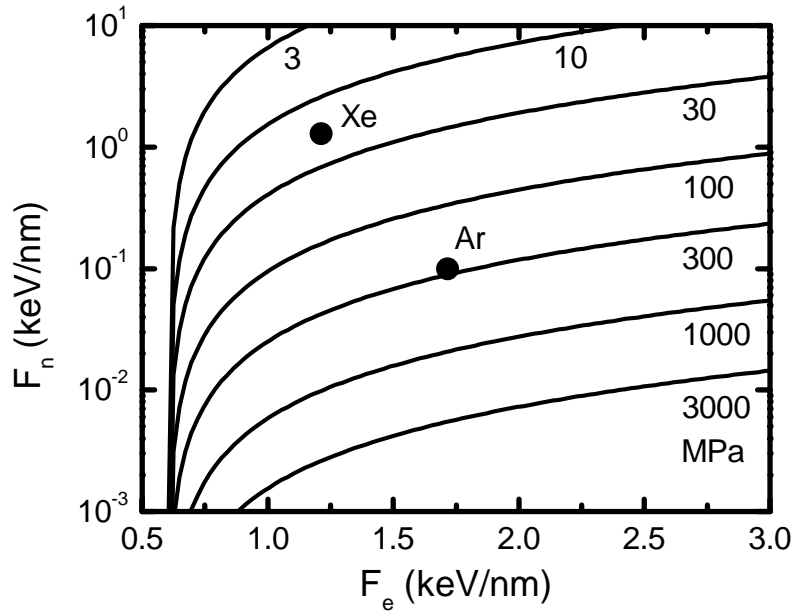


Figure 7.4: Stress map of SiO₂ at 115 K under ion irradiation. Plotted are iso-stress curves of the high-fluence saturation stress $\sigma_{SAT}=6A\eta_{RAD}$ (values indicated in units of MPa) as a function of the electronic stopping F_e and the nuclear stopping F_n . The near-surface saturation stress ($z=0$ nm) for 2 MeV Ar and 2 MeV Xe irradiation is also shown (solid circles).

small value of the saturation stress occurs in regions where F_n is high and F_e small.

For comparison, the solid dots in Fig. 7.4 indicate the calculated near-surface saturation stress for 2 MeV Ar and 2 MeV Xe irradiations, taken from Fig. 7.1(b). The 2 MeV Ar irradiation results in a much higher saturation stress (~ 270 MPa) than the 2 MeV Xe irradiation (~ 20 MPa) due to the smaller nuclear stopping. Using the stress map in Fig. 7.4 we can now predict the final saturation stress in SiO₂ for any irradiation condition (energy, ion) at 115 K with ion energies up to several MeV. Since the temperature dependence of both the anisotropic strain generation rate A and the radiation-induced viscosity η_{RAD} are known,⁸ stress maps for SiO₂ at other temperatures can also be made. Finally, since η_{RAD} and A have been determined for other materials as well,¹⁵⁻¹⁷ stress maps for these materials may also be constructed.

7.5 Conclusions

We have for the first time calculated the depth-dependent mechanical stress induced by the interplay between densification by structural transformation, Newtonian viscous flow and anisotropic strain generation in a constrained SiO₂

film, by taking into account the electronic and nuclear stopping dependence of these processes. As a function of the depth, the stress shows giant variations of several hundred MPa ranging between compressive and tensile. Finally, we have constructed a stress map that can predict the final saturation stress in SiO₂ at any depth in the film for any irradiation condition with ion energies up to several MeV.

References

- ¹ A. Misra, S. Fayeulle, H. Kung, T. E. Mitchell, and M. Nastasi, *Appl. Phys. Lett.* **73**, 891 (1998)
- ² C. A. Volkert, *J. Appl. Phys.* **70**, 3521 (1991)
- ³ E. Snoeks, T. Weber, A. Cacciato, and A. Polman, *J. Appl. Phys.* **78**, 4723 (1995)
- ⁴ R. A. B. Devine, *Nucl. Instrum. Methods Phys. Res. B* **91**, 378 (1994)
- ⁵ C. A. Volkert and A. Polman, *Mater. Res. Soc. Symp. Proc.* **235**, 3 (1992)
- ⁶ S. G. Mayr, Y. Ashkenazy, K. Albe, and R. S. Averback, *Phys. Rev. Lett.* **90**, 055505 (2003)
- ⁷ H. Trinkaus and A. I. Ryazanov, *Phys. Rev. Lett.* **74**, 5072 (1995)
- ⁸ M. L. Brongersma, E. Snoeks, T. van Dillen, and A. Polman, *J. Appl. Phys.* **88**, 59 (2000)
- ⁹ F. F. Morehead, Jr. and B. L. Crowder, *Radiat. Eff.* **6**, 27 (1970)
- ¹⁰ A. Benyagoub, S. Klaumünzer, and M. Toulemonde, *Nucl. Instrum. Methods Phys. Res. B* **146**, 449 (1998)
- ¹¹ A. Audouard, E. Balanzat, J. C. Jousset, D. Lesueur, and L. Thomé, *J. Phys. Condens. Matter* **5**, 995 (1993)
- ¹² A. Benyagoub, S. Löffler, M. Rammensee, S. Klaumünzer, and G. Saemann-Ischenko, *Nucl. Instrum. Methods Phys. Res. B* **65**, 228 (1992)
- ¹³ J. F. Ziegler, J. P. Biersack, and U. Littmark, *The Stopping and Range of Ions in Solids* (Pergamon Press, New York, 1985)
- ¹⁴ D. L. Griscom, M. E. Gingerich, and E. J. Friebele, *Phys. Rev. Lett.* **71**, 1019 (1993)
- ¹⁵ E. Snoeks, K. S. Boutros, and J. Barone, *Appl. Phys. Lett.* **71**, 267 (1997)
- ¹⁶ S. Klaumünzer, *Radiat. Eff. Defects Solids* **110**, 79 (1989)
- ¹⁷ M.-d. Hou, S. Klaumünzer, and G. Schumacher, *Phys. Rev. B* **41**, 1144 (1990)

8 *Activation energy spectra for annealing of ion irradiation-induced defects in silica glasses*

In-situ stress measurements were performed on alkali-borosilicate glass samples during and after 2 MeV Xe ion irradiation at several temperatures between 95 and 580 K. After switching off the ion beam, stress changes are observed that are related to the annealing of ion beam generated defects. The activation energy spectra for defect annealing are obtained from the data at each irradiation temperature. Defects are observed in the energy range from 0.26 and 1.85 eV. At each temperature the spectrum increases monotonously with activation energy. At each energy the defect density per unit energy is smaller at higher temperatures. This behavior can be explained using a binary collision model. The data are contrasted with the results obtained for 4 MeV Xe ion irradiation of thermally grown SiO₂ films, which can be explained using a thermal spike model. Measurements of the radiation-induced viscosity support the difference in mechanisms. The difference in defect spectra may be attributed to the difference in glass composition.

8.1 Introduction

The effect of ion irradiation on the structure of silica glasses has been studied for many years, and many of the radiation-induced phenomena that can occur are now well established. For example, ion irradiation can cause structural transformations in which rearrangements in the glass network topology take place.¹ When the irradiated region is constricted by a substrate, such changes may lead to the build-up of mechanical stress in the material. This stress can be relaxed by radiation-induced viscous flow.^{2,3} In addition, as described in the previous chapters, ion irradiation may cause anisotropic deformation in amorphous materials,⁴⁻⁶ leading to stress in the plane perpendicular to the direction of the ion beam.^{2,7}

Ion irradiation also leads to the generation of point defects or larger defect agglomerates. Spectroscopic techniques have been used to try to identify the charge state and bonding nature of these defects.^{1,8} Little is known, however, about the typical annihilation activation energies of these defects and their steady state concentration as a function of activation energy. One way to study this is by measuring the mechanical stress in an irradiated region that has built up due to the excess volume generated by such defects.² In this chapter, we present time-resolved stress measurements during and after 2 MeV Xe ion irradiation of alkali-borosilicate glass and of SiO₂ films that are thermally grown on Si. Measurements are performed at different irradiation temperatures in the range from 95-580 K. The results are compared with similar measurements that were performed earlier on thermally grown SiO₂ films under 4 MeV Xe irradiation.^{3,9} Some striking differences between the defect spectra are found, and are related to a fundamental difference in the nature of the defect generation process.

8.2 Experimental

Measurements were performed on 150 μm thick rectangular bulk alkali-borosilicate glass samples ($6\times 23\text{ mm}^2$, Menzel cover glasses). Rutherford backscattering spectrometry and elastic recoil detection show that this glass contains (besides Si and O) approximately 4.7 at% Na, 3.7 at% B and also small concentrations of K, Ca, Ti and Zn.

One end of the samples was clamped to a temperature-controlled copper block, leaving the other end free to bend. The bare glass-side of the samples was homogeneously irradiated with a 2 MeV Xe ion beam that was electrostatically scanned over the sample at an ion flux of $(4.0-9.0)\times 10^{10}$ ions/cm²s. The maximum ion range was about 1.0 μm .² During irradiation the radius of

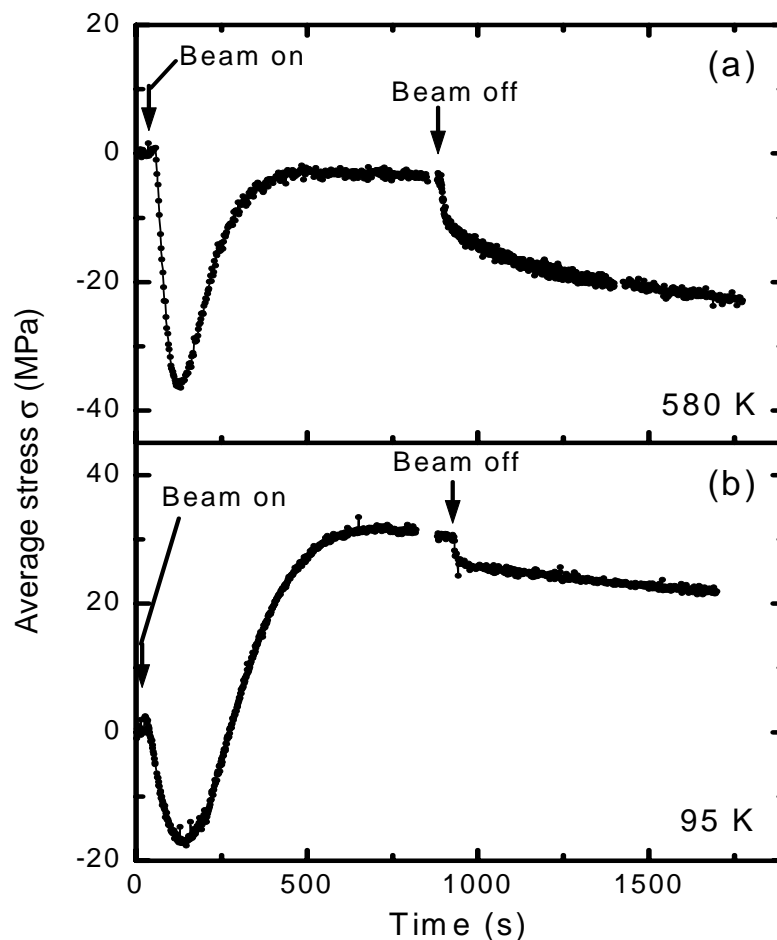


Figure 8.1 In-situ measurements of the average in-plane stress σ of alkali-borosilicate glass before, during and after 2 MeV Xe ion irradiation as a function of time. Results are shown for a sample temperature of 580 K (a), and 95 K (b). The ion beam was switched off after a total irradiation fluence of 8×10^{13} Xe/cm² (a), 4.3×10^{13} Xe/cm² (b).

curvature of the sample was measured using a sensitive scanning laser technique, from which the *average* in-plane stress σ in the irradiated region was derived.¹⁰ In order to obtain a good reflection from the sample a 50 nm thick Cr film was evaporated on the backside of the sample. The measurements were performed at fixed temperatures between 95 and 580 K.

In addition, measurements were performed on 2.4 μm thick SiO₂ films grown by wet thermal oxidation (1100 °C) on 95 μm thick Si (100) substrates. These films were homogeneously irradiated with 2 MeV Xe ion beam at a flux of $(1.0\text{-}1.5) \times 10^{11}$ ions/cm²s at fixed sample temperatures between 90 and 375 K.

8.3 Results and analysis

We will first describe the data measured on the alkali-borosilicate glass samples. Figure 8.1(a) shows a typical stress measurement as a function of time during and after ion irradiation at a temperature of 580 K. The ion beam is switched on at $t=54$ s and switched off at $t=893$ s. Compressive stress is defined to be positive. After switching on the ion beam there is small initial increase in the stress. The stress then becomes tensile and reaches a maximum tensile stress at $t=130$ s, corresponding to a Xe fluence of 7.3×10^{12} cm⁻². The stress then turns towards compressive values and saturates at a value of -3 MPa after ~ 500 s, corresponding to a fluence of about 4×10^{13} Xe cm⁻².

As shown previously, the stress changes during ion irradiation are caused by different processes that occur simultaneously.^{3,9} The small initial peak is caused by stress induced by the creation of volume occupying defects in the glass as the ion beam is switched on. The subsequent change towards tensile stress is attributed to a structural change of the glass.^{1,9} At the same time, radiation-induced viscous flow occurs, a continuous stress-driven process that eventually relaxes the stress towards zero. Figure 8.1(b) shows a stress measurement at a temperature of 95 K. It shows the same features as the data in Fig. 8.1(a), except that the stress saturates at a positive value. As described earlier (see also Chapters 2-7), this is due to anisotropic strain generation that occurs most efficiently at low irradiation substrate temperature (see Chapter 4).^{2,4-7,9} The interplay between the latter three processes and the resulting (depth-dependent) stress evolution *during* ion irradiation is described in detail in Chapter 7.

After switching off the ion beam the stress changes towards tensile values as can be seen in Fig. 8.1 both at 95 K and 580 K. The same effect was also observed in measurements performed at intermediate temperatures.¹¹ This stress change is attributed to the annealing of volume occupying defects (generated by the ion beam) that have a spectrum of annihilation times. The densification is given by^{9,12,13}

$$\Delta\rho(\theta) = \Delta\rho_{\infty} - \int_0^{\infty} D(Q) \exp\left[-\frac{\theta}{\tau(Q)}\right] dQ \quad , \quad (8.1)$$

where $D(Q)$ is the density change per unit energy, θ is time after switching off the beam and $\tau(Q)$, given by

$$\tau(Q) = \frac{h}{kT} \exp\left[\frac{Q}{kT}\right] \quad , \quad (8.2)$$

is the characteristic annihilation time of defects with an activation energy Q . In Eq. (8.2) k and h are Boltzmann's and Planck's constants, respectively, and T is the temperature.

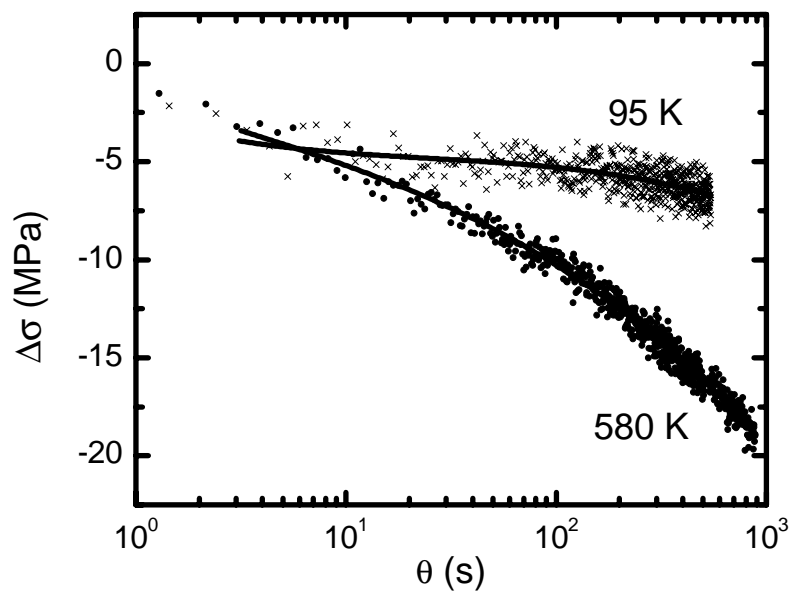


Figure 8.2 The stress change $\Delta\sigma$ from Fig. 8.1 (relative to saturation stress) after switching off the ion beam, plotted as a function of the time θ after switching off the ion beam. Results are shown for the alkali-borosilicate glass at sample temperatures of 580 and 95 K. At both temperatures the samples were first irradiated to reach a saturation stress value. The drawn lines are polynomial fits through the data.

If the defect activation energy spectrum is very broad and varies slowly with activation energy it follows from Eq. (8.2) that at a time θ after switching off the ion beam defects with activation energies in a small band of order kT around

$$Q_\theta = kT \ln[\theta \cdot kT / h] \quad (8.3)$$

are annealing out, resulting in a certain stress change. The spectrum $D(Q_\theta)$ can then be approximated from the measured stress change by⁹

$$D(Q_\theta) = \frac{-3\rho}{kT \cdot Y_b} \frac{d(\Delta\sigma)}{d(\ln[\theta \cdot kT / h])} \quad , \quad (8.4)$$

where $\Delta\sigma$ is the stress change after switching off the ion beam with respect to the saturation stress ($\Delta\sigma < 0$), ρ is the density of the silica glass (6.9×10^{22} atoms/cm³) and Y_b the biaxial modulus of the modified region of the glass (90 GPa).² It should be noted here that, in contrast to Chapter 7 where we have demonstrated that the local stress is strongly depth-dependent, we have taken the *average* in-plane stress σ for our analysis. The spectrum $D(Q)$ is therefore a depth-averaged quantity without any local information.

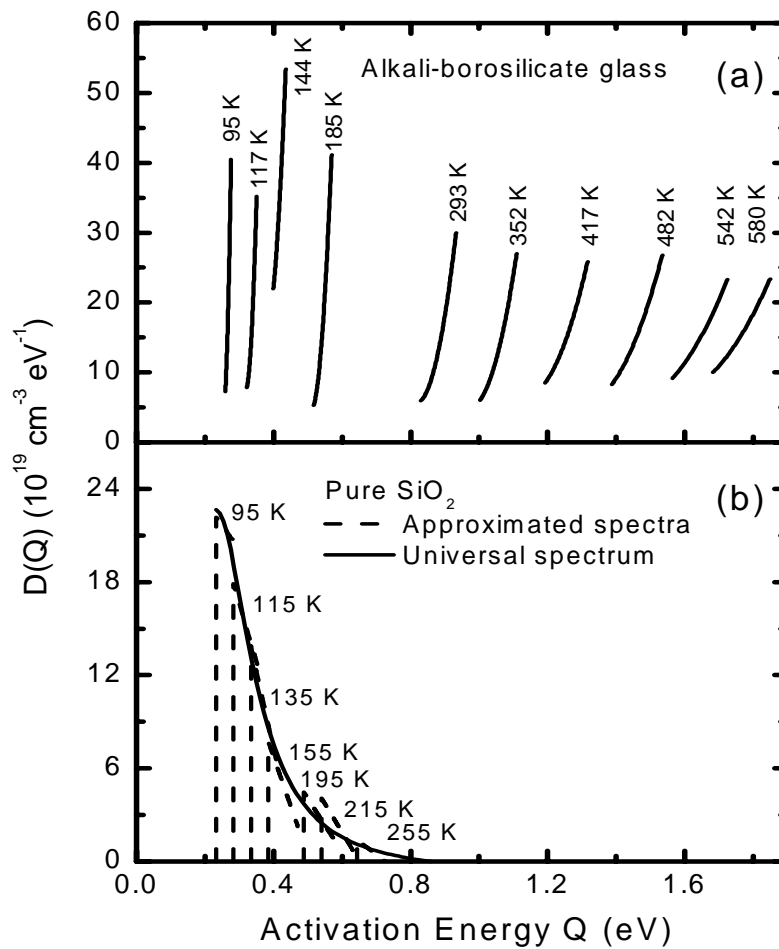


Figure 8.3 (a) Defect annihilation activation energy spectra for alkali-borosilicate glass derived from the data in Fig. 8.2 and from additional data taken at other temperatures (all after irradiation with 2 MeV Xe at a flux of $(4-9) \times 10^{10}$ ions/cm²s). (b) The same for thermally grown SiO_2 films on Si (after irradiation with 4 MeV Xe at a flux of 5×10^{12} ions/cm²s).

Figure 8.2 shows the transient stress change from Fig. 8.1 after switching off the ion beam plotted on a logarithmic time scale. According to Eq. (8.4) the spectra $D(Q)$ can now be calculated by taking the derivative of $\Delta\sigma$ with respect to $\ln[\theta \cdot kT/h]$. This is done by fitting a 3rd order polynomial to the data and then taking the derivative of these curves versus $\ln[\theta]$. The result is shown in Fig. 8.3(a), where $D(Q)$ is plotted versus Q for the temperatures between 95 and 580 K. To avoid possible contributions from beam heating on the stress measurement only data for $\theta > 30$ s are used.

8.4 Discussion

As can be seen in Fig. 8.3(a), at each temperature the spectrum for $D(Q)$ increases with increasing Q . It can also be seen that at a fixed activation energy the defect density per unit energy decreases with increasing sample temperature.

We will compare these spectra of alkali-borosilicate glass with activation energy spectra derived from stress measurements performed on 2.4 μm thick, thermally grown SiO_2 films on Si.⁹ These measurements were performed after a 4 MeV Xe^{4+} irradiation at a flux of 5.0×10^{12} $\text{Xe}/\text{cm}^2\text{s}$, and data for four different temperatures taken from Ref. 9 are shown in Fig. 8.4. The stress relaxation curves in Fig. 8.4 and additional curves taken at different temperatures were analysed as described above to obtain the defect spectra $D(Q)$. The result is plotted for different temperatures in Fig. 8.3(b). All spectra decrease gradually as a function of the activation energy Q .

By comparing all spectra for pure silica measured at different temperatures they seem to fit one ‘universal’ continuous spectrum independent of temperature. To confirm this, a smooth curve $D(Q)$ was fitted to the spectra of Fig. 8.3(b) (drawn line). The time dependence of the stress change was then calculated using this spectrum, Eq. (8.1), and the relation $\Delta\rho/\rho = -3\Delta\sigma/Y_b$.² The result is shown for the four temperatures in Fig. 8.4. Good agreement with the measured data is observed. Comparing the spectra of the two glass types it can first be concluded that defects are more stable in alkali-borosilicate glass, because the spectrum of alkali-borosilicate glass has non-zero values up to at least 1.85 eV whereas for the thermal oxide the spectrum vanishes above 0.75 eV.

The existence of a universal spectrum for thermal SiO_2 can be explained using a thermal spike model,⁹ in which the defect generation is independent of sample temperature, as the temperature in the thermal spike^{3,9,14} is much higher than the sample temperature. The defect population that is probed by the stress measurement would then be generated during the thermal spike that causes local melting of the SiO_2 film, and quenched in during rapid cooling.

The fact that this ‘universal’ behavior is not found for alkali-borosilicate glass implies that in this glass the steady state concentration of defects depends on sample temperature. This can be explained by a binary collision model for which, in contrast to a thermal spike, an ion impact does not cause local melting but produces isolated defects as a result of binary collisions. In this case, a steady state defect population builds up due to temperature-independent defect generation and temperature-dependent defect annihilation. The steady state defect population then depends on the annihilation activation energy Q , the sample temperature and the maximum concentration of defects that can be generated for each Q . Because the annihilation rate $1/\tau$ [with τ from Eq. (8.2)] is larger for higher temperatures, the steady state defect population for a fixed

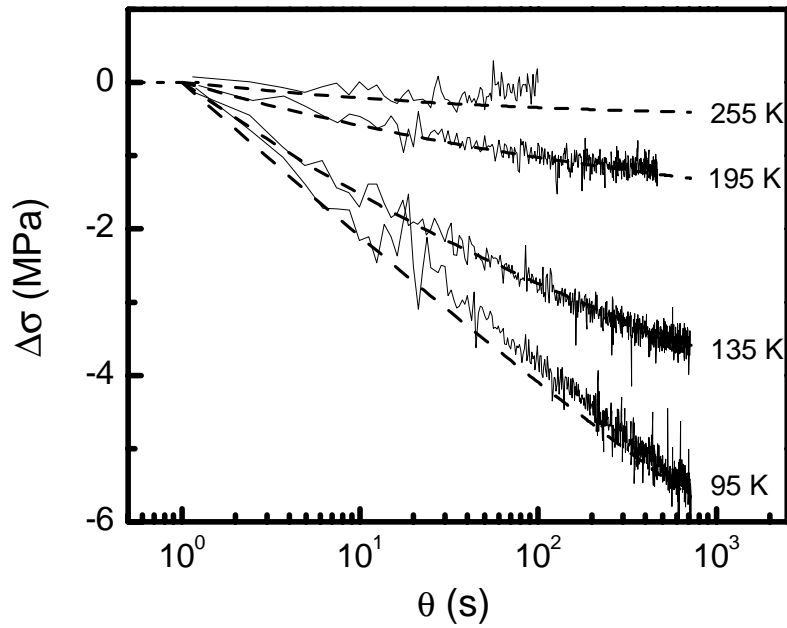


Figure 8.4 The average in-plane stress change in the SiO_2 film after the 4 MeV Xe ion beam was switched off (Data from Ref. 9). Results are shown for four sample temperatures 95, 135, 195 and 255 K. The dashed lines are calculations of these stress changes using the universal spectrum in Fig 8.3(b) and Eq. (8.1).

activation energy is smaller for higher temperatures, which is in agreement with the data in Fig. 8.3(a).

Additional indications for the different nature of the defect generation in the two cases are found by comparing the temperature dependencies of the radiation-induced viscosity $\eta_{rad}^{2,3,7,9}$ for both glass types. These data are derived from stress relaxation measurements *during* ion irradiation. We estimated η_{rad} by fitting an exponential function to the part of the stress curve (see Fig. 8.1) between ~ 300 and 700 s (fluence $\geq 1.5 \times 10^{13}$ Xe/cm²), the same method as used in Ref. 3. The results are shown in Fig. 8.5. As can be seen, the viscosity for alkali-borosilicate glass (triangles) slowly increases with increasing temperature from $(0.75 \pm 0.10) \times 10^{23}$ Pa ion/cm² at 95 K to $(1.1 \pm 0.10) \times 10^{23}$ Pa ion/cm² at 580 K. For comparison, the data for pure SiO_2 (solid squares, taken from Ref. 3) are included. These data show an opposite behavior of η_{rad} , in agreement with calculations using a thermal spike model (the drawn line in Fig. 8.5).³ This provides independent evidence that the defect generation in alkali-borosilicate glass is not governed by a thermal spike process.

To further investigate the universality of the defect spectra $D(Q)$ for pure silica in Fig. 8.3(b) we varied both the ion energy and flux. First, 2 MeV Xe ions were studied at the same flux of $(1.0-1.5) \times 10^{11}$ Xe/cm²s as used for the 4 MeV irradiation as described above. Fig. 8.6 shows the average in-plane stress change (relative to the saturation stress) after switching off the ion beam after these

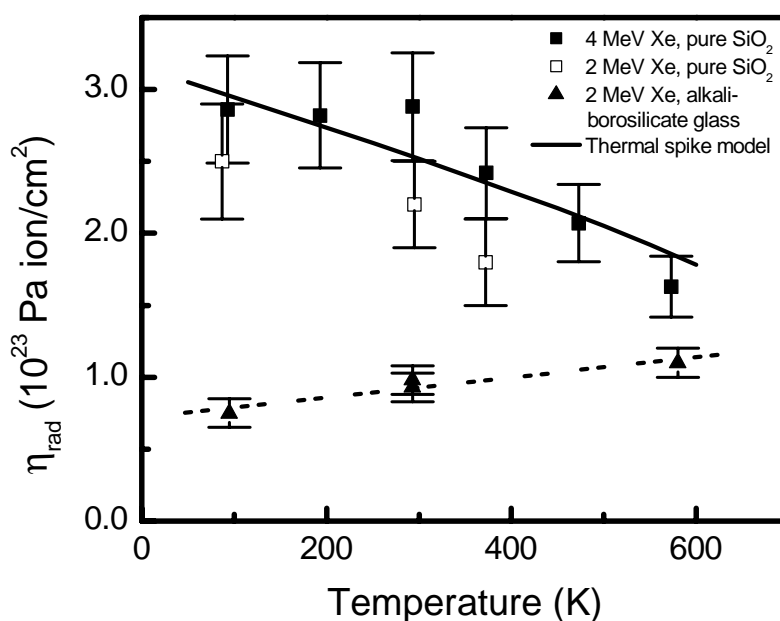


Figure 8.5 The radiation-induced viscosity η_{rad} , derived from stress relaxation measurements during Xe ion irradiation, plotted as a function of temperature for 2 MeV irradiation of alkali-borosilicate glass (triangles) and 4 MeV irradiation of thermally grown SiO₂ films at a flux of $\sim 10^{11}$ Xe/cm²s (solid squares). The solid line is a calculation of η_{rad} according to a thermal spike model (multiplied by a factor 4.7 to obtain agreement between the model and the data).³ The dashed line is a guide to the eye for alkali-borosilicate glass. Data for irradiations of thermal SiO₂ using 2 MeV Xe ions are also shown (open squares).

irradiations. Data are shown for three sample temperatures: 120, 145 and 170 K. Next, the time dependence of the stress change was calculated using the universal spectrum derived from the 4 MeV data [Fig. 8.3(b)] and Eq. (8.1). The result is shown in Fig. 8.6 (dashed lines). Again good agreement with the measured data is observed, indicating that the defect activation energy spectrum of thermally grown SiO₂ does not depend on irradiation energy in the 2-4 MeV Xe ion energy range. To study the dependence of the defect spectrum on the ion beam flux, we raised the flux for 2 MeV irradiation of thermal SiO₂ to $\sim 5 \times 10^{11}$ Xe/cm²s (at 95 K). No beam flux dependence was found in the structural relaxation behavior.¹⁵

We also investigated the temperature dependence of the radiation-induced viscosity of thermal SiO₂, using a 2 MeV Xe ion beam at a flux of $(1.0-1.5) \times 10^{12}$ Xe/cm²s. These data are shown in Fig. 8.5 (open squares). The viscosity decreases from $(2.5 \pm 0.4) \times 10^{23}$ Pa ion/cm² at 90 K to $(1.8 \pm 0.3) \times 10^{23}$ Pa ion/cm² at 375 K. As can be seen, the radiation-induced viscosity for 2 MeV irradiation is very similar to that for 4 MeV irradiation (closed squares). Finally, from additional post-irradiation wafer curvature experiments (not shown) we could

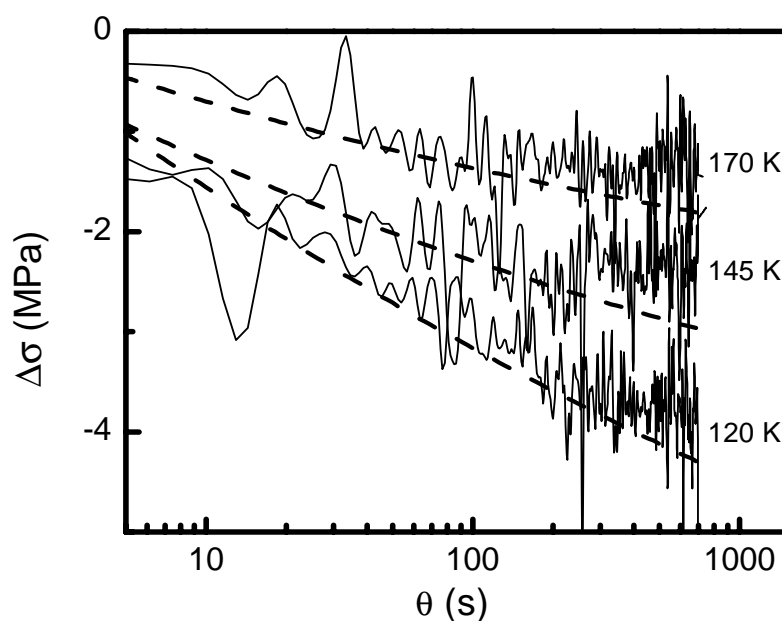


Figure 8.6 The average in-plane stress change in thermal SiO_2 films after switching off a 2 MeV Xe ion beam (flux: $(1-1.5)\times 10^{11}$ Xe/cm²s). Results are shown for three sample temperatures 120, 145 and 170 K. The dashed lines are calculations of these stress changes using the universal spectrum in Fig. 8.3(b) (derived from the 4 MeV Xe irradiations) and Eq. (8.1).

also conclude that the defect activation energy spectrum of alkali-borosilicate glass at 4 MeV is similar to that at 2 MeV.¹⁵

The different behavior found for pure silica and alkali-borosilicate glass, as observed in Fig. 8.3 must be due to the difference in glass composition. Indeed, it has been shown that the presence of boron affects the stability and the density of ion irradiation-induced defects in silica glass.^{8,16}

8.5 Conclusions

Borosilicate glass as well as thermally grown SiO_2 films show characteristic transients in their in-plane stress upon termination of ion irradiation, that are ascribed to the annihilation of volume-occupying defects. From the stress relaxation kinetics, studied over a broad temperature range, the defect annihilation activation energy spectra are determined for the two glasses. The spectrum for silica shows a decreasing trend with energy, universal for all irradiation temperatures in the range 95-255 K, independent of ion energy and flux, and vanishes above ~ 0.8 eV. In contrast, the spectrum for alkali-borosilicate glass is strongly temperature dependent and increases with energy over the range that is probed.

The distinctly different characteristics are attributed to different defect generation mechanisms, as is supported by an observed difference in the radiation-induced viscosity with temperature. The silica data are consistent with a thermal spike model, while the results for borosilicate glass may be explained by a binary collision model with temperature-dependent defect annihilation.

References

- ¹ R. A. B. Devine, Nucl Instrum. Methods Phys. Res. B **91**, 378 (1994)
- ² E. Snoeks, T. Weber, A. Cacciato, and A. Polman, J. Appl. Phys **78**, 4723 (1995)
- ³ M. L. Brongersma, E. Snoeks, and A. Polman, Appl. Phys. Lett. **71** (12), 1628 (1997)
- ⁴ T. van Dillen, A. Polman, W. Fukarek, and A. van Blaaderen, Appl. Phys. Lett. **78**, 910 (2001)
- ⁵ A. Benyagoub, S. Löffler, M. Rammensee, S. Klaumünzer, and G. Saemann-Ischenko, Nucl. Instrum. Methods Phys. Res. B **65**, 228 (1992)
- ⁶ S. Klaumünzer, Radiat. Eff. Def. in Sol. **110**, 79 (1989)
- ⁷ E. Snoeks, A. Polman, and C. A. Volkert, Appl. Phys. Lett. **65**, 2487 (1994)
- ⁸ D. L. Griscom, G. H. Sigel, Jr., and R. J. Ginther, J. Appl. Phys. **47**, 960 (1976)
- ⁹ M. L. Brongersma, E. Snoeks, T. van Dillen, and A. Polman, J. Appl. Phys. **88**, 59 (2000)
- ¹⁰ C. A. Volkert, J. Appl. Phys. **70**, 3521 (1991)
- ¹¹ Some stress measurements (at certain temperatures between 95 and 580 K) were performed on the same sample using a procedure consisting of: stabilizing the temperature, ion irradiation to equilibrium stress and measuring the stress after switching off the ion beam.
- ¹² M. R. J. Gibbs, J. E. Evetts, and J. A. Leake, J. Mat. Science **18**, 278 (1983)
- ¹³ W. Primak, Phys. Rev. **100**, 1677 (1955)
- ¹⁴ G. H. Vineyard, Rad. Eff. **29**, 245 (1976)
- ¹⁵ T. van Dillen, Masters Thesis, Utrecht University (FOM-Institute for Atomic and Molecular Physics, Amsterdam, 1999)
- ¹⁶ E. Snoeks, P. G. Kik, and A. Polman, Optical Materials **5**, 159 (1996)

9 *Applications of shape-anisotropic colloidal particles and aggregates*

The ion-beam deformation technique can be used to modify the shape of nano- and micrometer-sized colloidal composite materials. We show five different applications. Particles can be brought in suspension for studies on self-assembly and phase behaviour. The hole size of two-dimensional colloidal crystals that serve as mask for nanolithography is tuned by ion irradiation. We demonstrate the fabrication of three-dimensional colloidal photonic crystals of shape-anisotropic particles. Prolate silica ellipsoids can be obtained after two subsequent, mutually orthogonal ion irradiations to equal fluences, and spherical Au particles embedded in a silica matrix can be turned into nanorods by MeV ion irradiation.

9.1 Introduction

In the Chapters 2-4 we have shown in detail how ion irradiation can be used to change the shape of single colloidal silica particles in a well-controlled way. In this chapter we present several applications of shape-anisotropic colloids and composite materials of which the shape is modified by ion irradiation.

9.2 Anisotropic colloidal particles in solution

Colloidal particles play an important role in studies of self-assembly and phase behavior. The synthesis of colloidal model suspensions is well explored and understood for a wide variety of inorganic materials. However, most of the model systems with a narrow size distribution consist of spherical particles. It appears very difficult to synthesize nonspherical particles such as oblate and prolate ellipsoids with low polydispersity. With the work in this thesis we now provide a new technique by which highly anisotropic monodisperse ellipsoidal colloids can be made with adjustable aspect ratio.

For studies of self-assembly and phase behavior, colloidal particles must be brought in suspension. We have shown that, by using ultrasonic treatment, ion irradiated colloidal particles can be removed from the substrate. A stable suspension of deformed silica particles in solution was obtained and light scattering confirmed that the spheroids were redispersed as single entities. Preliminary self-assembly experiments have been performed and showed indications of the formation of nematic colloidal liquid crystalline phase of ion beam deformed oblate colloids.¹

The typical particle yield in our experiments is on the order of 3×10^8 colloids (0.3 mg) per hour (4 MeV Xe⁴⁺, 40 nA/cm², 90 K, area ~ 6 cm²). This assumes an areal density of 10^8 colloids per cm², which can be achieved using a properly patterned template. Using high-energy, high-throughput and high-current ion irradiation systems the yield may be improved by 1–2 orders of magnitude. Indeed, quantities in the order of milligrams are valuable for a wide variety of model experiments in e.g. self-assembly, phase-behavior, or to study optical properties.

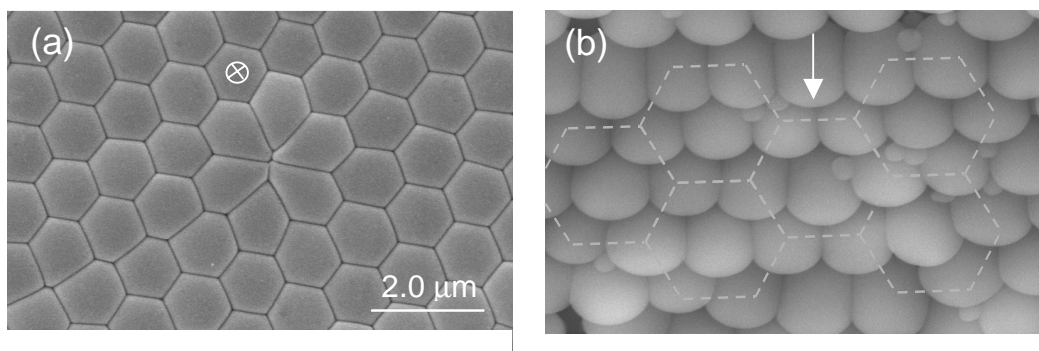


Figure 9.1 SEM images of a hexagonally close-packed monolayer of 1030 nm diameter silica particles after irradiation. **(a)** After irradiation under normal incidence using 4 MeV Xe^{4+} ions to a fluence of $7.5 \times 10^{14}/\text{cm}^2$. The remnants of a dislocation in the original structure, terminated by a vacancy, are clearly seen. **(b)** After irradiation under 45° off the surface normal (at an azimuth indicated by the arrow) to a fluence of $3 \times 10^{14} \text{ Xe}/\text{cm}^2$. The dashed lines indicate the original hexagonal arrangement. Both **(a)** and **(b)** are imaged normal to the surface, and both irradiations are performed at 90 K

9.3 Modification of two-dimensional colloidal crystals, nanolithography

Two-dimensional ordered structures of colloidal particles show dramatic shape changes upon irradiation. A hexagonally close-packed structure of 1030 nm-diameter spherical silica colloids on a silicon substrate was irradiated with 4 MeV Xe^{4+} ions at normal incidence to a fluence of $7.5 \times 10^{14} \text{ cm}^{-2}$ at 90 K. Fig. 9.1(a) shows a scanning electron microscopy (SEM) image after irradiation. As can be seen, the particles that were originally spherical have deformed quite strongly and fill completely the empty space between particles. Even a vacancy, that was present in the original unirradiated structure and that terminated a dislocation coming in from the lower left, is completely filled up as a result of the deformation. The structure in Fig. 9.1(a) is completely different to what would be observed if the colloids had been deformed by purely thermal treatment.²

Figure 9.1(b) shows a hexagonally packed monolayer of silica particles irradiated at an angle of 45° to a fluence of $3 \times 10^{14} \text{ Xe}/\text{cm}^2$. As can be seen in the SEM image, taken normal to the surface, this results in a structure of partially overlapping rows of particles, reminiscent of shingles or roof tiles. The anisotropy is caused by the fact that due to the sample tilt during irradiation the particles were free to expand in one direction perpendicular to the ion beam, but constrained in the other direction due to the presence of neighboring particles.

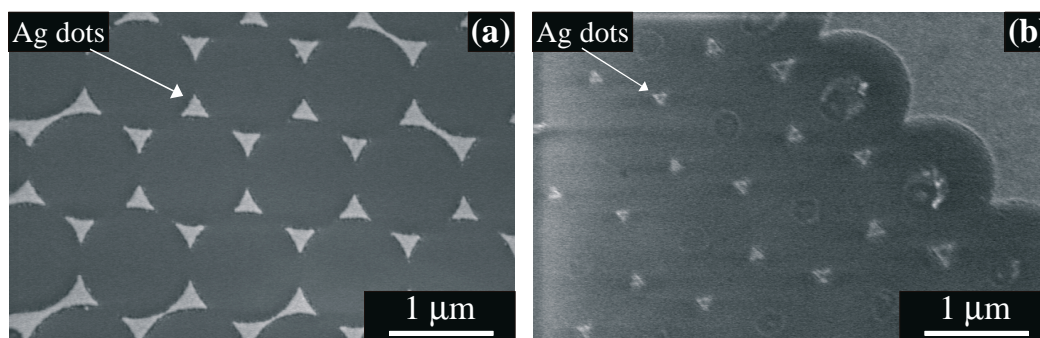


Figure 9.2 Ag patterns (thickness 30 nm) on a glass substrate made by deposition (thermal evaporation) through a self-assembled colloidal mask that was (a) unirradiated, or (b) deformed with 4 MeV Xe ions at 90 K to a fluence of $6 \times 10^{14} \text{ cm}^{-2}$ at normal incidence. The images were taken at normal incidence, after removal of the colloids. In the images the bright spots are the Ag features on the substrate.

Such anisotropic colloidal films are expected to show highly anisotropic optical properties.

The deformation of regular colloidal structures can also be used to tailor the shape of microspheroids comprising a self-assembled lithographic mask for thin-film deposition.^{3,4} In this way the lattice spacing and shape of the voids in between the spheres can be uncoupled. As an example of this effect we show in Fig. 9.2 SEM images of hexagonal patterns of 30 nm thick Ag dots formed by thermal evaporation through a close-packed hexagonal arrangement of 1.0 μm diameter silica colloids placed on glass substrate (a). The image was taken after removal of the colloidal mask by ultrasonic treatment for 1 minute. Figure 9.2(b) shows an image taken after evaporation through a colloidal mask that was first irradiated under normal incidence with 4 MeV Xe ions to a fluence of $6 \times 10^{14} \text{ cm}^{-2}$ at 90 K. This experiment clearly shows a major reduction in feature size of the Ag dots using the deformed colloidal mask: the feature size has decreased from $234 \pm 15 \text{ nm}$ [Fig. 9.2(a)] to $125 \pm 15 \text{ nm}$ [Fig. 9.2(b)]. By controlling the ion fluence the hole size of the colloidal mask can be continuously tuned, and feature sizes below 50 nm have been demonstrated.⁵ Such small feature sizes are difficult to achieve with other techniques.

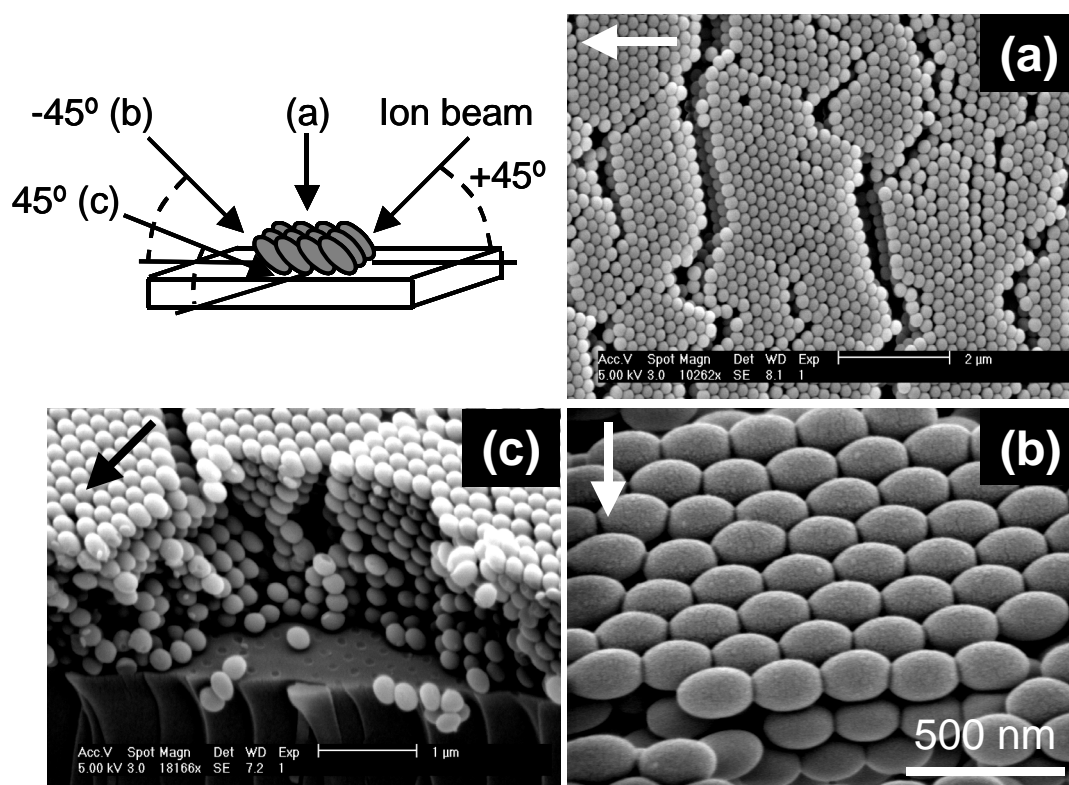


Figure 9.3 SEM images of a planar photonic crystal of close-packed SiO_2 oblate ellipsoids obtained after irradiation with 4 MeV Xe^{4+} ions to a fluence of $1.0 \times 10^{15} \text{ cm}^{-2}$ at an angle of 45° at 90K. (a) Top view of the crystal showing the (111)-crystal plane. (b) Image of the irradiated crystal taken perpendicular to the ion beam direction. The average semi-axes of the ellipsoids determined from the SEM image are $x = 123 \pm 5 \text{ nm}$ and $y = 74 \pm 2 \text{ nm}$. (c) Side-view image (45° tilt) of a broken crystal showing the depth of the deformation caused by the irradiation. The arrows show the direction of the ion beam.

9.4 Photonic crystals of shape-anisotropic colloidal silica particles

A photonic crystal is a regular arrangement of a dielectric material that interacts strongly with light. It offers a unique way to control the propagation and emission of light. Optical bandstructure calculations show that, for a given particle asymmetry, photonic crystals composed of spheroids can have larger bandgaps than those composed of spheres.⁶

Colloidal photonic crystals were fabricated from monodisperse 220 nm diameter SiO_2 colloids (relative polydispersity $\pm 3\%$), synthesized using a microemulsion method followed by seeded growth.⁷ Thin colloidal crystals of 8–10 layers thick were grown on clean glass substrates using a controlled drying

method^{3,8,9} and then annealed at 600°C for four hours in air.² Next the crystals were irradiated with 4 MeV Xe⁴⁺ ions to a fluence of 1.0×10^{15} cm⁻² at 90 K with the sample surface held at an angle of 45° with respect to the direction of the ion beam. Samples were coated with a 5 nm Pt/Pd layer before analyzing by SEM at 5 kV.

Figure 9.3(a-c) shows SEM micrographs of a thin planar crystal of close-packed monodisperse silica colloidal particles after ion irradiation. The different viewing directions are drawn in the schematic inset. After irradiation all particles were deformed and turned into (almost) oblate ellipsoids as is best seen in Fig. 9.3(b). The particles expanded relatively undisturbed in the plane perpendicular to the ion beam direction. When the sample is imaged at -45° [Fig. 9.3(b)] both ellipsoidal semi-axes (x , y) can be measured directly. We find $x=123 \pm 5$ nm and $y=74 \pm 2$ nm (aspect ratio 1.65 ± 0.09) by image processing of the SEM micrographs. From these values it follows that the particle volume has decreased by 16 %, which is ascribed to the shrinkage of the silica colloids upon thermal annealing. Similar volume changes upon thermal annealing have been observed in Ref. 2. Due to this shrinkage and the attachment of the crystal to the substrate randomly oriented cracks appear after the thermal anneal of the crystal. No cracks were observed in annealed and irradiated *free-standing* colloidal crystalline films.

From the side view [Fig. 9.3(c)], one can see that the anisotropic deformation is extended throughout the full crystal including the layer of particles in contact with the substrate. However, particles close to the substrate are less deformed since the crystal thickness (~ 1.8 μm) is close to the penetration depth of the 4 MeV Xe⁴⁺ ions, taking the angle of irradiation and the filling fraction of SiO₂ into account. Higher energies could be used to deform thicker crystals more uniformly. From Fig. 9.3(c), it is apparent that there is a deviation from the ellipsoidal shape caused by the fact that deforming spheres were touching in the crystal. Most likely, this increases the packing fraction and consequently the effective refractive index of the composite.

Optical transmission spectra on these thin photonic crystals were taken along the (111) direction (normal incidence).¹⁰ The spectra before and after the ion irradiation exhibit a minimum in the optical transmission, where the Bragg condition is fulfilled and light is diffracted away from the axis of propagation. The presence of a Bragg peak after irradiation indicates that the crystal structure remains after the ion irradiation. However, the Bragg minimum, corresponding to the stop gap, that occurs at a wavelength of 453 nm before irradiation shifts to 424 nm after irradiation. This shift is ascribed to the combined effect of changes in the crystal symmetry (lattice spacing) and particle form factor due to the ion irradiation, and possibly a small crystal densification. These measurements clearly demonstrate that the optical properties of three-dimensional photonic structures can be modified in a controllable way using ion irradiation.

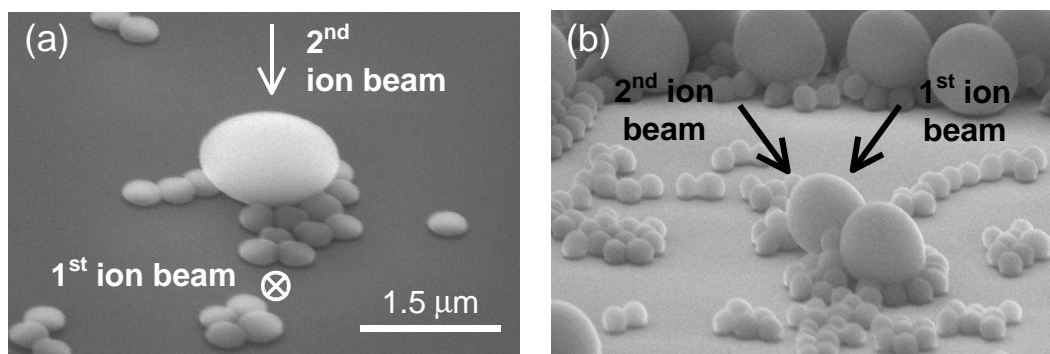


Figure 9.4 Prolate ellipsoids: SEM images of silica particles such as shown in Fig. 2.1(a)-(d), after an additional 4 MeV Xe⁴⁺ ion irradiation to a fluence of 3×10^{14} cm⁻² at an angle orthogonal to the first irradiation. (a), View along the direction of the first ion irradiation (+45° tilt). (b), Side view almost perpendicular to both ion beams [same orientation as in Fig. 2.1(d)].

9.5 Prolate silica colloids by multiple ion irradiation

As an illustration of the reproducibility and versatility of the ion irradiation technique, we demonstrate that anisotropic deformation can also be used for the synthesis of prolate ellipsoids. First, oblate particles were made from originally 1030-nm-diameter silica spheres by 4 MeV Xe⁴⁺ irradiation to a fluence of 3×10^{14} cm⁻² at an angle of +45°, similar to what is shown in Figs. 2.1(b-d). Next, the particles were again irradiated with 4 MeV Xe⁴⁺ ions to a fluence of 3×10^{14} cm⁻², now with the sample tilted at -45°, i.e. orthogonal to the direction of the first irradiation.

Figure 9.4 shows SEM images of these doubly irradiated particles. In the image of Fig. 9.4(a), taken using the same sample orientation as in Fig. 2.1(b), the particles appear elliptical. The same is found in SEM images taken at other sample tilt angles within the plane expanded by the two ion beam directions. Figure 9.4(b) shows a side-view image [15° tilt angle, as in Fig. 2.1(d)] that is almost normal to both of the two ion beam directions. From this angle of view the particle projection is close to circular. Therefore, it can be concluded that the ellipsoids in Fig. 9.4 have a prolate shape. The total ion fluence used to form these prolate ellipsoids was 6×10^{14} cm⁻², and the major and minor diameters of the particles are included in Fig. 2.2 (triangles). The measured transverse diameter L of the prolate ellipsoids (open triangle) agrees well with the calculated curve of L (dotted line) for ellipsoidal particles after a single irradiation to the same *total* ion fluence.¹¹ This experiment demonstrates that a high level of shape control can be achieved. In general, repeated ion irradiations

from different directions can be used to create ellipsoidal particles with variable ratios between the three principal diameters.¹²

9.6 Aligned gold nanorods in silica made by ion irradiation of core-shell colloidal particles

Core-shell colloidal particles composed of a 14 nm-diameter Au core surrounded by a 72 nm-thick SiO₂ shell, were prepared in solution using a method described elsewhere.¹³ A few drops of a diluted solution were dispersed on a 10 nm-thick Si₃N₄ membrane which allowed transmission electron microscopy (TEM) of individual particles. The particles were irradiated with 30 MeV Cu or Se ions to fluences in the range $(2-4)\times 10^{14}$ ions/cm². During irradiation the samples were clamped to a liquid-nitrogen cooled Cu block. Some irradiations were done at normal incidence, others with the ion beam 20° or 45° tilted away from the normal. 6 MV tandem accelerators in Rossendorf and Montreal provided the ion beams. Following irradiation the colloids were examined by SEM (5 keV electron beam), TEM (200 keV electron beam), and optical transmission measurements.

Figure 9.5(a) shows a TEM image of an Au-silica core-shell particle before irradiation. It is spherically shaped, with the 14 nm-diameter Au core centred inside. Fig. 9.5(b) shows a TEM image after 30 MeV Se irradiation at a fluence of 2×10^{14} cm⁻², with the ion beam 45° off-normal. The image was taken along the normal, and the arrow in Fig. 9.5(b) indicates the ion beam direction projected onto the surface. Clearly, after irradiation, neither the silica shell nor the Au core is spherically shaped. The deformation of the silica shell is consistent with the anisotropic deformation described in the previous chapters, i.e. formation of an oblate particle, with the minor axis parallel and two major axes perpendicular to the ion beam. The relative expansion of the longitudinal (major) axis is ~20 %.

Figure 9.5(b) also shows that the Au core has deformed, but in an entirely different manner: a major axis is observed along the ion beam and a minor axis perpendicular to the beam. The initially 14 nm-diameter Au core has deformed into a rod with apparent dimensions of 6 by 38 nm. Correcting for the 45° projection of the TEM image relative to the ion beam direction, the major axis is as large as 54 nm (size aspect ratio ~9). Assuming cylindrical symmetry, we can derive from the TEM image that the volume of the Au particle does not change during the deformation, within an error bar of $\pm 20\%$.

Reference measurements were also performed, in which 14 nm-diameter Au colloids, not surrounded by a silica shell, were irradiated with 30 MeV Se ions, and no deformation was observed. These data indicate that the deformation of the Au core is related to an effect imposed by the silica shell.

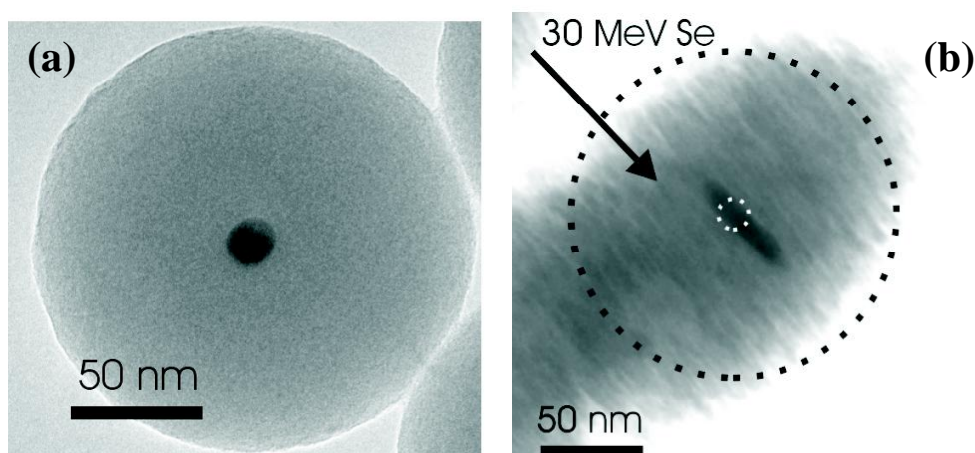


Figure 9.5 TEM images of core-shell colloids composed of a 14 nm-diameter Au core surrounded by a 72 nm-thick silica shell. (a) before irradiation, (b) after 30 MeV Se ion irradiation at an angle of 45° at a fluence of $2 \times 10^{14} \text{ cm}^{-2}$. The ion beam direction projected onto the surface is indicated by an arrow. The original spherical perimeter is indicated by the dashed circle.

To study this in more detail, a series of core-shell particles was made with different silica shell thicknesses (and identical Au cores) in the range 15–72 nm. No measurable deformation of the Au core was observed for silica shells thinner than 26 nm. A second additional observation, of similar nature, is that for core-shell particles of equal size and shell thickness, the deformation of the metal core depends on the local surroundings of the particles: particles that are stacked two or three layers thick and are in contact before irradiation exhibit significantly larger deformation of the metal core than isolated particles. From these two independent experiments (varying shell thickness and varying colloid contact) we conclude that the Au core deforms more efficiently as more silica surrounds it.

To explain the shape change of the Au core due to the presence of the silica shell we propose the following indirect deformation scenario. Each individual ion impact in silica leads to the formation of a thermal spike bringing about an in-plane viscous strain perpendicular to the ion beam, as described in Chapter 5. In the core-shell colloids the lateral stress fields surrounding each individual ion track in silica act on the Au core. Metals are known to be relatively soft under ion irradiation, as evidenced e.g. from the low ion irradiation-induced viscosity.¹⁴ Thus, with an in-plane stress acting on the soft core, it may flow in the out-of-plane direction, i.e. along the direction of the ion beam.

Preliminary optical extinction measurements presented in Ref. 15 show that aligned anisotropic Au nanorods made by high-energy ion irradiation have shifted surface plasmon absorption resonances with respect to isotropically

shaped Au nanoparticles. The ‘*indirect*’ ion beam deformation technique can therefore be used to change the optical properties of metal nanoparticles.

9.7 Conclusions

We demonstrated several applications of ion-beam induced anisotropic deformation in colloidal systems:

1. Ion beam-deformed colloidal particles can be brought in suspension for studies of self-assembly. Typical quantities that can be formed are mg/hr.
2. By MeV ion irradiation-induced deformation of self-assembled two-dimensional colloidal crystals used as masks for thin film deposition, the size of the deposited features can be precisely tuned.
3. Colloidal photonic crystals of shape-anisotropic particles were made using MeV ion irradiation. Both the lattice structure and form factor were changed in a controlled way, resulting in modified optical properties of the colloidal crystal.
4. By using multiple ion irradiations different ellipsoidal particle shapes can be produced. As an illustration, we made prolate-shaped particles by using two subsequent, mutually orthogonal ion irradiations to equal fluences.
5. MeV ion irradiation of colloidal silica particles containing an Au core leads to a deformation of the shell into an oblate ellipsoid and of the Au core into a nanorod. The Au deformation is attributed to the in-plane mechanical stress in the silica shell acting on the radiation-softened Au core. Size aspect ratios as large as 9 were observed for the Au rods.

References

- ¹ E. Snoeks, A. van Blaaderen, T. van Dillen, C. M. van Kats, M. L. Brongersma, and A. Polman, *Adv. Mater.* **12**, 1511 (2000)
- ² H. Miguez, F. Meseguer, C. Lopez, A. Blanco, J. S. Moya, J. Requena, A. Mifsud, and V. Fornes, *Adv. Mater.* **10**, 480 (1998)
- ³ N. D. Denkov, O. D. Velev, P. A. Kralchevsky, I. B. Ivanov, H. Yoshimura, and K. Nagayama, *Langmuir* **8**, 3183 (1992)
- ⁴ F. Burmeister, C. Schäfle, T. Matthes, M. Böhmisch, J. Boneberg, and P. Leiderer, *Langmuir* **13**, 2983 (1997)
- ⁵ D. L. J. Vossen, D. Fific, J. J. Penninkhof, T. van Dillen, A. Polman, and A. van Blaaderen, to be published
- ⁶ J. W. Haus, H. S. Sözüer, and R. J. Inguva, *J. Mod. Opt.* **39**, 1991 (1992)
- ⁷ K. Osseosare and F. J. Arriagada, *Colloids Surface* **50**, 321 (1990)
- ⁸ P. Jiang, J. F. Bertone, K. S. Hwang, and V. L. Colvin, *Chem. Mater.* **11**, 2132 (1999)

- ⁹ K. P. Velikov, A. Moroz, and A. van Blaaderen, *Appl. Phys. Lett.* **80**, 49 (2002)
- ¹⁰ K. P. Velikov, T. van Dillen, A. Polman, and A. van Blaaderen, *Appl. Phys. Lett.* **81**, 838 (2002)
- ¹¹ The calculation was performed using L from Eq. (2.3), $2R=1029$ nm and the deformation strain rate $A=6.0\times 10^{-16}$ cm²/ion for silica colloids under 4 MeV Xe ion irradiation at 90 K as found in Chapter 2.
- ¹² S. Klaumünzer, *Nucl. Instrum. Methods Phys. Res. B* **215**, 345 (2004)
- ¹³ L. M. Liz-Marzan, M. Giersig, and P. Mulvaney, *Langmuir* **12**, 4329 (1996);
C. Graf, D. L. Vossen, A. Imhof, and A. van Blaaderen, *Langmuir* **19**, 6693 (2003)
- ¹⁴ E. Snoeks, K. S. Boutros, and J. Barone, *Appl. Phys. Lett.* **71**, 267 (1997).
- ¹⁵ S. Roorda, T. van Dillen, A. Polman, C. Graf, A. van Blaaderen, and B. Kooi, *Adv. Mater.* **16**, 235 (2004)

Summary

When an amorphous microstructure is subjected to an ion beam of high enough energy, an anisotropic plastic shape transformation can take place that is the result of the thermal spike around the ion tracks. This thesis presents a detailed investigation of this ion irradiation-induced anisotropic plastic deformation phenomenon in a wide range of materials and under a range of conditions. It provides understanding of its fundamental origin and provides a range of applications of ion beam-deformed microstructures.

In Chapter 2 we show that colloidal silica particles with a diameter of 1 μm change their shape from spherical to oblate ellipsoidal under 4 MeV Xe ion irradiation: the particles expand in the plane perpendicular to the ion beam and contract in the direction of the ion beam, while remaining their volume. The size aspect ratio (major over minor diameter) of the colloids can be accurately tuned by varying the ion fluence and size ratios up to 5 are achieved. During off-normal irradiation the colloids perform a gradual angular “roll-off” with respect to the incident ion beam: after irradiation at an angle of 45° to a fluence of $1 \times 10^{15} \text{ cm}^{-2}$ the minor axis has rotated by 17° . The particles have thus transformed into ellipsoidal particles with three different principal diameters. The fluence dependence of principal axes and roll-over angle are well described by a macroscopic phenomenological model for anisotropic deformation derived by Klaumünzer. For 4 MeV Xe the typical deformation perpendicular to the ion beam is 6% for each unit fluence of $1 \times 10^{14} \text{ cm}^{-2}$.

In Chapter 3 it is shown that the size polydispersity of a silica colloid distribution is unaffected by the ion irradiation. The transverse diameter perpendicular to the ion beam grows exponentially with ion fluence. From ion energy-dependent measurements using 4-16 MeV Au ions, it follows that the deformation rate increases with electronic stopping. Nonellipsoidal shapes can be obtained in case the mean projected ion range is smaller than the colloid diameter. Ion beam-induced anisotropic deformation is also observed for amorphized micro-crystalline ZnS and amorphous TiO_2 particles, as well as for composite ZnS/ SiO_2 and SiO_2 /Au core/shell particles. No deformation is observed for single-crystalline Al_2O_3 particles and micro-crystalline Ag particles.

Chapter 4 focuses on anisotropic deformation for Xe ion energies between 300 keV and 4 MeV: a strong effect still occurs at ion energies as low as 300 keV, underlining the importance of this effect at commonly used ion irradiation energies. We find that the deformation strain rate increases with electronic stopping without indication of a threshold. It is also found that the deformation rate decreases with increasing irradiation substrate temperature.

The data presented in Chapters 2-4 provide strong evidence for a viscoelastic thermal spike model for anisotropic deformation that we develop in Chapter 5. In this model the deformation process is attributed to time-dependent viscous flow in single ion tracks. Deviatoric stresses brought about by the rapid thermal expansion of heated ion track cylinders relax by subsequent Newtonian viscous flow for ion track temperatures exceeding a certain flow temperature. The stress relaxation is accompanied by viscous expansion perpendicular to the ion track and an associated contraction along the direction of the ion track. Upon rapid cooling of the ion track cylinder, these strains freeze in, leading to a net deformation. From our model it also follows that ion tracks close to the sample's edge should exhibit reduced viscous flow compared to ion tracks located far away from the edge. The macroscopic deformation is then found by superposing the deformations resulting from independent ion tracks randomly distributed over the sample surface. The model shows excellent qualitative agreement with experimental data in Chapters 2-4.

In Chapter 6 we concentrate on the deformation of silicon pillars under 30 MeV Cu irradiation. We find that amorphous silicon pillars anisotropically deform at a transverse strain rate that is one order of magnitude smaller than that of silica under similar irradiation conditions. No deformation was found for crystalline Si(100) pillars. The latter is attributed to the lack of regions with local free volume required for the shear stress relaxation leading to the deformation. The small amount of free volume, the relatively high irradiation-induced viscosity or the fact that Si contracts upon melting are possible explanations for the relatively low deformation strain rate for amorphous Si. Irradiation of partially amorphized Si pillars with 30 MeV Cu ions demonstrates that deformation can be used to generate a variety of microstructures.

In case the irradiated material is constrained on a substrate, dimensional changes resulting from ion irradiation-induced effects lead to the build-up of an in-plane compressive or tensile stress. The in-plane stress results in a wafer bending that can be accurately measured using a sensitive scanning laser wafer curvature technique. This technique allows us to *in-situ* determine the integrated stress in an irradiated film and to investigate phenomena that are accompanied by dimensional changes smaller than 1%. In Chapter 7 we study the dynamic competition between three irradiation-induced phenomena in vitreous silica: tensile stress generation due to densification by structural transformation, stress relaxation by Newtonian viscous flow, and creation of compressive stress by anisotropic strain generation. Each of these processes strongly depends on either electronic or nuclear stopping. We demonstrate that due to the strong depth-dependence of both stopping processes, the in-plane stress, resulting from the interplay between the three irradiation-induced processes, is also highly depth-dependent and shows large variations over depth, ranging between compressive and tensile. We introduced the concept of a *stress map* for ion irradiation that

predicts the high-fluence saturation stress of a constrained silica film under any irradiation condition with ion energies up to several MeV.

Time-resolved stress measurements presented in Chapter 8 show that after 2 and 4 MeV Xe ion irradiation of both alkali-borosilicate glass and thermally grown SiO₂ films the in-plane stress changes towards tensile values. We attribute this phenomenon to a fourth irradiation-induced effect, namely the generation and subsequent annihilation of volume-occupying defects that have a distribution of activation energies. We derive the activation energy spectra of these defects. For alkali-borosilicate glass defects are observed with strongly temperature dependent annihilation energies, whereas for thermal silica a temperature independent spectrum is found that vanishes for activation energies higher than 0.8 eV. The difference is attributed to differences in the nature of defect generation in the two types of glass.

Finally, in Chapter 9, we report on several applications of shape-anisotropic particles and aggregates fabricated using the ion irradiation technique. Colloidal particles can be removed from the substrate after ion irradiation and brought in solution, so that studies of self-assembly and phase behaviour of monodisperse highly anisotropic colloids become possible. We show that the hole size of two-dimensional colloidal crystals that serve as mask for thin film deposition can be tuned by ion irradiation, resulting in deposited features of reduced size. We demonstrate the fabrication of three-dimensional colloidal photonic crystals of almost ellipsoidal particles that show modified optical properties as a result of a change in crystal lattice structure and particle form factor. We show that prolate ellipsoidal silica particles can be made by using two mutually orthogonal ion irradiations to equal fluences, and finally, we show that spherical Au nanoparticles surrounded by a silica matrix transform into nanorods upon 30 MeV Cu ion irradiation.

In summary, the experimental results on ion beam-induced anisotropic plastic deformation of colloidal particles and their good agreement with the developed theoretical model provide a nearly complete picture of the origin and characteristics of the deformation phenomenon. We have also demonstrated that the ion irradiation-induced deformation technique can be used to fabricate unique microstructures that find applications in a range of scientific fields.

Samenvatting

Als een amorfe microstructuur wordt bestraald met ionen van voldoende hoge energie, kan er een anisotrope plastische vormverandering optreden ten gevolge van de hoge temperatuur in smalle zones rondom de ionenbanen door het materiaal. Dit proefschrift beschrijft een gedetailleerd onderzoek naar anisotrope plastische deformatie van een veelheid van materialen onder verschillende bestralingscondities. Het geeft fundamenteel inzicht in de oorsprong van het proces en laat verschillende toepassingen zien van microstructuren die zijn gedeformeerd met ionenbundels.

In hoofdstuk 2 laten we zien dat colloïdale silica deeltjes met een diameter van 1 μm onder bestraling met 4 MeV Xe ionen een vormverandering ondergaan van bolvormig naar oblaat ellipsoïdaal: loodrecht op de ionenbundel zetten de deeltjes uit, evenwijdig aan de bundel krimpen ze. Daarbij verandert hun volume niet. De verhouding van de lange en de korte diameter van de colloïden kan nauwkeurig worden ingesteld door het variëren van de ionendosis. Verhoudingen ter grootte van 5 worden bereikt.

Gedurende niet-loodrechte bestraling ondergaan colloïden op een vlak substraat een “roll-off” ten opzichte van de ionenbundel: na bestraling tot een dosis van $1 \times 10^{15} \text{ cm}^{-2}$ onder een hoek van 45° met de normaal van het substraat is de hoek van de korte as met de ionenbundel toegenomen tot 17° . De deeltjes hebben een ellipsoïdale vorm gekregen met 3 hoofdassen van verschillende lengte. De dosisafhankelijkheid van deze diameters en de “roll-off”-hoek kunnen goed worden beschreven met een fenomenologisch model dat is ontwikkeld door Klaumünzer. Voor 4 MeV Xe is de typische uitzetting loodrecht op de ionenbundel 6 % per eenheidsdosis van $1 \times 10^{14} \text{ cm}^{-2}$.

In hoofdstuk 3 laten we zien dat de spreiding in deeltjesgrootte van silica colloïden niet wordt beïnvloed door ionenbestraling. De transversale diameter loodrecht op de ionenbundel groeit exponentieel met de ionendosis. Uit bestralingen met Au ionen met energieën tussen 4 en 16 MeV blijkt dat de deformatiesnelheid toeneemt met het energieverlies van de ionen aan het bestraalde materiaal als gevolg van elektronische excitaties. Niet-ellipsoïdale deeltjes worden verkregen indien het gemiddelde geprojecteerde bereik van de ionen kleiner is dan de diameter van de colloïden. Anisotrope deformatie treedt ook op bij bestraling van geamorfiseerde microkristallijne ZnS en amorfe TiO_2 deeltjes, evenals bij ZnS/SiO_2 en SiO_2/Au kern/schil-deeltjes. Geen deformatie is waargenomen na bestraling van monokristallijne Al_2O_3 en microkristallijne Ag deeltjes.

Hoofdstuk 4 behandelt anisotrope deformatie onder Xe ionenbestraling met energieën tussen 300 keV en 4 MeV. Zelfs bij 300 keV treedt nog

aanzienlijke deformatie op. Dit onderstreept het belang van het de deformatie-effect bij gangbare energieën. Uit de resultaten volgt dat de deformatiesnelheid toeneemt met het elektronische energieverlies. Een drempelwaarde voor dit energieverlies waaronder geen deformatie zou optreden, wordt niet gevonden. Tevens blijkt dat de deformatiesnelheid afneemt met toenemende substraattemperatuur.

De data gepresenteerd in hoofdstukken 2-4 passen binnen een mesoscopisch, viskoelastisch model voor anisotrope deformatie dat in hoofdstuk 5 wordt ontwikkeld. In dit model vindt het deformatieproces zijn oorsprong in tijdsafhankelijke viskeuze vervloeiing in de smalle zone rondom de baan van een ion in het bestraalde materiaal. Deviatorische spanningen, veroorzaakt door de snelle thermische uitzetting van deze hete, cilindrische zone, relaxeren als gevolg van Newtoniaanse viskeuze vervloeiing bij temperaturen boven een zekere 'vloei temperatuur'. Deze spanningsrelaxatie gaat gepaard met een viskeuze uitzetting van de hete zone loodrecht op de baan van het ion en een krimp langs de baan van het ion. Tijdens snelle afkoeling vriezen deze viskeuze rekken in, hetgeen leidt tot een netto deformatie van de zone. Uit ons model volgt tevens dat de viskeuze vervloeiing af zou moeten nemen naarmate de ionencilinder dichter bij de rand van het substraat ligt. De macroscopische deformatie is vervolgens het collectieve resultaat van individuele, onafhankelijke ioneninslagen, willekeurig verdeeld over het oppervlak van het bestraalde materiaal.

In hoofdstuk 6 behandelen we het deformatiegedrag van silicium paaltjes met afmetingen van enkele μm , onder bestraling met 30 MeV Cu ionen. Waargenomen wordt dat amorfe silicium paaltjes anisotroop deformereren met een transversale reksnelheid die een orde van grootte kleiner is dan die van silica onder gelijke bestralingscondities. Kristallijne Si(100) paaltjes daarentegen blijken niet te deformereren, hetgeen wordt toegeschreven aan het ontbreken van gebieden met lokaal vrij volume, waardoor spanningsrelaxatie niet kan optreden. De lage deformatiesnelheid van amorf Si is mogelijk het gevolg van het geringe vrije volume, de relatief hoge viscositeit onder ionenbestraling of het anomale smeltgedrag van Si. Bestraling van gedeeltelijk geamorfiseerde Si paaltjes met 30 MeV Cu ionen laat zien dat deze deformatietechniek kan worden gebruikt voor het maken van unieke microstructuren.

Indien een materiaal niet vrij is te deformereren, maar daarin wordt beperkt door bijvoorbeeld een onderliggend substraat, leiden de bestralingsgeïnduceerde dimensieveranderingen tot de opbouw van druk- of trekspanningen. Voor dunne films op een substraat leidt dit tot een kromming die nauwkeurig kan worden gemeten met een gevoelige laser reflectie techniek. Deze techniek stelt ons in staat de geïntegreerde spanning in de bestraalde film *in-situ* te bepalen en op deze manier processen te bestuderen die dimensieveranderingen veroorzaken kleiner dan 1%. In hoofdstuk 7 bestuderen we de netto spanningsevolutie als gevolg van drie processen in silica onder ionenbestraling: opbouw van

trekspanning als gevolg van verdichting door structuurveranderingen, spanningsrelaxatie door het optreden van Newtoniaanse viskeuze vervloeiing en ontwikkeling van drukspanning als gevolg van anisotrope deformatie. Deze drie processen hangen ieder verschillend af van het elektronische energieverlies of van het directe energieverlies van de ionen door botsingen met de atomen in het bestraalde materiaal (atomaire energieverlies). We tonen aan dat als gevolg van de sterke diepteafhankelijkheid van zowel het elektronische als het atomaire energieverlies van de ionen de spanningen in de bestraalde film ook sterk diepteafhankelijk zijn. We introduceren het concept van een *spanningskaart* voor ionenbestraling, die de hoge-dosis verzadigingsspanning in een gefixeerde silica film voorspelt onder iedere bestralingsconditie met energieën tot enkele MeV.

Tijdsopgeloste spanningsmetingen bij verschillende substraattemperaturen tussen 95 en 580 K in hoofdstuk 8 laten zien dat na 2 en 4 MeV Xe ionenbestraling van zowel alkali-borosilicaatglas als thermisch gegroeide SiO₂ films de spanning langzaam verandert in de richting van trekspanning. We schrijven deze verandering toe aan een vierde, bestralingsgeïnduceerd effect: de generatie en de daaropvolgende annihilatie van volume-innemende defecten die een verdeling aan activeringsenergieën hebben. Uit deze spanningsmetingen bepalen we de activeringsenergiespectra van deze defecten. Voor alkali-borosilicaatglas is het defectenspectrum sterk temperatuurafhankelijk en neemt het toe met activeringsenergie bij iedere temperatuur. Voor thermisch silica daarentegen vinden we een spectrum dat onafhankelijk is van de temperatuur, geleidelijk afneemt met activeringsenergie en verdwijnt voor energieën groter dan 0.8 eV.

Tenslotte laten we in hoofdstuk 9 verschillende toepassingen zien van anisotrope deeltjes en aggregaten die zijn gemaakt met ionenbestraling. Colloïdale deeltjes kunnen van het substraat worden verwijderd en in oplossing worden gebracht, zodat studies naar zelfordening en fasegedrag van monodisperse, sterk anisotrope colloïden mogelijk worden. De gaten in tweedimensionale colloïdale kristallen, die als masker dienen voor de depositie van dunne films, kunnen worden verkleind door ionenbestraling, hetgeen resulteert in gedeponeerde structuren van kleinere afmeting. We laten zien hoe driedimensionale, fotonische kristallen van bijna-ellipsoïdale colloïden kunnen worden gemaakt. Deze kristallen hebben gemodificeerde optische eigenschappen als gevolg van een verandering van de roosterstructuur van het kristal en de vormfactor van de deeltjes. We hebben prolaat-ellipsoïdale silica deeltjes gemaakt door achtereenvolgens twee ionenbestralingen van gelijke dosis uit te voeren, loodrecht op elkaar. Tot slot tonen we aan dat bolvormige Au nanodeeltjes, omgeven door een silica schil, veranderen in staafjes onder 30 MeV Cu bestraling.

Kort samengevat, de experimentele resultaten van de anisotrope plastische deformatie van colloïdale deeltjes onder ionenbestraling en de goede overeenstemming met het ontwikkelde theoretische model geven een bijna

compleet beeld van de oorsprong en de karakteristieken van het deformatieverschijnsel. We hebben ook aangetoond dat deze deformatietechniek kan worden gebruikt voor het maken van unieke microstructuren die kunnen worden toegepast in verscheidene wetenschapsgebieden.

Dankwoord - Acknowledgements

Aan mijn mooie en leerzame periode op Amolf is helaas een einde gekomen. Ik wil daarom nu iedereen bedanken die heeft bijgedragen aan het tot stand komen van dit proefschrift.

Ten eerste wil ik mijn promotor Albert Polman bedanken. Albert, je hebt me de kans gegeven om in jouw groep boeiend onderzoek te doen. Onze interessante en leerzame discussies zijn in dit boekje verwerkt en daar mogen we trots op zijn. Tevens heb ik van je geleerd hoe je een goede presentatie moet geven, hetgeen ik vervolgens op verschillende continenten zelf ten uitvoer mocht brengen.

Tijdens mijn promotieonderzoek was ik ‘gelegerd’ in het “Optoelectronics materials”-kamp. Veel profijt heb ik gehad van de werkbesprekingen en de discussies met mijn groepsleden: Edwin Snoeks, Mark Brongersma, Pieter Kik, Lenneke Slooff, Christof Strohhofer, Jan van der Elsen, Michiel de Dood, Nicholas Hamelin, Jose dos Santos, Jeroen Kalkman, Joan Penninkhof, Hans Mertens, Anna Tchegotareva, Basjan Berkhout, Freek Suyver, Dirk Vossen, Daniel Peters, Michael Hensen en Max Siem. Ik wil in het bijzonder Jan van der Elsen bedanken voor de vele leerzame en interessante discussies. Mark Brongersma en Edwin Snoeks wil ik bedanken voor hun fantastische hulp in het begin van mijn Amolf-tijd. Max Siem bedank ik voor zijn inzet en de vele discussies tijdens zijn afstudeerstage, hetgeen resulteerde in hoofdstuk 7 van dit proefschrift. Sjoerd Roorda en Arjen Vredenberg wil ik bedanken voor de fijne samenwerking. Van onze discussies en gezamenlijke experimenten, die beschreven staan in hoofdstukken 6 en 9, heb ik enorm veel geleerd. Sjoerd, ik zal onze reis naar Dresden nooit vergeten.

Johan Derks en Jan ter Beek wil ik in het bijzonder bedanken voor hun technische hulp en het onderhouden van het “versnellerpark”. Dankzij jullie heb ik altijd goed experimenteel onderzoek kunnen doen. Bedankt Johan voor de steun in de laatste 2 maanden voor het vertrek van de 1 MV versneller en voor de technische hulp met de elektronenmicroscopie. Katrien Keune, Annelies van Loon en Hans Zeijlemaker wil ik bedanken voor hun enthousiasme en hulp met de elektronenmicroscopie. John Geus, bedankt voor je inspirerende begeleiding en samenwerking bij het SEM werk.

Gedurende mijn promotie heb ik veel samengewerkt met de ‘Soft Condensed Matter’ groep van Alfons van Blaaderen (Utrecht). Alfons, dankzij jou heb ik inzicht gekregen in colloïd-chemie en elektronenmicroscopie. Ik ben je zeer erkentelijk voor het beschikbaar stellen van de vele materialen. Tevens heb ik prettig samengewerkt met Carlos van Kats, Krassimir Velikov, Christina Graf, Dirk Vossen en Damir Fific. Dit heeft geresulteerd in een groot aantal artikelen, beschreven in hoofdstuk 9.

Een belangrijk deel van mijn promotietijd heb ik doorgebracht in de “Micromechanica” groep van Erik van der Giessen, eerst in Delft en later in Groningen. Patrick Onck en Erik, bedankt voor de geweldige samenwerking. Jullie hebben me in korte tijd ingewijd in de ‘materiaalkunde’. Zonder jullie intensieve hulp

was hoofdstuk 5 niet tot stand gekomen. Ik heb genoten van onze vruchtbare, leerzame en humorvolle discussies...en van het heerlijke brood in de kantine van de Universiteit Groningen. Ook zal ik onze gesprekken over ‘gegeneraliseerde vliegtuigen’ nooit vergeten. Lucia Nicola en Steffen Brinckmann bedank ik voor hun steun en vriendschap.

Part of the experiments described in Chapters 3, 6 and 9 were performed at the Research Center Rossendorf (Forschungszentrum Rossendorf, Germany). I would like to thank Andreas Kolitsch and Wolfhard Möller for making this possible and Karl-Heinz Heinig for the fruitful discussions. I would also like to thank my direct supervisor there, Wolfgang Fukarek, for his technical and scientific support.

I thank Siegfried Klaumünzer for his help and support. My visit to Berlin, our discussions about anisotropic deformation were very helpful and gave me a lot of insight in the deformation phenomenon.

Via Delft, Groningen en Dresden keer ik toch weer terug naar Amolf om een aantal mensen te bedanken. Ten eerste Michel Kropman, die vier jaar lang mijn kamergenoot was. Michel, bedankt voor de gezellige sfeer, onze wetenschappelijke gesprekken en vooral voor de vriendschap. Ook Joop Gilijamse, mijn kamergenoot gedurende het laatste jaar van mijn promotie, wil ik bedanken. Iliya Cerjak, bedankt voor je hulp bij het maken van de omslag van dit proefschrift. Silvia de Jong en Grace Joseph, bedankt voor al jullie steun bij het versturen van de vele artikelen (er komen er overigens nog twee aan). Ik zal onze gezamenlijke lunch missen. Willem de Jong, Anna Tchebotareva en Michiel de Dood wil ik bedanken voor hun steun en vriendschap. Ik wil iedereen van het ondersteunend personeel op Amolf bedanken voor alles wat ze voor me hebben gedaan. Dankzij jullie kon er heel goed worden gewerkt en, nog belangrijker, was het gezellig op Amolf. Ik zal jullie allemaal missen.

Ik wil mijn familie en in het speciaal mijn ouders, Jos en Marion, en mijn broer, Jaco, bedanken voor hun steun en belangstelling de afgelopen jaren. Zonder jullie was dit alles nooit mogelijk geweest.

Quiero agradecer a mi familia y mis amigos en Chile. Muchas gracias quiero dar a mi hermano Cristian Pereira Valverde y nuestra familia, especialmente Loreto, Laura, Manuel, y Cesar, por su amor, amistad, cariño y todo lo que han hecho por mi estos años. Muchas gracias tambien para mi hermano Marcel Guzman y su familia en Berlin. Desde el fondo de mi corazon, los quiero mucho a todos!

Al final, quiero agradecer a mi novia Judith Alicia y su familia en Peru. Gracias por su amor, amistad y cariño. Judith, gracias por estar a mi lado, te amo mucho.

List of publications

Chapter 2

Colloidal ellipsoids with continuously variable shape

E. Snoeks, A. van Blaaderen, T. van Dillen, C. M. van Kats, M. L. Brongersma, and A. Polman

Adv. Mater. **12**, 1511 (2000)

Angular roll-off during ion beam deformation of colloidal particles

T. van Dillen, S. Klaumünzer, E. Snoeks, A. van Blaaderen, and A. Polman
to be submitted

Chapter 3

Energy-dependent anisotropic deformation of colloidal silica particles under MeV Au irradiation

T. van Dillen, A. Polman, W. Fukarek, and A. van Blaaderen

Appl. Phys. Lett. **78**, 910 (2001)

Anisotropic deformation of colloidal particles under MeV ion irradiation

T. van Dillen, E. Snoeks, W. Fukarek, C. M. van Kats, K. P. Velikov, A. van Blaaderen, and A. Polman

Nucl. Instrum. Methods Phys. Res. B **175-177**, 350 (2001)

Chapter 4

Ion beam-induced anisotropic plastic deformation at 300 keV

T. van Dillen, A. Polman, C. M. van Kats, and A. van Blaaderen

Appl. Phys. Lett. **83**, 4315 (2003)

Chapter 5

Anisotropic plastic deformation by viscous flow in ion tracks

T. van Dillen, A. Polman, P.R. Onck, and E. van der Giessen

submitted to Phys. Rev. B

Chapter 6

Ion beam-induced anisotropic plastic deformation of silicon microstructures

T. van Dillen, M. J. A. de Dood, J. J. Penninkhof, A. Polman, S. Roorda, and A. M. Vredenberg

Appl. Phys. Lett. **84** (2004), in press

Chapter 7

Stress map for ion irradiation: depth-resolved dynamic competition between radiation-induced visco-elastic phenomena in SiO₂

T. van Dillen, M. Y. S. Siem, and A. Polman

submitted to Appl. Phys. Lett.

Chapter 8

Activation energy spectra for annealing of ion irradiation induced defects in silica glasses

T. van Dillen, M. L. Brongersma, E. Snoeks, and A. Polman
Nucl. Instrum. Methods Phys. Res. B **148**, 221 (1999)

Origin of MeV ion irradiation-induced stress changes in SiO₂

M. L. Brongersma, E. Snoeks, T. van Dillen, and A. Polman
J. Appl. Phys. **88**, 59 (2000)

Chapter 9

Colloidal assemblies modified by ion irradiation

E. Snoeks, A. van Blaaderen, T. van Dillen, C. M. van Kats, K. Velikov, M. L. Brongersma, and A. Polman
Nucl. Instrum. Methods Phys. Res. B **178**, 62 (2001)

Combined optical tweezer/ion beam technique to tune colloidal masks for nanolithography

D. L. J. Vossen, D. Fific, J. J. Penninkhof, T. van Dillen, A. Polman, and A. van Blaaderen
to be submitted

Photonic crystals of shape-anisotropic colloidal particles

K. P. Velikov, T. van Dillen, A. Polman, and A. van Blaaderen
Appl. Phys. Lett. **81**, 838 (2002)

Aligned gold nanorods in silica made by ion irradiation of core-shell colloidal particles

S. Roorda, T. van Dillen, A. Polman, C. Graf, A. van Blaaderen, and B. J. Kooi
Adv. Mater. **16**, 235 (2004)

Curriculum Vitae

Teun van Dillen werd geboren op 28 april 1976 in Culemborg. Vanaf 1988 bezocht hij het “Koninklijk Wilhelmina College” in Culemborg waar hij in 1994 zijn VWO diploma behaalde. In september van dat jaar begon hij aan de studie Natuurkunde aan de Universiteit van Utrecht. Het afstudeeronderzoek verrichtte hij in de groep “Opto-elektronische materialen” van Prof. Dr. A. Polman aan het FOM-Instituut voor Atoom- en Molecuulfysica in Amsterdam, waar hij defecten en anisotrope deformatie, geïnduceerd door ionenbundels, bestudeerde. Het doctoraalexamen aan de Universiteit van Utrecht met als specialisatie “Experimentele Natuurkunde” werd “cum laude” afgelegd in april 1999. Aansluitend zette hij zijn afstudeeronderzoek naar anisotrope deformatie onder ionenbestraling voort als promovendus. De resultaten van dit onderzoek staan beschreven in dit proefschrift.